







REVIEW ARTICLE

Applications of nanogenerators for biomedical engineering and healthcare systems

Wanli Wang¹ | Jinbo Pang²  | Jie Su³ | Fujiang Li⁴ | Qiang Li⁵  | Xiaoxiong Wang⁵ | Jingang Wang² | Bergoi Ibarlucea^{6,7} | Xiaoyan Liu² | Yufen Li² | Weijia Zhou²  | Kai Wang¹  | Qingfang Han⁸ | Lei Liu⁸ | Ruohan Zang⁹ | Mark H. Rummeli^{10,11,12,13,14} | Yang Li^{15,16} | Hong Liu^{2,17}  | Han Hu¹⁸  | Gianarelio Cuniberti^{6,7,19,20}

¹College of Electrical Engineering, Qingdao University, Qingdao, China

²Collaborative Innovation Center of Technology and Equipment for Biological Diagnosis and Therapy in Universities of Shandong, Institute for Advanced Interdisciplinary Research (IAIR), University of Jinan, Jinan, China

³College of Electronic Information, Qingdao University, Qingdao, China

⁴Department of Pediatric Surgery, The Affiliated Hospital of Qingdao University, Qingdao, China

⁵College of Physics, Qingdao University, Qingdao, China

⁶Institute for Materials Science and Max Bergmann Center of Biomaterials, Technische Universität Dresden, Dresden, Germany

⁷Center for Advancing Electronics Dresden, Technische Universität Dresden, Dresden, Germany

⁸College of Biological Science and Technology, University of Jinan, Jinan, China

⁹School of Chemistry and Chemical Engineering, University of Jinan, Shandong, Jinan, China

¹⁰College of Energy, Soochow Institute for Energy and Materials Innovations, Soochow University, Suzhou, China

¹¹Key Laboratory of Advanced Carbon Materials and Wearable Energy Technologies of Jiangsu Province, Soochow University, Suzhou, China

¹²Centre of Polymer and Carbon Materials, Polish Academy of Sciences, Zabrze, Poland

¹³Institute for Complex Materials, IFW Dresden, Dresden, Germany

¹⁴Institute of Environmental Technology, VŠB-Technical University of Ostrava, Ostrava, Czech Republic

¹⁵School of Information Science and Engineering, University of Jinan, Jinan, China

¹⁶Shandong Provincial Key Laboratory of Network Based Intelligent Computing, University of Jinan, Jinan, China

¹⁷State Key Laboratory of Crystal Materials, Center of Bio & Micro/Nano Functional Materials, Shandong University, Jinan, China

¹⁸College of Chemical Engineering, China University of Petroleum (East China), Qingdao, China

¹⁹Dresden Center for Computational Materials Science, Technische Universität Dresden, Dresden, Germany

²⁰The Dresden Center for Intelligent Materials (DCIM), Technische Universität Dresden, Dresden, Germany

Correspondence

Jinbo Pang, Collaborative Innovation Center of Technology and Equipment for Biological Diagnosis and Therapy in Universities of Shandong, Institute for Advanced Interdisciplinary Research (IAIR), University

The dream of human beings for long living has stimulated the rapid development of biomedical and healthcare equipment. However, conventional biomedical and healthcare devices have shortcomings such as short service life, large equipment size, and high potential safety hazards. Indeed, the power

Wanli Wang, Jinbo Pang, and Jie Su contributed equally to this study.

This is an open access article under the terms of the Creative Commons Attribution License, which permits use, distribution and reproduction in any medium, provided the original work is properly cited.

© 2021 The Authors. *InfoMat* published by UESTC and John Wiley & Sons Australia, Ltd.

of Jinan, Jinan 250022, China.
Email: ifc_pangjb@ujn.edu.cn

Kai Wang, College of Electrical Engineering,
Qingdao University, Qingdao 266071, China.
Email: wangkai@qdu.edu.cn

Hong Liu, State Key Laboratory of Crystal
Materials, Center of Bio & Micro/Nano
Functional Materials, Shandong University,
27 Shandan Road, Jinan 250100, China.
Email: hongliu@sdu.edu.cn

Han Hu, College of Chemical Engineering,
China University of Petroleum (East China),
Qingdao 266580, China.
Email: hhu@upc.edu.cn

Gianaurelio Cuniberti, Dresden Center for
Computational Materials Science,
Technische Universität Dresden, Dresden
01062, Germany.
Email: gianaurelio.cuniberti@tu-dresden.de

Funding information

Chinesisch-Deutsche Zentrum für
Wissenschaftsförderung, Grant/Award
Number: GZ 1400; European Regional
Development Fund, Grant/Award
Number: CZ.02.1.01/0.0/0.0/16_019/
0000853; Guangdong Basic and Applied
Basic Research Foundation, Grant/Award
Number: 2019A1515110706; National Key
Research and Development Program of
China, Grant/Award Number:
2017YFB0405400; National Natural
Science Foundation of China, Grant/
Award Numbers: 21975287, 51802113,
51802116, 52022037, 52071225; Natural
Science Foundation of Shandong
Province, Grant/Award Numbers:
ZR2018BEM015, ZR2018ZC1458,
ZR2019BEM040; Taishan Scholar Project
of Shandong Province, Grant/Award
Number: ts201712020; Taishan Scholars
Project Special Funds, Grant/Award
Number: tsqn201812083; Technological
Leading Scholar of 10000 Talent Project,
Grant/Award Number: W03020508;
Development Plan of Shandong Province,
Grant/Award Number: 2019GGX104019;
Project of “20 items of University” of
Jinan, Grant/Award Number:
2018GXRC031; Scientific Research
Development Plan of Shandong Higher
Education Institutions, Grant/Award
Number: J18KA316; China University of
Petroleum (East China)

supply for conventional implantable device remains predominantly batteries. The emerging nanogenerators, which harvest micro/nanomechanical energy and thermal energy from human beings and convert into electrical energy, provide an ideal solution for self-powering of biomedical devices. The combination of nanogenerators and biomedicine has been accelerating the development of self-powered biomedical equipment. This article first introduces the operating principle of nanogenerators and then reviews the progress of nanogenerators in biomedical applications, including power supply, smart sensing, and effective treatment. Besides, the microbial disinfection and biodegradation performances of nanogenerators have been updated. Next, the protection devices have been discussed such as face mask with air filtering function together with real-time monitoring of human health from the respiration and heat emission. Besides, the nanogenerator devices have been categorized by the types of mechanical energy from human beings, such as the body movement, tissue and organ activities, energy from chemical reactions, and gravitational potential energy. Eventually, the challenges and future opportunities in the applications of nanogenerators are delivered in the conclusive remarks.

KEYWORDS

biomedical engineering, healthcare, implantable devices, nanogenerators, self-powered devices, sensors

1 | INTRODUCTION

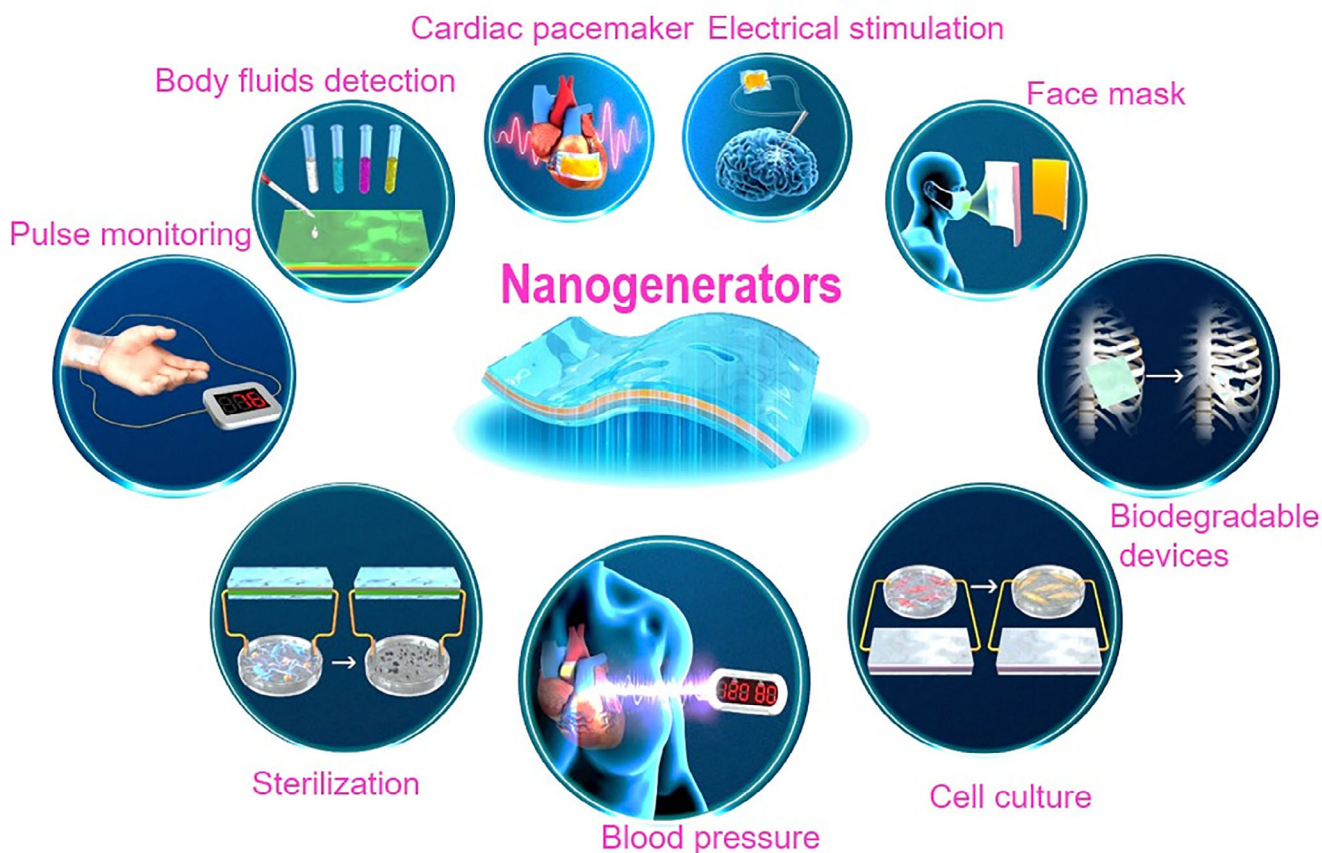
The increasing demand for safe, comfortable, and high-quality healthcare have led to an exponential increase in the biomedical technologies and healthcare services.^{1–4} In this scenario, biomedical sensors and implanted medical devices are gradually replacing traditional medical devices.^{5–9} Biomedical sensors^{10–14} are a class of equipment, developed via a combination of engineering and biomedicine, that detect or respond to physiological signals.^{15–18} They are used to measure the heartbeat,¹⁹ blood pressure,²⁰ pulse,^{21–23} body temperature,^{24–26} and blood flow.^{27,28} These detected physiological parameters^{29,30} are used for clinical diagnosis and patient monitoring. Biomedical sensors are critical medical equipment, analogous to a sensory organ that senses vital signs and extending the perceptual capability of doctors.

An implantable medical equipment³¹ combines intelligently electronic manufacturing technology and medicine^{32,33} to provide highly convenient, fast, and accurate medical services for people (Scheme 1). To name a few, an emerging trend of biomedical engineering has grown prosperous in the postoperative rehabilitation via

early diagnosis,^{34–37} therapy,^{38–41} disease treatment,^{42,43} and functional organ replacement.^{44,45}

Besides, the healthcare systems involve the specific drug delivery,^{46–50} and long-term real-time health status monitoring.^{44,45} To this end, applications of nanogenerators⁵¹ primarily include wearable and implantable sensing equipment,^{52–54} capsule endoscopes,^{55,56} cardiac pacemakers,^{57–59} artificial hearts,⁶⁰ spinal cord electrical stimulators,^{61–63} and artificial cochleae.^{64–66}

Providing safe, convenient, efficient, and reliable power supply for biomedical sensors and implantable electronic devices is one of the most critical problems. Traditional contact-based electric energy transmission via wires is prone to wear and exposure over the long term, which soon leads to accidental contact and electric shock, posing a significant potential safety hazard. In addition, the wires and cables of various biomedical equipment tend to become tangled and knotted while in use, resulting in poor contact. Consequently, implanted medical devices are currently powered by high-energy batteries,^{67–72} for example, lithium-ion batteries. However, typical battery sizes impede the miniaturization of implanted devices. The service life of



SCHEME 1 The applications of nanogenerators in biomedical engineering and healthcare devices

batteries is another limitation, requiring battery replacement surgery every few years. This secondary surgery dramatically increases the risk of infection and poses an economic burden on patients.^{73–76} Recently, a new type of noncontact power transmission technology called wireless power transfer (WPT) has rapidly developed. Furthermore, powering biomedical implantable sensors via wireless power transmission is now considered a superior energy supply method and is attracting growing attention. However, the existing wireless power transmission technology has short effective charging distance, large equipment volume, large energy loss, high electromagnetic compatibility index, and causes tissue heating. Therefore, WPT does not effectively solve challenges such as limitation of energy, device size, and device weight.

A nanogenerator is a device that harvests micro, nanomechanical, and thermal energies and converts them into electrical energy. Based on the power generation mechanism employed,^{77–79} nanogenerators can be classified into three different types: piezoelectric (PENGs),^{80–84} triboelectric (TENGs),^{85,86} and pyroelectric nanogenerators (PyENGs).^{87–90} PENGs and TENGs convert mechanical energy into electrical energy,^{91–94} whereas PyENGs convert thermal energy generated by temperature variations into electrical energy. The thermal and mechanical energy generated by the human body is sufficient to supply a nanogenerator for biomedical applications. In 2006, the concept of piezoelectric nanogenerator was first proposed.^{95,96} Until 2012, the triboelectric nanogenerator^{97,98} and pyroelectric nanogenerator⁹⁹ were successfully developed.

The self-powered nanodevice was proposed in 2008 as proof-of-concept.^{100,101} Because the nanodevice is assembled with a nanogenerator that has corresponding size, this device can harvest stray mechanical energy in its host environment and convert this energy into electricity, thus being a nanosystem operated independently of external power supply. Over the past decade, nanogenerators have rapidly developed from conceptual designs to a practical technology that effectively harvests various forms of mechanical energy from the surrounding environment,^{102–105} such as wind^{106–110} and waves.^{111–113} Besides, nanogenerators have harvested energy from the micromechanical movements such as muscle activity, heartbeat, breathing, and arterial contraction.

Self-powered micro/nanodevices provide an effective solution to the power supply limitations of biomedical implantable sensors. Therefore, nanogenerators are considered as the ideal energy source for biomedical electronic devices. In this regard, an implantable PENG (iPENG)¹¹⁴ based on zinc oxide (ZnO) was implanted into living mice to harvest energy generated via respiration and heartbeat. This was the first successful attempt at converting biomechanical energy into electrical

energy. An implantable TENG (iTENG)¹¹⁵ was successfully developed in 2014. The TENG was encapsulated and implanted in the body to harvest mechanical energy generated via respiratory muscle movement or heartbeat and convert this mechanical energy into electricity to power the implantable devices. In subsequent years, considerable research has been conducted on nanogenerators and biomedical devices, and nanogenerator use in biomedical applications has considerably grown. Nanogenerators can be used not only as a self-powered power supply for biomedical sensors but also as direct-use mechanical micro/nanosensors in biomedical applications or in the treatment of certain diseases.

First, this study briefly introduces the operating principle of the nanogenerator and reviews the progress of nanogenerators in biomedical applications, including power supply, sensing, treatment, microbial disinfection, and biodegradation. Then, the challenges to nanogenerator applications in the biomedical field are discussed, and the development and prospects for nanogenerators are summarized.

2 | NANOGENERATORS

Nanogenerators are a class of technical device that convert mechanical (e.g., vibration, wind, and human kinetic energies) or thermal energy in the surrounding environment into electricity. Thus, as a new technology that can enable the development of self-powered devices, nanogenerators have created a new field of energy harvesting and conversion. At present, there are three typical technical approaches to nanogenerators, based on three different power generation mechanisms: piezoelectric, triboelectric, and pyroelectric.^{116–118} PENGs and TENGs convert mechanical energy into electrical energy, whereas PyENGs convert thermal energy generated by temperature fluctuations into electrical energy.

2.1 | Piezoelectric nanogenerator

There is a phenomenon that mechanical energy and electrical energy are exchanged in piezoelectric materials. Under a deformation by an external force, polarization occurs within the material,^{119–123} while positive and negative charges simultaneously generate on opposing sides along the direction of polarization.¹²⁴ This is called a positive piezoelectric effect. In contrast, the inverse piezoelectric effect means that when a voltage is applied to the polarization direction of a dielectric material, the material will undergo a phase change. PENGs exploit the positive piezoelectric effect in piezoelectric nanomaterials.^{125,126}

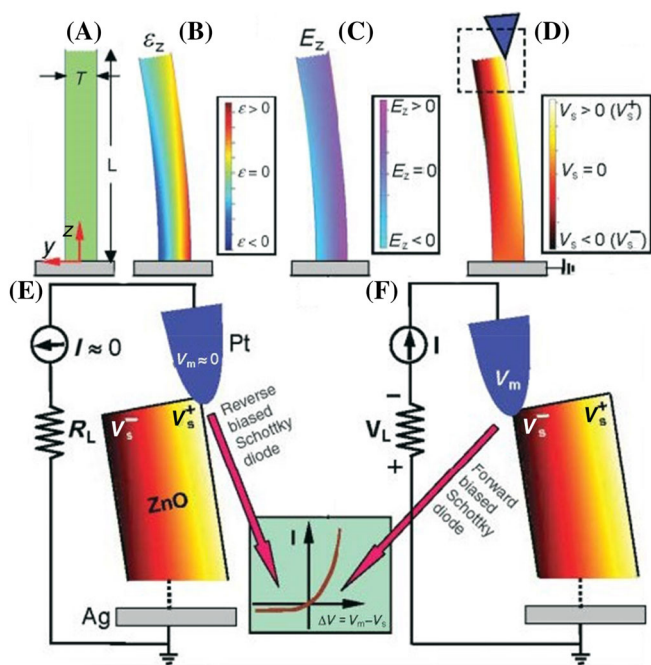


FIGURE 1 Operating mechanism of the piezoelectric nanogenerator. (A) Scheme of a ZnO nanowire and its coordination system. (B) Longitudinal strain ϵ_z distribution in the ZnO nanowire at a bending status. (C) The longitudinal piezoelectric-induced electric field E_z distribution. (D) Potential distribution. (E) Reverse- and (F) forward-biased Schottky rectifying curves of the AFM tip/nanowire contact. Reproduced with permission.⁹⁵ Copyright 2006, American Association for the Advancement of Science

The operating mechanism of the earliest PENG is presented in Figure 1. One end of a vertically grown ZnO nanowire is fixedly connected to a metal electrode, and the other end is deformed under the action of an atomic force microscope probe. When a ZnO nanowire is bent, it is simultaneously stretched and compressed on its opposing surfaces, generating a positive charge on the stretched surface and a negative charge on the compressed surface. Because ZnO is an N-type semiconductor, a Schottky junction is formed at the boundary between the ZnO and the Pt probe.

When the probe is in contact with the ZnO surface, a small number of negative charges accumulate on the probe's surface, and electrons can no longer flow from the ZnO nanowire to the Pt probe under the effect of the Schottky junction. When the probe scans from the tensile surface to the compressed surface of the ZnO nanowire, the Schottky junction is in a conducting state, and electrons flow from the ZnO nanowire through the probe via the external circuit.^{127–131}

2.2 | Triboelectric nanogenerator

The triboelectric effect refers to the phenomenon in which rubbing two different substances against each

other results in electron transfer from the surface of the substance with weaker electron binding ability to the surface of the substance with stronger electron binding ability, making the former positively charged and the latter negatively charged. Triboelectrification was discovered over 2600 years ago and is a very common phenomenon in daily life.

Electrostatic induction refers to the redistribution of electric charge in conductors due to the interaction of electric charges when charged and uncharged objects approach each other. This phenomenon was discovered by scientists John Canton and John Calville, in 1753 and 1762, respectively. Electrostatic induction occurs because the free charge in a conductor moves directionally when exposed to the force in an electric field such that the two ends of the conductor generate equal amounts of opposite charges,^{132–134} that is, the induced charge.^{135,136}

The TENG couples the triboelectric effect with electrostatic induction for energy conversion.^{137,138} The mechanism is briefly depicted as follows.^{139–143} First, it accumulates positive and negative charges on two friction layers via the triboelectric effect, and then outputs electric energy via electrostatic induction between its moving friction layers and electrodes.

The basic unit of the TENG typically comprises two types of dielectric film with a micro/nanostructure and different electron gain/loss capabilities that are attached via back electrodes. At least one of these dielectric films is an insulator to facilitate storage of the electric charges generated by the triboelectrification effect on the surface of the films. A TENG has four primary operational modes,¹⁴⁴ namely vertical contact–separation, lateral sliding, single-electrode, and freestanding triboelectric-layer (FTENG) modes (Figure 2).

2.2.1 | Vertical contact–separation mode

Due to its simple structure and high output performance, TENG's vertical contact–separation mode is the most commonly utilized.¹⁴⁶ Figure 3 illustrates the operating principle of the TENG in vertical contact–separation mode for open and short-circuited external circuits. In this mode, the typical composition of TENG is dielectric–dielectric model: two polymer insulator materials are placed opposite to each other and separated by gaskets, and the other side of the polymer films is plated with metal electrodes.

When the device is in its original state (Figure 3A), the entire device is electrically neutral. When influenced by an external force, the two polymer films contact and rub against each other. Due to the difference in the ability of the friction layer to gain or lose electrons, the material with positive electronegativity loses electrons.

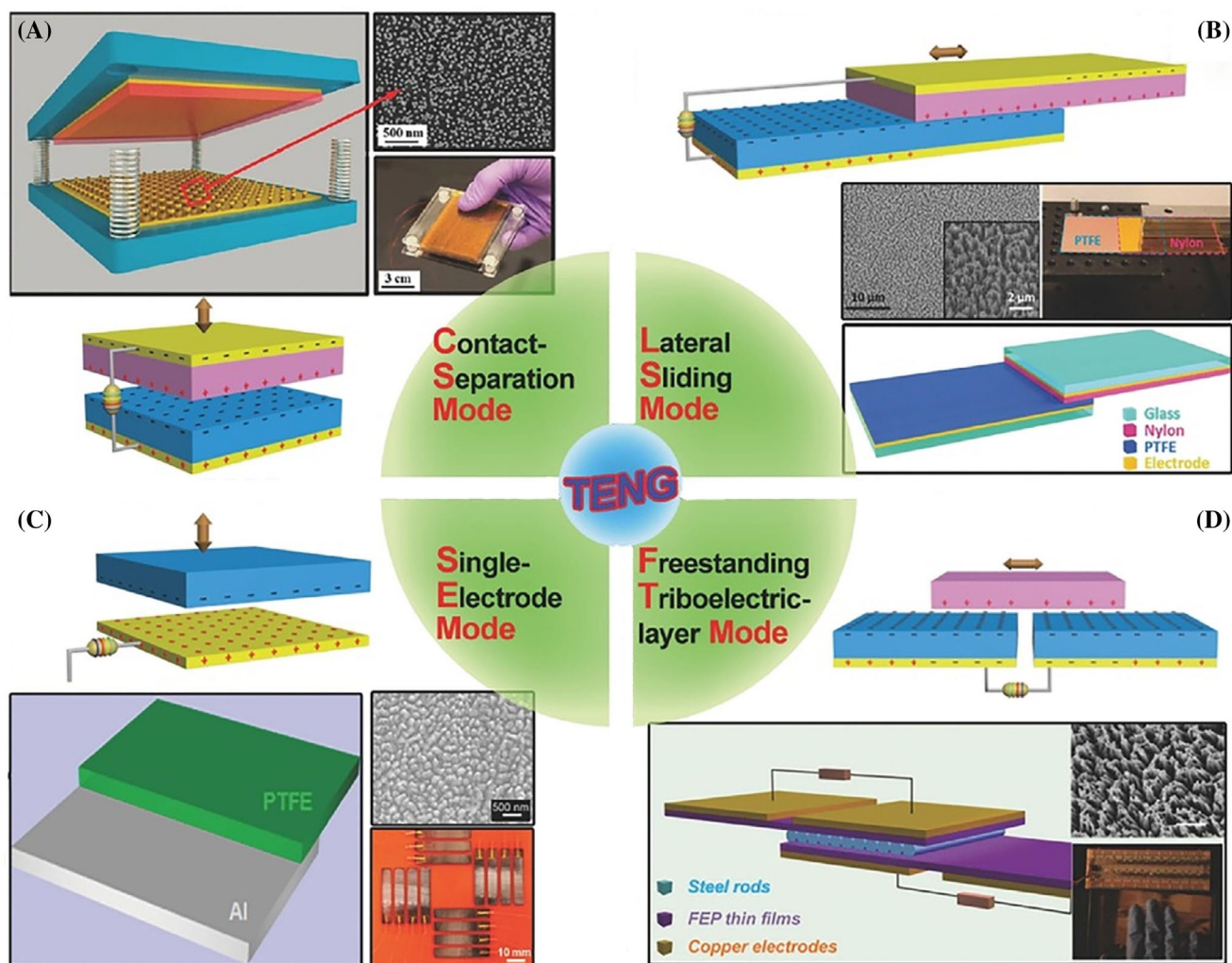


FIGURE 2 The four primary operational modes of a TENG. (A) Vertical contact-separation mode. (B) Lateral-sliding mode. (C) Single-electrode mode. (D) Freestanding triboelectric-layer mode. PTFE stands for polytetrafluoroethylene. FEP denotes fluorinated ethylene propylene. Reproduced with permission.¹⁴⁵ Copyright 2016, Wiley-VCH Verlag GmbH

In contrast, the material with negative electronegativity gains an equal amount of electrons.¹⁴⁸ Consequently, the upper and lower friction layers gain equal amounts of opposite charge, that is, frictional charge. Because the polymer is an insulating material, frictional charges can be accumulated on the surface of the polymer films for a long time without dissipation.

When the two polymer films are separated by an external force, a potential difference is generated between the two electrodes.¹⁴⁹ With an increase in the separation distance, the open-circuit voltage continuously increases until the device returns to its original state, which is a point of open-circuit voltage peak. In an ideal state (where the impedance of the external circuit is infinite), the voltage remains unchanged. Subsequently, the distance between the two polymer films is reduced by an external force, and the open-circuit voltage continuously decreases until the two films are in full contact, which is a point where the open-circuit voltage decreases to zero.

When the external circuit is connected to an ammeter (Figure 3B), the triboelectrification process for the two polymer films is the same as that for the external voltmeter. As the two polymer membranes separate, electrons are transferred to balance the potential difference caused by the distance. However, when the two polymer films return to complete contact, the potential difference generated by the frictional charges dissipates, and the electron transfer is reversed.

Owing to its ease of fabrication and excellent performance, the vertical contact–separation TENG is extensively applied to collect mechanical energy caused by flapping, oscillation, and sound waves.

2.2.2 | Lateral sliding mode

Converting mechanical energy from horizontal sliding motion into electric energy mainly depends on the lateral

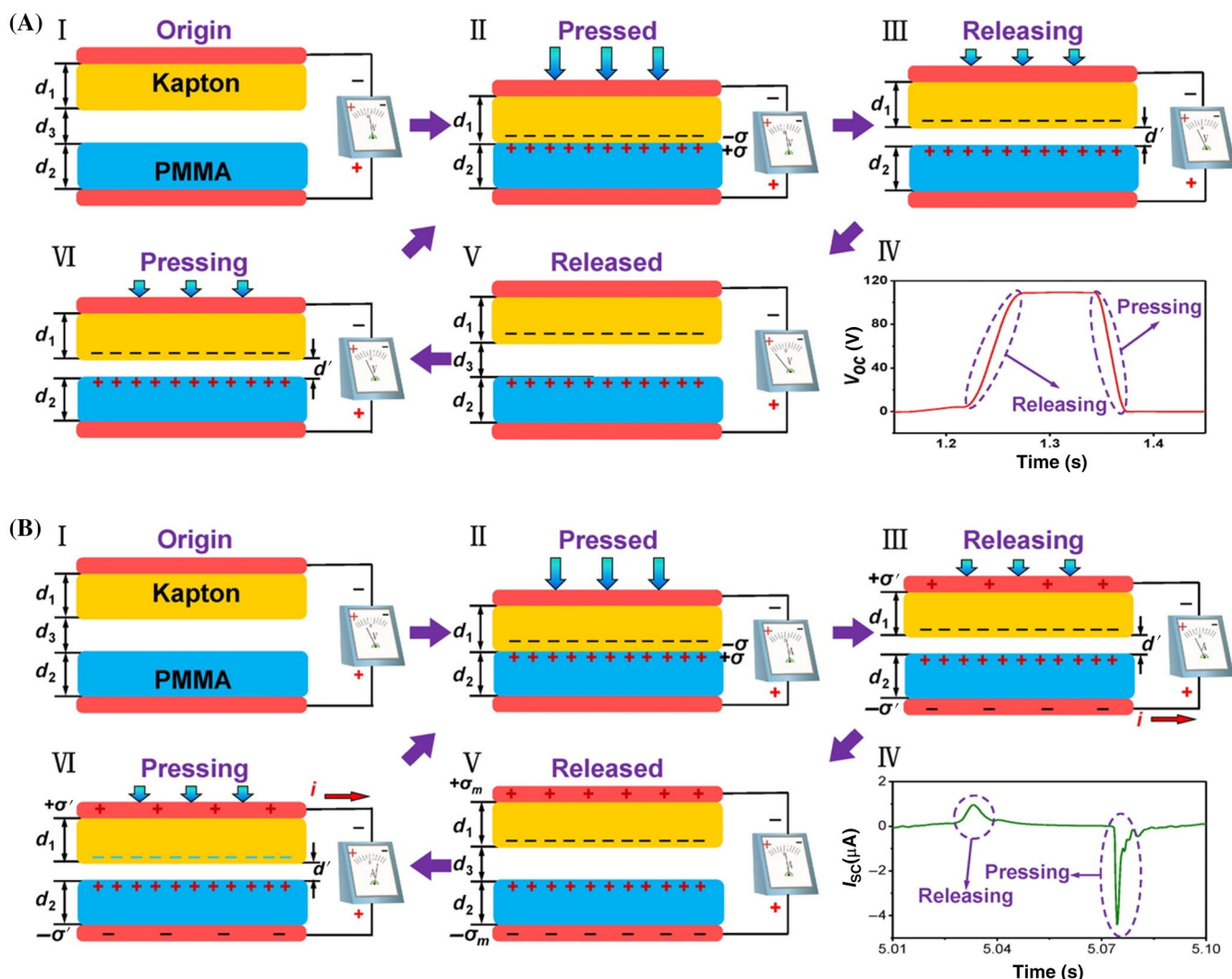


FIGURE 3 Operating principle of the vertical contact-separation mode TENG. The external circuit is (A) connected to an ammeter; (B) connected to a voltmeter. The PMMA denotes polymethyl methacrylate. Reproduced with permission.¹⁴⁷ Copyright 2012, American Chemical Society

sliding mode TENG, solving the limitation of the conventional TENG working only in the vertical direction. The operational process of the lateral sliding mode TENG^{150–153} is presented in Figure 4, with polytetrafluoroethylene (PTFE) and polymer nylon used as the friction materials.

Metal electrodes are plated onto the outer sides of the two polymers, and the outer sides of the two metal electrodes are attached to a glass substrate. The PTFE and nylon are rubbed against each other by sliding the glass substrate, which generates an equal amount of opposite charge.

When the upper and lower substrates slide relative to each other and are no longer fully aligned, the positive and negative frictional charges on the polymer can no longer be completely shielded from each other, thus the exposed positive and negative charges change the potential difference of the upper and lower electrodes. The potential difference at the exposed end of the positively

charged polymer is inevitably higher than that at the exposed end of the negatively charged polymer. This potential difference causes the electron transfer between the upper and lower electrodes, realizing the transformation from mechanical to electrical energy.

Compared with existing vertical contact-separation mode TENGs, the lateral sliding mode TENG has structural advantages, including the capacity to maximally harvest sliding mechanical energy, high efficiency, and convenient integration and encapsulation. The TENG is often used for harvesting mechanical energy in the forms of wind energy, water energy, and relative sliding.

2.2.3 | Single-electrode mode

The main difference between the two TENGs previously mentioned is the direction of the relative motion of the

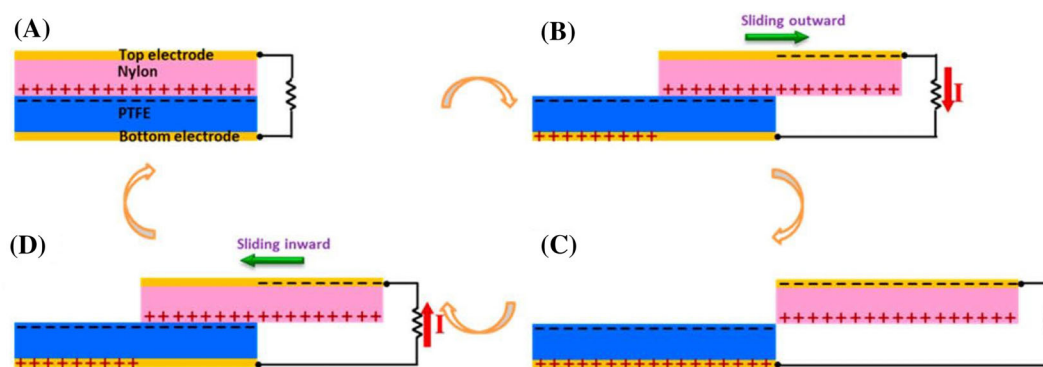


FIGURE 4 Operating principle of the lateral sliding mode TENG. The nanogenerator operates with periodically repeating the four states. (A) Two polymer surfaces are completely overlapped and closely contacted. (B) The top polymer with positive charge surface starts to slide outward. (C) The top polymer completely slides out of the bottom polymer with both triboelectric surfaces completely separated. (D) The top polymer slides backward. Reproduced with permission.¹⁵⁴ Copyright 2013, American Chemical Society

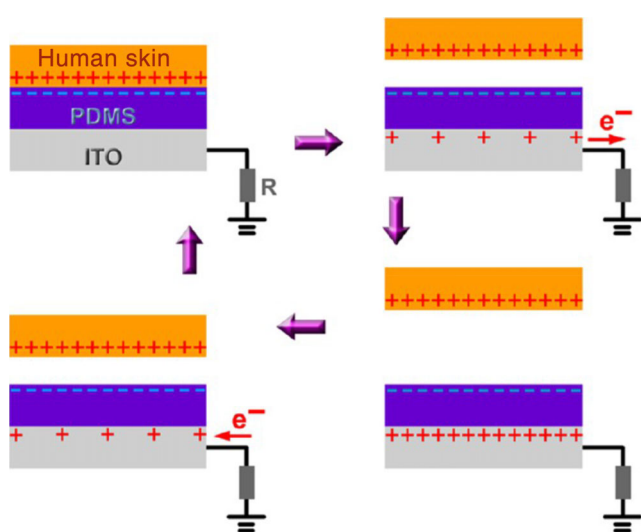


FIGURE 5 Operating principle of the single-electrode mode TENG. The PDMS denotes polydimethylsiloxane. The ITO stands for the indium tin oxide. Reproduced with permission.¹⁶¹ Copyright 2013, American Chemical Society

two friction materials. The common characteristic of the two previous modes is that the friction layers and the electrodes are connected to the load, which can be useful in a situation where the device is mobile. However, in real world applications, when only one contact surface of the nanogenerator is mobile, for example, a car or a walking person, the previous two modes of the nanogenerator would be unable to effectively harvest energy.

To overcome this limitation, researchers have proposed a single-electrode mode TENG.^{155,156} Unlike the conventional TENG, the single-electrode mode TENG¹⁵⁷ only contains one dielectric layer and one electrode.^{158–160} The induction electrode is connected to the earth via the conductor, and the earth replaces the other induction electrode. The entire ground potential can be regarded as

zero, and the potential difference between the induction electrode and the earth promotes the transfer of electric charge. The operating principle of the single-electrode mode TENG (Figure 5) is basically similar to that of the conventional dielectric–dielectric TENG.

A metal conductive electrode is plated onto the back of a polymer film, and the conductive electrode is directly grounded to form a circuit when connected to an external load. Due to the friction polarity difference between the free moving friction object and the polymer film, the same amount of opposite frictional charge is generated when they are in contact. When the two contact surfaces are separated, the interval between the two contact surfaces leads to a potential difference between the conductive electrode and the earth wire, and the potential difference drives the flow of electrons, generating current output.

The single-electrode mode TENG considerably expands the range of application of the TENG, enabling it to harvest energy via a human–machine interface, bodily movement, object rotation, and even liquid flow and other environments. It is a more flexible power generation mode.

2.2.4 | Freestanding triboelectric-layer mode

The freestanding triboelectric-layer mode TENG (FTENG)^{162–166} is a further developed single-electrode mode. With the elimination of the grounding structure, it can freely move, providing considerable flexibility. The structure consists of two interconnected metal electrodes attached in parallel to a polymer film layer. A fluorinated ethylene propylene (FEP) film serves as an independent friction material, while two connected Al foils arranged in parallel function as a conductive electrode and a second friction layer (Figure 6).

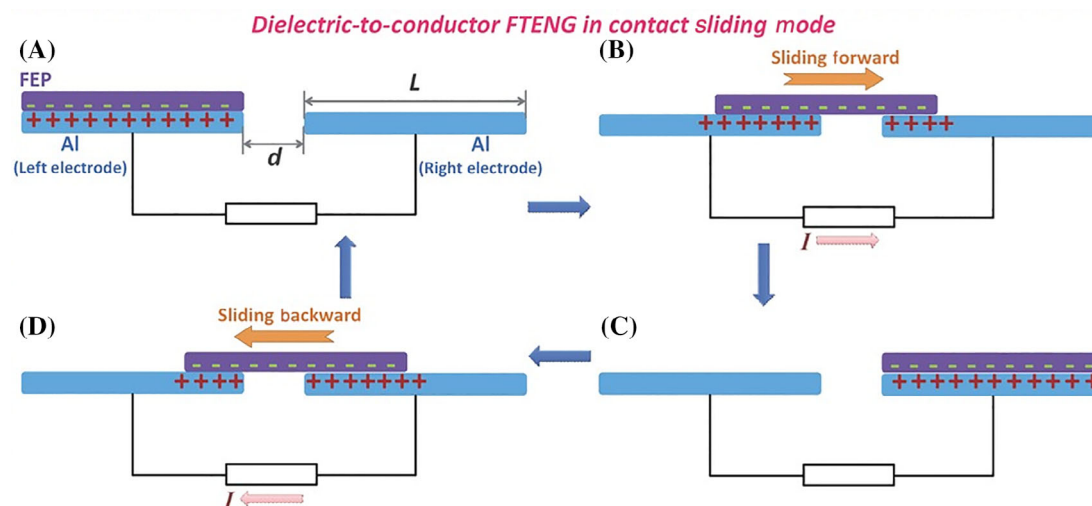


FIGURE 6 Operating principle of the freestanding TENG. (A) The FEP layer overlaps completely with the left electrode. (B) The FEP layer slides towards the right electrode. (C) The FEP layer slides to the overlapping position with the right electrode. (D) The FEP layer slides from the right electrode to the left. Reproduced with permission.¹⁶⁷ Copyright 2014, Wiley-VCH Verlag GmbH

2.2.5 | Self-charging mechanism

Actually, the common energy storage devices (polar capacitors, batteries, etc.) and electronic components (light-emitting diodes [LEDs], etc.) strictly distinguish the positive and negative poles, and the output signal of TENG presents the alternating current characteristics similar to sine wave with the contact–separation movement. Direct connection between AC signal and DC system will cause mismatch, resulting in waste of reverse signal and even damage to electronic equipment. And in practical application, the mechanical movement of human body is uncertain, so TENG cannot provide electric energy continuously. To sum up, it is necessary to rectify the output current and store it in the energy storage device before supplying power to the subsequent circuits.

It should be noted that TENG, as a capacitive energy harvester, has a high inherent impedance, which is usually in the range of several megaohms to tens of megaohms. However, the impedance of miniature electronic equipment and energy storage devices such as batteries and capacitors is relatively low. This characteristic of TENG leads to low energy transfer efficiency after rectification, whether it is directly supplying power to electronic equipment or charging energy storage equipment. Therefore, a universally matched power management design is needed to deal with the problem of impedance matching. Figure 7 is a very classic power management design, TENG is represented by a series AC power supply and a capacitor, which is directly connected with a rectifier bridge composed of four diodes, and the rectifier bridge converts AC electrical signals into DC electrical signals. And finally, the rectifier bridge is connected with a direct current step-down circuit composed of a switch tube S, a diode D_1 , an inductor L and a capacitor C , so as

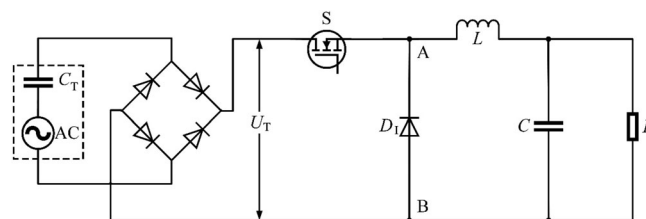


FIGURE 7 Power management design of TENG

to realize the step-down and current-up of the circuit. This circuit solves the problem of impedance mismatch to a certain extent, and the whole circuit is composed of miniature electronic electrification, which is small in size and easy to integrate.

2.2.6 | Preparation method of nanogenerator

Manufacturing method is the basis of device production, and scientific and reasonable manufacturing method is the decisive factor of producing high-quality devices. Compared with traditional electronic devices, flexible electronics devices have better flexibility, are easier to adapt to various working environments, and meet the deformation requirements of devices, which also means that there is a larger application space, has flexibility, to adapt to various working environments, and meets the deformation need of devices, which also means that there is more application space.

Therefore, considering the long-term development, flexibility is the first condition to be considered in the preparation of nanogenerators. In addition, considering the future industrial production and large-scale

application, low cost and high efficiency are also necessary conditions for the preparation of nanogenerators. Soft lithography process and flexible printed circuit board (PCB) process are considered as the general large-scale manufacturing technologies for flexible TENG.

Soft lithography is a mighty technology to form surface topography by using mold replication structure. Generally, a flexible imprint mold is made of soft polymer material, and after SAM (self-assembly monomer) is coated on the mold, it is slightly pressed on the gold-plated film substrate like a stamp, and the self-assembly monomolecular of the protruding part on the nanopattern mold is printed on the gold film like ink, thus completing the transfer of surface pattern. Soft lithography technology,^{168–170} which can easily manufacture surface microstructures, and even make molds on irregular curved surfaces, which is not limited by materials and chemical surfaces, and has been used to produce TENG materials with surface patterning. At the same time, due to the reusability of the mold, this technology is very suitable for large-scale production of surface pattern materials, and the production cost is greatly reduced because lithography is avoided. It is a cheap, efficient, and suitable technology for large-scale use.

Of course, it is inevitable that there are some defects in the application of soft lithography in micro-machining. As the most commonly used elastic mold material in soft lithography, PDMS¹⁷¹ has shrinkage deformation after curing, and under the action of toluene and ethane, the aspect ratio will also change to some extent. In addition, PDMS has elasticity and thermal expansion, which makes it difficult to obtain high accuracy, which limits the application of this material in soft lithography. But these are not enough to prevent PDMS from being widely used in soft lithography.

PCB is a very important part of electronic products. PCB technology uses insulating board as base material, which is cut into a certain size, with at least one conductive pattern attached to it and holes (such as component holes, fastening holes, metallized holes, etc.), to replace the chassis of electronic components of previous devices, and realize the interconnection between electronic components. Because this kind of board is made by electronic printing, it is called “printed circuit board”. PCB is the key interconnection of electronic equipment, which plays an important supporting role in scientific research, communication, automobile, aerospace, and other fields, and is an important foundation of modern science and technology. Its own development and the continuous improvement of related technologies promote the continuous development of society and economy. With the adoption of PCB technology, due to the standardization of industrial production and the unification of PCB standards, manual errors are avoided,

and electronic components can be automatically inserted or mounted and automatically detected, thus ensuring the quality of electronic equipment, improving labor productivity, reducing costs and facilitating detection and maintenance.

As a PCB technology, flexible printed circuit board (FPCB) technology retains all the advantages of PCB technology, and has flexible characteristics. It makes surface graphics on a flexible substrate surface by means of photo imaging graphics transfer and etching process, which can be curled, coiled and folded in half at will, and is widely used in many fields such as flexible, wearable and implantable devices. In addition, FPCB can greatly further reduce the volume and thickness of electronic products, which is conducive to miniaturization and integration of equipment. And its comprehensive cost is low, and it is easy to realize the batch manufacturing of flexible TENG. It has good application in the preparation of contact TENG¹⁷² and sliding TENG.¹⁷³

Similarly, FPCB technology also has some disadvantages. First of all, after the flexible PCB is manufactured, it can only be changed from the base map or the compiled photo drawing program, which is difficult to modify. Second, at present, the soft PCB technology has not been popularized, which is limited by the size of industrial unit, so it is limited to miniaturization application.

2.2.7 | Performance evaluation of nanogenerator

The triboelectric nanogenerator has four working modes, and each mode has different structural design and material selection to adapt to the corresponding mechanical triggering conditions. Therefore, in order to quantitatively characterize and analyze the output and efficiency of generators in various modes, we need a general evaluation scale. By constructing the cycle for maximized energy output (CMEO) of TENG, a performance figure-of-merit (FOM_P) was proposed with a model constituted of structural figure-of-merit (FOM_S) and material figure-of-merit (FOM_M).^{174,175}

For periodic mechanical movement, the electrical signal generated by TENG will also be periodic. In this way, the average output power \bar{P} is generally utilized to evaluate the quality of the generator. When the period T is determined, the output energy E per period can be deduced as:

$$E = \bar{P}T = \int_0^T vI dt = \int_0^T v dQ = \oint v dQ \oint. \quad (1)$$

Therefore, the charge state and energy generation of TENG can be expressed by the curve of voltage V versus transferred charge Q . In view of this V - Q curve, in order to quantitatively analyze the operating state of TENG, different working processes are described as different operating cycles, mainly including the energy output cycle and the maximum energy output cycle when TENG is connected with an external resistor.¹⁷⁶ The energy output cycle refers to a closed loop formed by V - Q curve.^{177,178} According to V - Q relationship, for CEO of each energy output cycle, the total cycle charge Q_C is smaller than the maximum transfer charge $Q_{SC,max}$ all the time. If we can uniformly maximize the Q_C of these cycles to $Q_{SC,max}$, the energy E generated in each cycle will be improved.

The key to maximize the energy of each cycle is the use of switches in parallel with resistors. Taking the horizontal sliding mode as an example, whenever the friction charge accumulates to the maximum value, that is, when the sliding distance reaches the maximum value, the switch is closed to complete the energy release, and so as to realize the maximum energy output. Under infinite load resistance, the maximum possible output energy E_m per cycle can be calculated theoretically by the following formula:

$$E_m = \frac{1}{2} Q_{SC,max} (V_{OC,max} + V'_{max}). \quad (2)$$

In the formula, $V_{OC,max}$ is the maximum value of the maximum open circuit voltage, and the maximum value of the maximum achievable absolute voltage at the position where $Q = Q_{SC}$ is V'_{max} . \bar{P} at this time is expressed as:

$$\bar{P} = \frac{E_m}{T} \approx \frac{E_m}{2 \frac{x_{max}}{v}} = \frac{\bar{v}}{2} \frac{E_m}{x_{max}}. \quad (3)$$

In which T is the cycle period and \bar{v} represents the average speed of relative movement of the two friction layers.

Therefore, the energy conversion efficiency η of the generator is:

$$\eta = \frac{E_{out}}{E_{in}} = \frac{E_{output \text{ per cycle}}}{E_{output \text{ per cycle}} + E_{dissipation \text{ per cycle}}} = 1 / \left[1 + 1 / \left(\frac{E_m}{2 \bar{F} x_{max}} \right) \right], \quad (4)$$

where is the average dissipation force in the moving process, which can be air resistance, friction force, and so forth. Therefore, it can be seen from formulas (3) and (4) that \bar{P} and η are related to E_m/x_{max} term. It is worth

noting that the values of E_m and x_{max} only depend on TENG itself. In formula (2), E_m includes $Q_{sc,max}$, which is a quantity proportional to the friction surface area A . In order to eliminate the influence of the generator size on the performance, A should be introduced into E_m/x_{max} term as a divisor, so that E_m/Ax_{max} term which can determine TENG quality can be obtained.

In formula (2), $Q_{sc,max}$ and $V_{oc,max}$ are all proportional to σ . Therefore, E_m should be proportional to σ .² To sum up, the structural index FOM_S of TENG is defined as:

$$FOM_S = \frac{2\epsilon_0}{\sigma^2} \frac{E_m}{Ax_{max}}, \quad (5)$$

where ϵ_0 is the vacuum dielectric constant. The quality factor of this structure represents TENG's quality from the perspective of structural design. To sum up the performance index FOM_P of TENG is defined as:

$$FOM_P = FOM_S \cdot \sigma^2 = 2\epsilon_0 \frac{E_m}{Ax_{max}}. \quad (6)$$

In this formula, σ is FOM_M , it only depends on the materials themselves. Because it is related to the maximum possible average output power and energy conversion efficiency, but has nothing to do with the mode and size of TENG, this performance quality factor can be used as a unified standard for evaluating different TENG.

2.3 | Pyroelectric nanogenerator

In general, the conversion of thermal energy into electrical energy utilizes the Seebeck effect,^{179,180} a phenomenon in which the temperature difference between two dissimilar conductive materials produces a potential difference and drives electron flow, generating electricity. However, under normal circumstances, temperature distribution in the same environment often has spatial consistency, and the temperatures of materials are basically the same. Over time, there is essentially no temperature gradient between these objects. In this case, the Seebeck effect does not apply. Unlike the Seebeck effect, the pyroelectric effect derives from a change in polarization intensity due to temperature change in an insulating material with spontaneous polarization, producing equal and opposite charges at both ends of the material, which overcomes the limitation of the Seebeck effect. The pyroelectric nanogenerator^{181,182} is a nanodevice that converts thermal energy generated by temperature variations into electrical energy utilizing the pyroelectric effect.¹⁸³⁻¹⁸⁶

The operating mechanism of the pyroelectric nanogenerator can be generally divided into two types: one

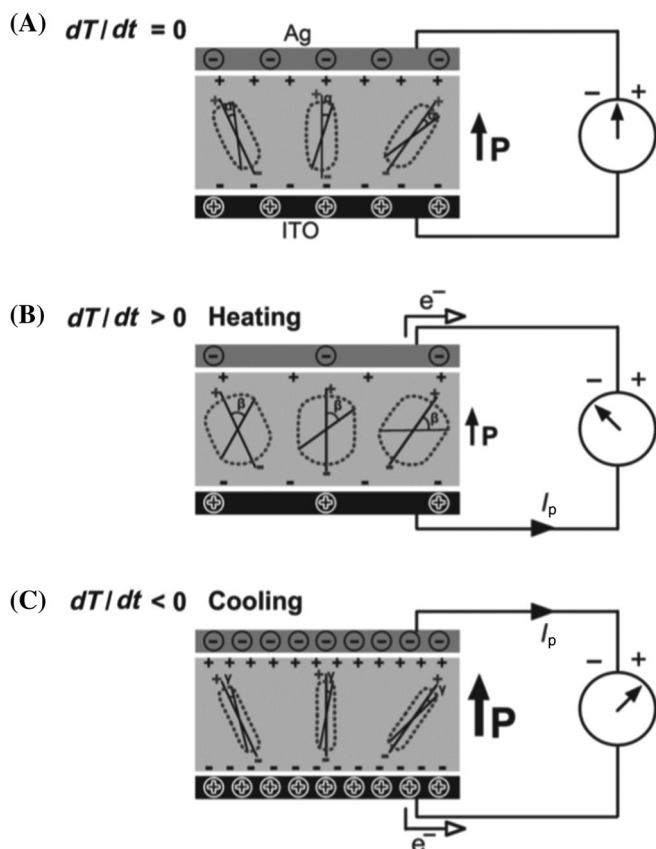


FIGURE 8 Operating principle of the pyroelectric nanogenerator at (A) constant temperature, (B) heating and (C) cooling conditions. Reproduced with permission.¹⁸⁷ Copyright 2012, Wiley-VCH Verlag GmbH

relies on the basic pyroelectric effect and the other on the secondary pyroelectric effect. Figure 8 illustrates the generating mechanism of the pyroelectric nanogenerator.⁹⁹ The basic pyroelectric effect is used to describe how to generate electric charge without tension. This effect is important for most pyroelectrics and is primarily related to the random oscillation of the electric dipole near the equilibrium axis induced by heat. This random oscillation increases with the increase in temperature. This effect is very important for most ferroelectric materials, which is mainly related to the random oscillation of the electric dipole.

When the temperature is in a fluctuating state, the amplitude of the random oscillation of the electric dipoles along their respective adjusting axes changes within a certain range, thus current output is generated. If the temperature is constant, the total average spontaneous polarization intensity of the electric dipole inside the material remains constant, and there is no charge transfer and no current output. When the temperature of the pyroelectric nanogenerator increases with time, the electric dipoles inside the material undergo large-scale extension oscillation near their respective adjusting axes,

which correspondingly reduces the total average spontaneous polarization intensity and the amount of electric charge induced on the electrodes, thus causing electron transfer.

In contrast, when the pyroelectric nanogenerator temperature decreases with time, the electric dipoles inside the material oscillate within the extension angles of the smaller levels of their respective equilibrium positions, resulting in an increase in the total spontaneous polarization intensity and in the amount of charge induced on the corresponding electrodes, driving electron flow in the reverse direction to generate reverse current.

The second type is described using the secondary pyroelectric effect: for wurtzite structure materials, the main driving force for electron transfer is the piezoelectric potential difference caused by thermal deformation along a cross-section of the material. The pyroelectric nanogenerator's current output is proportional to the thermal deformation and piezoelectric coefficient of the material, and can be expressed by the following formula:

$$I = pA(dT/dt), \quad (7)$$

where p represents the pyroelectric coefficient, A represents the friction layer area of the nanogenerator, and dT/dt represents the temperature change rate.

For the convenience of analysis and comparison, Table 1 briefly summarizes the mechanism, advantages and disadvantages and applications of the above three types of nanogenerators.

In addition, due to the advantages of high current, high durability and high efficiency under high frequency trigger, the current energy conversion system is still dominated by electromagnetic generators; however, electromagnetic power generation devices are large in size and complex in structure, which makes it difficult for them to meet the development needs of miniature electronic devices. Nanogenerator is a brand-new microenergy conversion device. Unlike electromagnetic generator, its power generation mainly depends on the material's own characteristics rather than electromagnetic induction law and electromagnetic force law (Table 2) provides a comparison of the mechanism, advantages and disadvantages between electromagnetic generator and triboelectric nanogenerator. It can continuously collect various discrete mechanical energy in the environment (such as wind energy, sound wave energy, raindrops, water waves, mechanical vibration, rotation, rolling, human motion, even breathing and heartbeat, etc.), realize high-efficiency energy conversion triggered by low-frequency machinery, and convert these energies into electric energy to drive electronic equipment, which is expected to solve the problem of sustainable power supply for electronic equipment.

TABLE 1 Comparison of mechanism, advantages, disadvantages, and application among three types of nanogenerators

Types of nanogenerators	Working mechanism	Advantages	Disadvantages	Applications
PENG	Piezoelectric effect and electrostatic induction	Easy to shrink to nanometer level	Low output and low efficiency	Sonar system, meteorological detection, smart wear, and health diagnosis
TENG	Triboelectric effect and electrostatic induction	High voltage output, high efficiency at low frequency, low cost, low weight, simple structure, and wide selection of materials	Low durability and high impedance	Smart wear, health diagnosis, environmental detection, and human-computer interaction
PyENG	Pyroelectric effect	High sensitivity, fast response rate, and easy miniaturization	Low output and low efficiency	Infrared thermal imaging, flame detection, temperature detection, and laser detection

TABLE 2 Comparison of mechanism, advantages, and disadvantages between electromagnetic generator and triboelectric nanogenerator

Types	Electromagnetic generator	Triboelectric nanogenerator
Working mechanism	Electromagnetic induction	Triboelectric effect and electrostatic induction
Advantages	High current, low voltage High output efficiency under high frequency trigger High durability and long service life	High output efficiency under low frequency trigger High voltage, low current Low cost, low density, and low weight Simple structure Multiple working modes Diverse material selection Sensor applications
Disadvantages	Low impedance Heavy weight and high density High cost	High impedance Low durability

At the same time, nanogenerators are small in size, light in weight, simple to manufacture and not limited by fixed structures, and can be easily integrated with various microelectronic devices through different structural designs, which makes nanogenerators have great development potential in the future application of intelligent and implantable electronic devices. More importantly, the nanogenerator has low cost, easily available raw materials, and will not damage the environment in the

working process. It is an environment-friendly device that can be applied on a large scale. At present, it has made great achievements in smart wear, health diagnosis, environmental detection and human-computer interaction, and has broad application prospects.

3 | NANOGENERATOR APPLICATION IN BIOMEDICAL SENSORS

With the rapid development of, sensors have been widely used. With the rapid development of information industry in various countries, sensors have widely used, for example, industrial production, ocean exploration, human-computer interaction, environmental protection, smart home, medical diagnosis, and bioengineering. As a new power generation technology, nanogenerators effectively harvest micro-biomechanical energy generated by human motion, muscle activity, heartbeat, respiration, and arterial contraction. Thus, nanogenerators can be used directly in biosensors to convert biological signals into electrical signals. For example, wearable nanodevices can be used outside the human body to collect gait, respiration, facial expression, and other information, and an implantable nanogenerator can be used to detect information such as heart rate and blood sugar.^{188,189} Table 3 summarizes some applications of nanogenerators in biomedical sensors. The application of nanogenerators in biosensors provides a new and effective method of medical diagnosis^{198,199} and disease treatment.^{200,201}

Among the three kinds of nanogenerator, PENG and TENG are far more used in biomedical sensors than PyENG, because PyENG works based on pyroelectric effect and only responds to the detected temperature, so it can only be used as a temperature sensor. And the

TABLE 3 Performance and application of nanogenerators as biomedical sensors

Sensor type	Nanogenerator type	Materials	Nanogenerator size (cm ²)	Output performance	Monitored parameters	Working principle	References
Body fluid detection	PENG	Agarose and BaTiO ₃ nanoparticles	3 × 3	V _{OC} : 80 V; I _{SC} : 285 nA (experimental test)	Cysteine	Cysteine binds to the film, increasing its surface negative charge	190
	PENG	BaTiO ₃ nanoparticles and PVDF film	2.5 × 2.5	V _{OC} : 5 V; I _{SC} : 900 nA (experimental test)	Glucose	Glucose molecule acts as an electron donor to the BTO NPs film	191
Pulse sensor	TENG	Nanostructured Kapton thin film and nanostructured Cu film	2 × 1	V _{OC} : 1.52 V; I _{SC} : 5.4 nA (radial arteria)	Pulse	TENG converts human pulse biomechanical signal into electric signal	192
Respiratory sensor	TENG	Cu-coated polyethylene terephthalate warp yarns and polyimide-coated weft yarns	6 × 4	V _{OC} : 4.98 V; I _{SC} : 15.50 mA/m ⁻² (the t-TENG was tapped at 10 cm/s)	Respiratory rate and depth	TENG stretches/releases as the chest cavity expands/contracts	193
	PyENG	A metal coated PVDF film	3.5 × 3.5	V _{OC} : 42 V; I _{SC} : 2.5 μA (normal breathing drives PyENG at 5°C)	Respiratory rate	A temperature fluctuation induced change of polarization will generate potential between electrodes due to pyroelectric effect	194
Multiple physiological signal monitoring	TENG-PENG and PyENG	PDMS, PVDF, and silver nanowires	3 × 3.5	TENG-PENG: V _{OC} : 55 V; PyENG: V _{OC} : 86 V (experimental test)	Breath, pulse, swallowing and neck tilting	Physiological signals were captured by TENG-PENG, and pyroelectric effects caused by temperature fluctuations are captured by PENG	195
Auditory sensor	TENG	Kapton film and aluminum foil	11.1 × 5	n.a.	Acoustic stimuli	Triboelectric effects convert an acoustic stimulus to electricity	196
Endocardial pressure sensor	TENG	Nano-polytetrafluoroethylene film and Al foil	1 × 1.5 × 0.1	V _{OC} : 0.45 V; I _{SC} : 0.2 μA (maximal pressure of 350 mmHg)	Endocardial pressure	TENG can convert the energy of blood flow within the heart chambers into electricity	197

Abbreviations: I_{SC}, short-circuit current; PDMS, polydimethylsiloxane; PVDF, polyvinylidene difluoride; V_{OC}, open-circuit voltage.

temperature of human body is almost constant, which basically eliminates the possibility of PyENG as the sensor power supply. PENG and TENG are widely used compared with PyENG, because the influence of body fluid on piezoelectric or triboelectric materials will lead to the change of nanogenerator output, so the concentration of body fluid can be detected. In addition, the influence of force on PENG and TENG will also lead to the change of nanogenerator output, so it can monitor various mechanical movements of human body (breathing, pulse, heart-beat, swallowing, blood pressure and body movement, etc.). At the same time, various mechanical movements of human body make PENG and TENG have continuous electrical output, so they can be integrated with various biomedical sensors as power sources to continuously supply power to the sensors.

3.1 | Power supply for self-powered systems

Cysteine is an essential glucogenic amino acid in the human body.^{202–204} It is involved in detoxification, prevents

radiation injury, skin whitening, reduces inflammation, dissolves cutin, and prevents aging. The cysteine concentration level in the human body is important; however, the current detection method requires sophisticated instruments and is complex and tedious. Recently, this process was simplified by developing a self-powered cysteine sensor powered by a PENG fabricated from agarose biopolymer and BaTiO₃ nanoparticles with good biocompatibility.¹⁹⁰

The cysteine sensor based on agarose/BaTiO₃-NH₂ films and a TENG comprised of BaTiO₃/agarose film are electrically connected (Figure 9A,B). Current versus potential (I–V) technology is used to test the performance of the cysteine sensor based on the AG/BT-NH₂ film. Phosphate buffer solution containing different cysteine concentrations was measured (Figure 9C).

The inset in Figure 9C is an enlarged portion of the measurement curve at a potential of –4 V, which indicates that the increase in current is linearly related to the cysteine concentration. The corresponding calibration plot is presented in Figure 9D. To test the anti-interference performance of the proposed sensor, urine samples of different concentrations (10–500 μM) were measured, and the results are presented in Figure 9E.

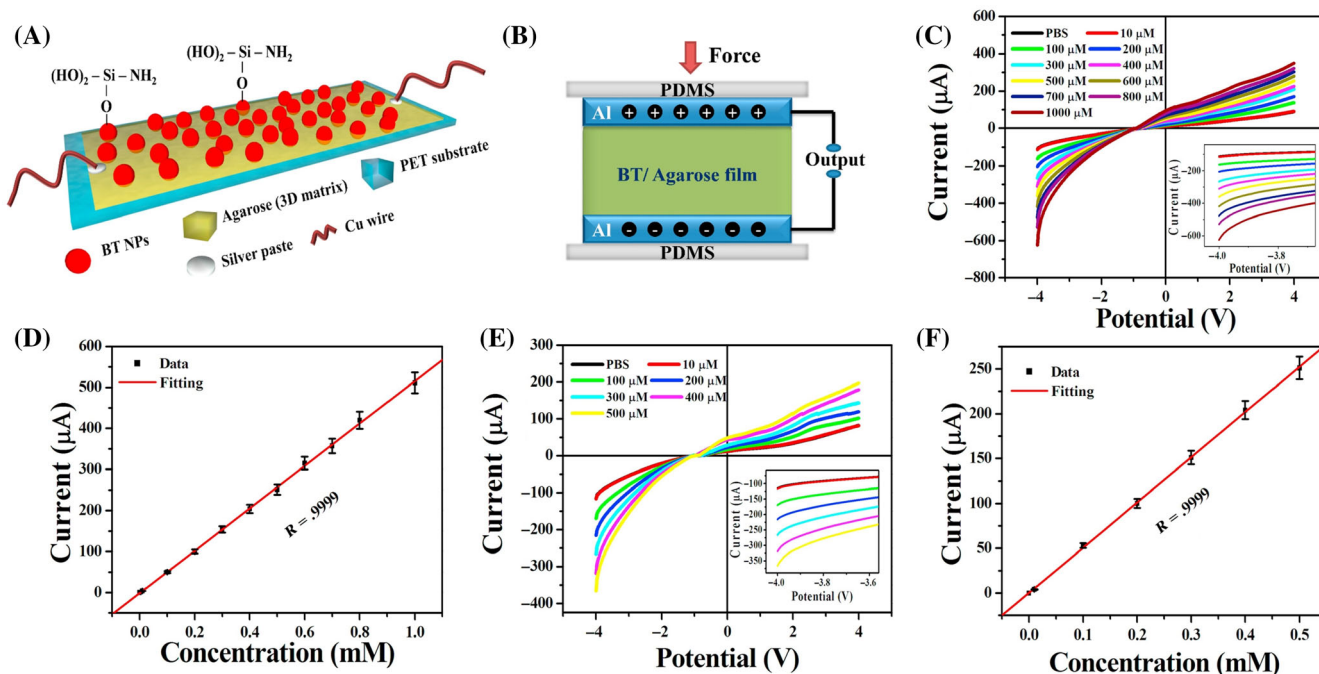


FIGURE 9 Self-powered cysteine sensor driven by a piezoelectric nanogenerator unit of BaTiO₃/agarose film. (A) Cysteine sensor based on agarose/BaTiO₃-NH₂ film. The BT represents the BaTiO₃. The NPs denotes nanoparticles. (B) The scheme of PENG device based on BaTiO₃/agarose film. (C) Current versus potential curve of the cysteine sensor under phosphoric acid buffer solution containing different cysteine concentrations in the potential range from -4 to $+4$ V. The inset is magnified region at a potential range from -4 to -3.5 V. (D) Correlation between current and cysteine concentration. (E) The current versus the concentrations of urine. The inset is an enlarged portion at a potential of -4 to -3.5 V. (F) The output current against the concentration of cysteine. Reproduced with permission.¹⁹⁰ Copyright 2016, Elsevier B.V

The inset in Figure 8E is an enlarged portion of the measurement curve at a potential of -4 V. The increase in current is also linearly proportional to the cysteine concentration (Figure 9F), which is consistent with the measurements in the phosphate buffer solution. In addition, various interfering substances, for example, histidine, glutamine, were tested during the experiment, and the sensor response was almost zero, indicating that the sensor has good anti-interference performance. Finally, the cysteine sensor based on Ag/BT-NH₂ film and the BT/AG PNG were integrated in parallel to test the performance of the entire self-powered sensor. When the concentration of cysteine rises, the voltage of the self-powered sensor showed a monotonic decreasing tendency, indicating good cysteine concentration detection performance.

A self-powered glucose sensor has been proposed based on BaTiO₃ nanoparticles driven by a power source of PENG.¹⁹¹ The electrical connection is presented for the glucose sensor based on a film of BaTiO₃ nanoparticles and a PENG based on a PVDF/BaTiO₃ nanocube film (Figure 10A).

To accurately evaluate the performance of the designed sensor, I - V curve, current versus time (I - t curve), and

anti-interference (galactose and UA) analyses were performed. From Figure 10B-D, the current exhibits an increasing tendency with increase in the glucose concentration, and the sensor shows good response characteristics. Furthermore, the response of the sensor to interfering substances (galactose and UA) is almost negligible, demonstrating good anti-interference performance. In addition, the voltage decrease in the integrated self-powered sensor also shows a good functional relationship with the glucose concentration of the solution (Figure 10E). These results indicate that the proposed self-powered sensor has good detection performance for glucose.

3.2 | Wearable biomedical sensor

Cardiovascular diseases are a common and very serious threat to human health,²⁰⁵⁻²⁰⁹ with a characteristically high prevalence, disability, and mortality rate. Approximately 17.5 million people die every year from cardiovascular diseases worldwide. However, researches show that 90% of cardiovascular diseases can be prevented (research results indicate that approximately 90% of all sudden patient deaths occurred outside the hospital, and

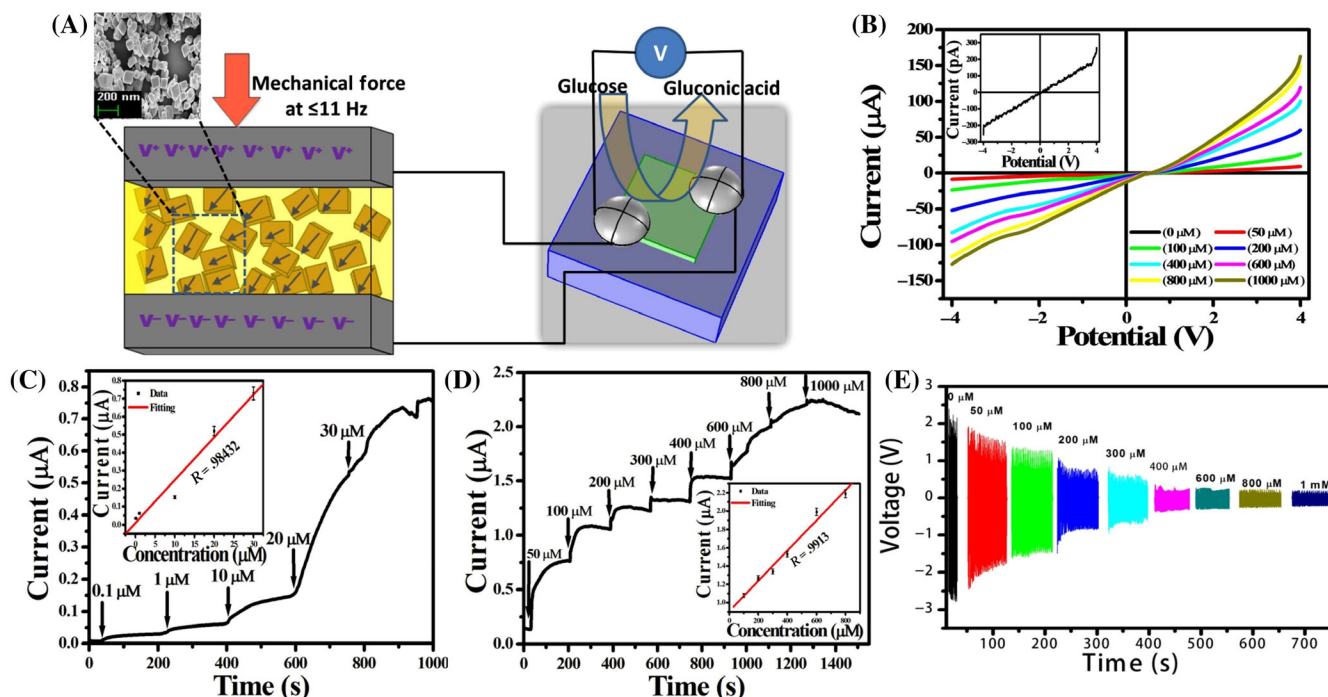


FIGURE 10 Self-powered glucose sensor driven by a piezoelectric nanogenerator of PVDF/BaTiO₃ nanocube film. (A) Glucose sensor based on BaTiO₃ thin films (right), and a power unit of PENG based on PVDF/BaTiO₃ nanocube films (left). (B) Sensor response for solutions of different glucose concentrations. The time dependent current curves for sensors in (C) low and (D) high glucose concentration ranges. (E) The output voltage of the self-powered sensor and the concentration of glucose solution. Reproduced with permission.¹⁹¹ Copyright 2016, Elsevier B.V

resuscitation failed due to failure to access timely medical treatment).

A flexible self-powered ultrasensitive pulse sensor (SUPS) based on triboelectric active sensors can monitor physiological information related to cardiovascular diseases in real time.¹⁹² The design of such a pulse sensor (Figure 11A) comprises two nanostructured friction layers (Kapton and Cu layers), a Cu electrode layer, and a polydimethylsiloxane (PDMS) substrate.

This device can be regarded as a vertical contact-separation mode TENG. Thus, to test the reliability and accuracy at pulse wave monitoring, SUPS, piezoelectric pulse transducer (PPT), and photoplethysmograph (PPG) results were compared with those of an electrocardiograph (ECG). The synchronization between the SUPS and the ECG (ECG100C) is higher than with the PPT (HK2000A) and PPG (TSD270B) (Figure 11B). Therefore, the SUPS has a higher accuracy for pulse wave monitoring. To test the diagnostic efficacy of the SUPS on cardiovascular diseases, heart rate variability changes between the pulse waveform and heartbeat of healthy people. And different cardiovascular disease patients were evaluated and compared. The results show evident differences between healthy groups, unhealthy groups, and between different healthy groups, demonstrating that the SUPS

provides good diagnostic and differential diagnostic capability.

Because of the high accuracy of the SUPS, it may be advantageous for pulse wave velocity (PWV) measurement. Therefore, PWVs of 24-year-old male adults before and after jogging 500 m were measured (Figure 11C). Changes in the measured PWV values are equivalent to those measured using a practical tonometer under the same conditions, indicating that the SUPS can sense PWV changes. Finally, the signal output of different artery positions in the human body (Figure 11D and pulse changes during different human activities (Figure 11E) was measured. The results show excellent monitoring and diagnostic performance of the SUPS (Figure 11F).

Sensor and wearable electronics technologies have rapidly developed with the advances of textile materials. Indeed, textile materials are the main component of daily wear articles such as clothes, belts, and various ornaments. Thus, wearable sensors of different textile materials have been reported.^{210–212}

A machine-washable textile TENG (t-TENG) has been developed for effectively monitoring human respiration.¹⁹³ The designed t-TENG (Figure 12A) is woven directly from copper-coated polyethylene terephthalate

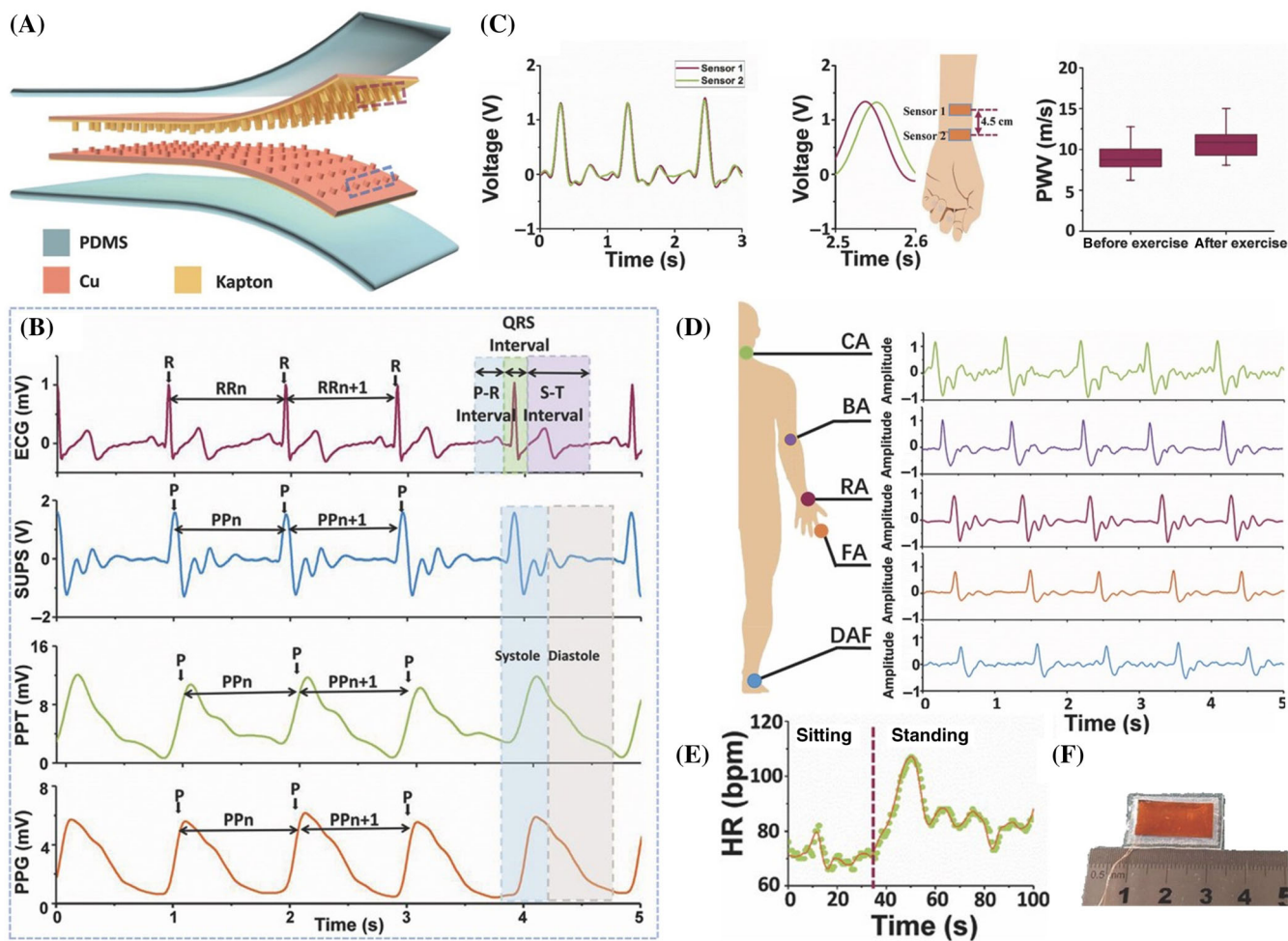


FIGURE 11 Flexible SUPS based on triboelectric active sensors (the carotid artery, the brachial artery, the radial artery, the finger). (A) Structural diagram showing the SUPS design. (B) Pulse wave monitoring comparison. (C) PWV measurement test. (D) Signal output at different artery positions in the human body. (E) Pulse changes during different human activities. (F) Photograph of the designed SUPS. Reproduced with permission.¹⁹² Copyright 2017, Wiley-VCH Verlag GmbH

(Cu-PET) warp yarn and polyimide-coated Cu-PET (PI-Cu-PET) weft yarn.

Figure 12B presents a photograph of the final t-TENG (each overlapping point of the designed t-TENG is a miniature TENG), and Figure 12C presents a cross-sectional scanning electron microscopy (SEM) image of the t-TENG. The PI of the PI-Cu-PET weft yarn is the friction layer, and the Cu layer serves as the electrode. The Cu of the Cu-PET warp yarn functions as both friction layer and electrode. As the oval contact area of the overlapping point (Figure 12D) changes, the t-TENG generates current. To test the performance of the designed t-TENG in respiratory monitoring, a t-TENG wearable chest strap was fabricated and worn on a human chest for respiratory data collection (Figure 12E). Figure 12F presents the actual measured respiratory signals, with a clearly visible complete respiratory cycle.

By processing the original recorded signals, and a sine wave shape was obtained (Figure 12G). Subsequently,

tests were performed for different respiratory modes (deep, shallow, fast, and slow). The original recorded signals are presented in Figure 12H, and the different responses of the t-TENG to the four respiratory states are clearly observable. Finally, the washability of the designed t-TENG was tested. After 20 repeated standard washings, the Cu-PET yarn had no apparent cracks, demonstrating high reliability. The success of this new t-TENG indicates the potential of textile materials in the field of healthcare.

The energy source of a self-powered wearable sensing system primarily derives from human activity and the host environment. The thermal energy, generated via the thermoelectric effect, is considerably abundant in daily life as a good self-powered energy choice. With the development of the pyroelectric nanogenerators, this concept has attracted great attention.^{213–215}

A wearable PyENG based self-powered respiratory sensor has been proposed for harvesting respiratory

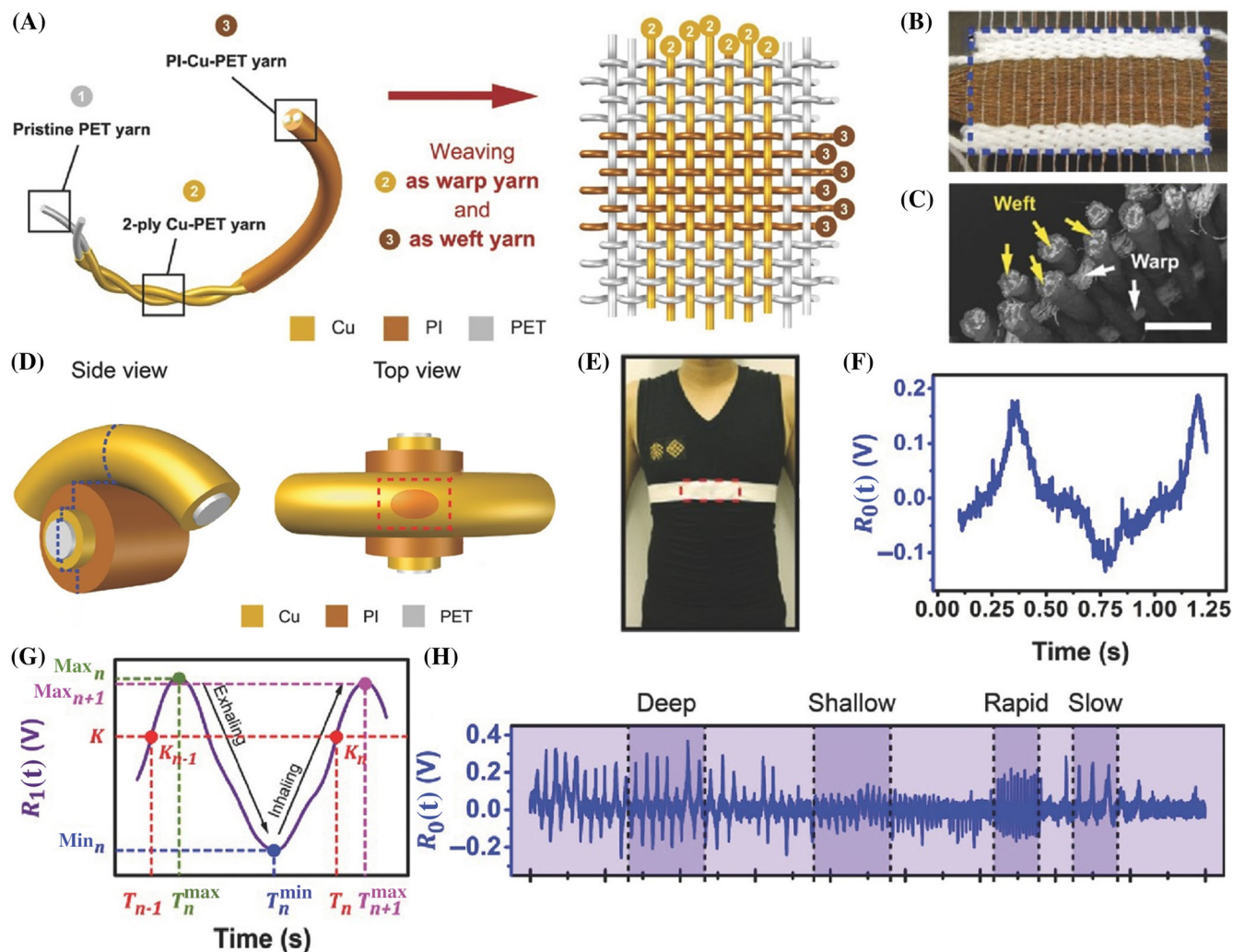


FIGURE 12 Machine-washable t-TENG. (A) Manufacturing process for the t-TENG. (B) Photograph of the final t-TENG. (C) Cross-sectional SEM view of the t-TENG. (D) Each overlapping point of the t-TENG forms a miniature TENG. (E) Wearable t-TENG chest strap worn across a human chest. (F) Raw measured respiratory signals. (G) Waveform obtained after processing the original signals. (H) Test responses for different breathing patterns. Reproduced with permission.¹⁹³ Copyright 2016, Wiley-VCH Verlag GmbH

energy, respiratory detection, and ambient temperature detection.¹⁹⁴ The PyENG (Figure 13A) has a three-part structure: one PVDF film as a thermoelectric material and two Al films as the top and bottom electrodes. A self-powered wearable respirator is obtained with the installation of a PyENG on a N95 respirator (Figure 13A).

When the self-powered wearable respirator operates, breathing causes dynamic changes of temperature at the point in front of the mouth, reaching changes in the order of 12°C. This temperature change drives the PyENG, with the maximum open-circuit voltage and maximum short-circuit current reaching 42 V and 2.5 μ A, respectively.

The respiration leads to a periodic temperature change in the PVDF film, which causes periodical changes in the polarization density of this film and induces an alternating current. For example, the electrical signals of different respiratory states measured using

the designed self-powered respiratory sensor are clearly distinguished (Figure 13B,C). The output of the PyENG also exhibits a good linear relationship with the ambient temperature (Figure 13D), except during the breathing state. In addition, the PyENG can charge a 10.0 μ F capacitor to 1 V (Figure 13E) within 18 s after simple rectification, and it can also directly provide continuous power for electronic watches (Figure 13F, i) and light up eight LEDs (Figure 13F, ii). Thus, the wearable self-powered respiration sensor is expected to integrate energy harvesting, respiration monitoring, and temperature detection, and the device shows good development potential.

Furthermore, nanogenerators with hybrid structures have been manufactured to improve outputs. However, most of these hybrid nanogenerators^{184,216,217} have complex structure and poor flexibility, which considerably limits their application in wearable devices.

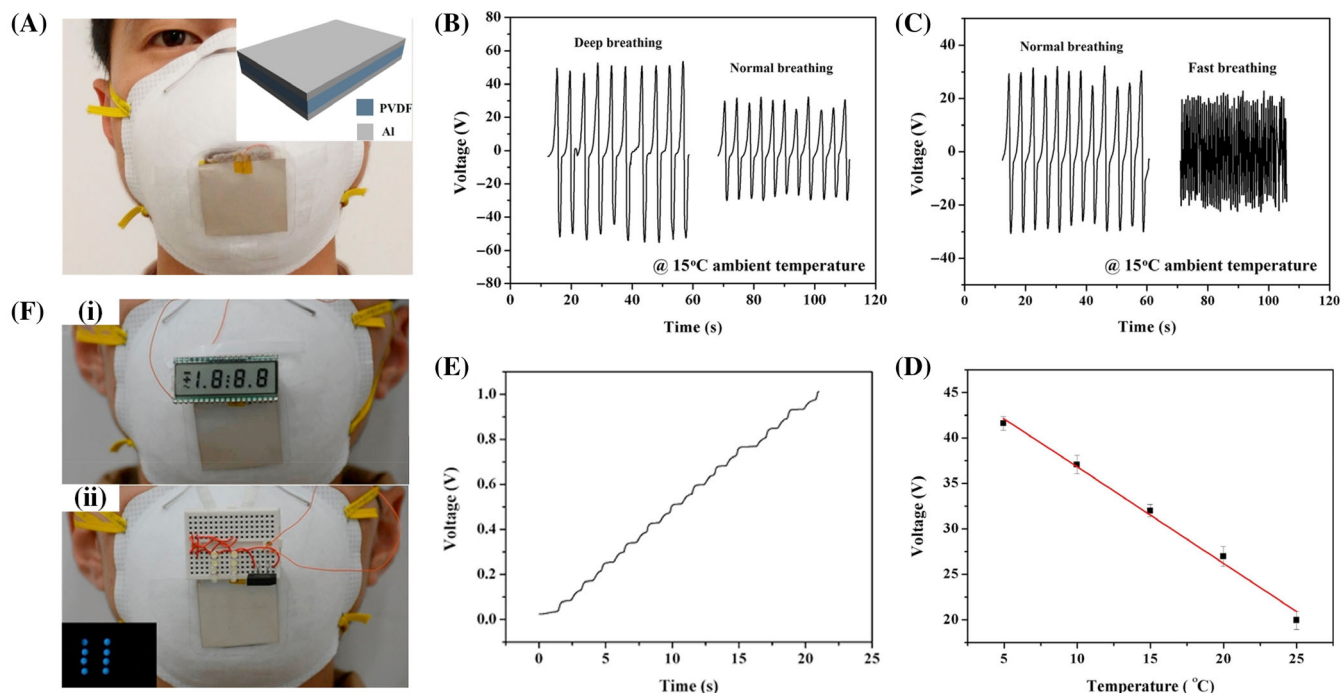


FIGURE 13 Wearable PyENG and self-powered respiratory sensor. (A) Structure of the PyENG and self-powered wearable respirator. (B) Electrical signals for deep, (C) fast, and normal breathing states. (D) Relationship between the PyENG's output and the ambient temperature. (E) The PyENG charges the capacitor after simple rectification, (F) directly and continuously supplies power to an electronic watch (i), and lights up eight LEDs (ii). Reproduced with permission.¹⁹⁴ Copyright 2017, Elsevier Ltd

A tribo-piezo-pyroelectric hybrid nanogenerator¹⁹⁵ has been designed for simultaneously harvesting mechanical and thermal energies. The nanogenerator can be attached to different points on the human body for real-time monitoring of human vital signs such as respiration, heartbeat, and body temperature.

The structure of the designed hybrid nanogenerator (Figure 14A) consists of a PVDF nanofiber piezoelectric layer fabricated via electrospinning, a high-performance transparent electrode (TE) with nanowires drawn in a leaf venation (LV) pattern on both surfaces, and a PDMS film encapsulation layer as the outermost layer. The PDMS film on the bottom layer of the device also serves as a friction layer when contacting human skin. Figure 14B presents a photograph of the designed hybrid nanogenerator mounted on the wrist.

The transparent electrodes of leaf venation-like nanowires were prepared via modified dry transfer printing technology using a skeleton of leaf venation as a mold, with 0.1 ml volume of prepared Ag nanowire solution used to achieve an LV nanowire transparency of approximately 99% (Figure 14C). The generator can harvest mechanical energy from the human motion because of the coupling effect of triboelectric and piezoelectric mechanisms. In addition, the thermoelectric effect can overcome temperature fluctuations between the human body and the surrounding environment, and, consequently, the generator can also harvest

thermal energy. The operating mechanism is presented in Figure 14D. Due to periodic pressure on the surface of the hybrid nanogenerator, the two friction layers (human skin and PDMS film) of the TENG constituent continuously contact and separate, while the PENG constituent continuously undergoes a deformation and recovery process, enabling both the TENG and PENG operations to harvest mechanical energy during the pressure and release process.

The instantaneous open-circuit voltages of the TENG-PENG and PyENG are 55 and 86 V, respectively. The designed hybrid nanogenerator was fixed at different points on the human body to monitor different vital signs in real time, including pulse (Figure 14E), swallowing (Figure 14F), body temperature (Figure 14G), cough (Figure 14H), and respiratory state (Figure 14I). Furthermore, when the hybrid nanogenerator is placed on a respirator, thermal energy can be harvested via a PyENG operation due to the temperature gradient created by the difference between the respiration and the ambient temperature. The device shows considerable development potential in medical diagnosis and healthcare monitoring.

3.3 | Implantable biomedical sensor

According to the World Health Organization (WHO), 466 million of people (including 34 million of children)

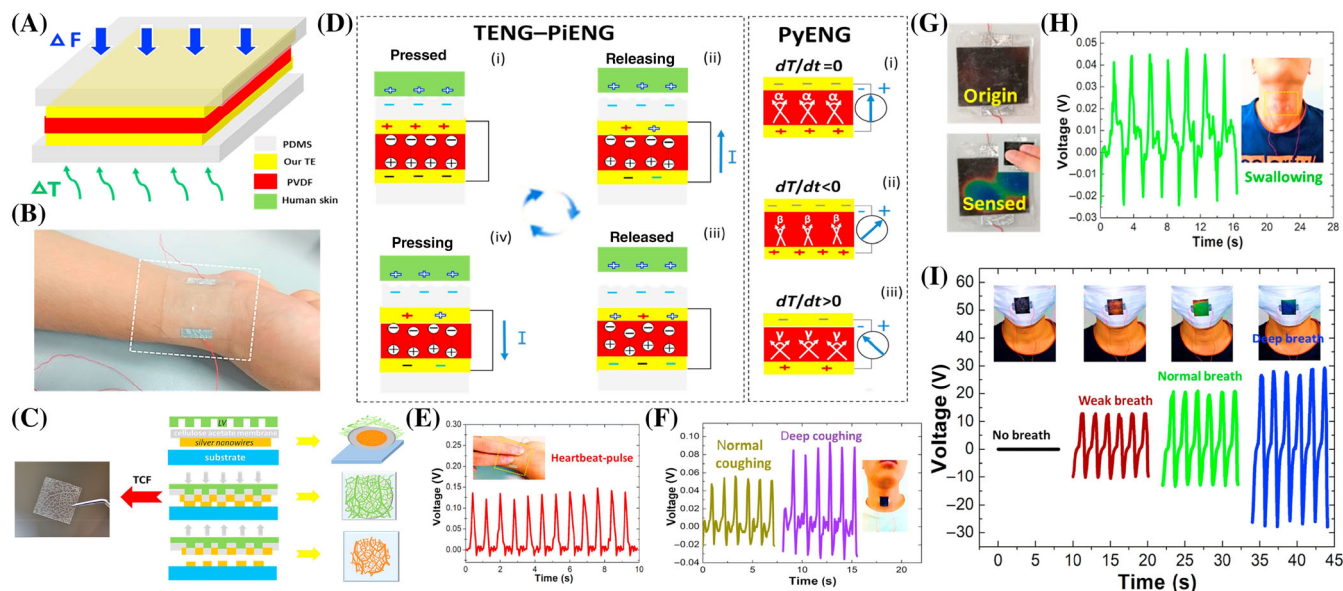


FIGURE 14 A single structure, flexible, biocompatible tribo-piezo-pyroelectric hybrid nanogenerator. (A) Structural diagram of the designed hybrid nanogenerator. (B) Photograph of the hybrid nanogenerator mounted on the wrist. (C) Manufacturing process of the TE. (D) Operating mechanism of hybrid nanogenerators used for monitoring of different human vital signs, including (E) pulse, (F) swallowing, (G) body temperature, (H) coughing, and (I) respiratory state. Reproduced with permission.¹⁹⁵ Copyright 2018, Elsevier Ltd

suffer from hearing loss, which represents 5% of the global population.²¹⁸ Predictions indicate that this number will increase to more than 900 million by Year 2050, which is equivalent to 10% in human population. At present, hearing problems have become a key health issue. When the hearing loss is severe and hearing aid assisted hearing is suboptimal, a cochlear implant becomes the only option for hearing reconstruction. However, the cochlear implant currently has many disadvantages, for example, it is inconvenient during daily activities such as bathing, swimming, and sleeping, requires frequent charging, and has high cost. These challenges result in reluctance to consider the cochlear implant, despite its extensive use in clinical solutions.

A triboelectric-based artificial basilar membrane (TEABM) can simulate the topology of the cochlea and has low cost, simple manufacture, and is self-powered.¹⁹⁶ The designed TEABM (Figure 15A) is composed of eight TENGs in a beam structure. Here, the Kapton film and Al foil work as the friction layers of different lengths and widths. A photograph of the TEABM device shows its eight-beam channel structure (Figure 15B) and its power generation process is presented (Figure 15C). When stimulated by sound waves, the two friction layers contact to generate frictional charges. When the sound waves disappear, the two friction layers rebound. Due to the difference in the Young's modulus of the two materials, a gap appears between them in the rebound process, generating a potential difference that drives current through an

external load. After the maximum gap is reached, the two materials fall until they contact again, during which the charge flows in reverse.

To verify the response of the artificial basilar membrane to sound, the displacement and open-circuit voltage of its fourth channel were tested (Figure 15D,E). The maximum peak value at 669 Hz reflects the resonant frequency of the channel, and the inset is the applied sound input. The open-circuit voltage test results show a maximum peak value at 669 Hz (Figure 15F,G). It has been proved that the fabricated TEABM has a good response to sound. The designed TEABM was also analyzed using Hartley guinea pigs. The experiment (Figure 15H) tested the second channel of the TEABM at 1340 Hz (resonant frequency of channel 2). The recorded evoked auditory brainstem responses under 85 dB acoustic stimulation are presented in Figure 15I, and the positive and negative peaks (P2 and N1) are clearly visible. The recording of evoked auditory brainstem response with a sound pressure level of 70–85 dB shows that the average amplitude of N1-P2 increases with increase in the input sound pressure level (Figure 15J). Therefore, triboelectric artificial basilar membrane can convert sound stimulus into electrical voltages to induce auditory evoked potentials in deaf animal models.

Heart failure refers to a dysfunction in the heart's systolic and diastolic functions, such that the venous return blood volume from the heart cannot be fully discharged, resulting in venous system blood stasis and insufficient

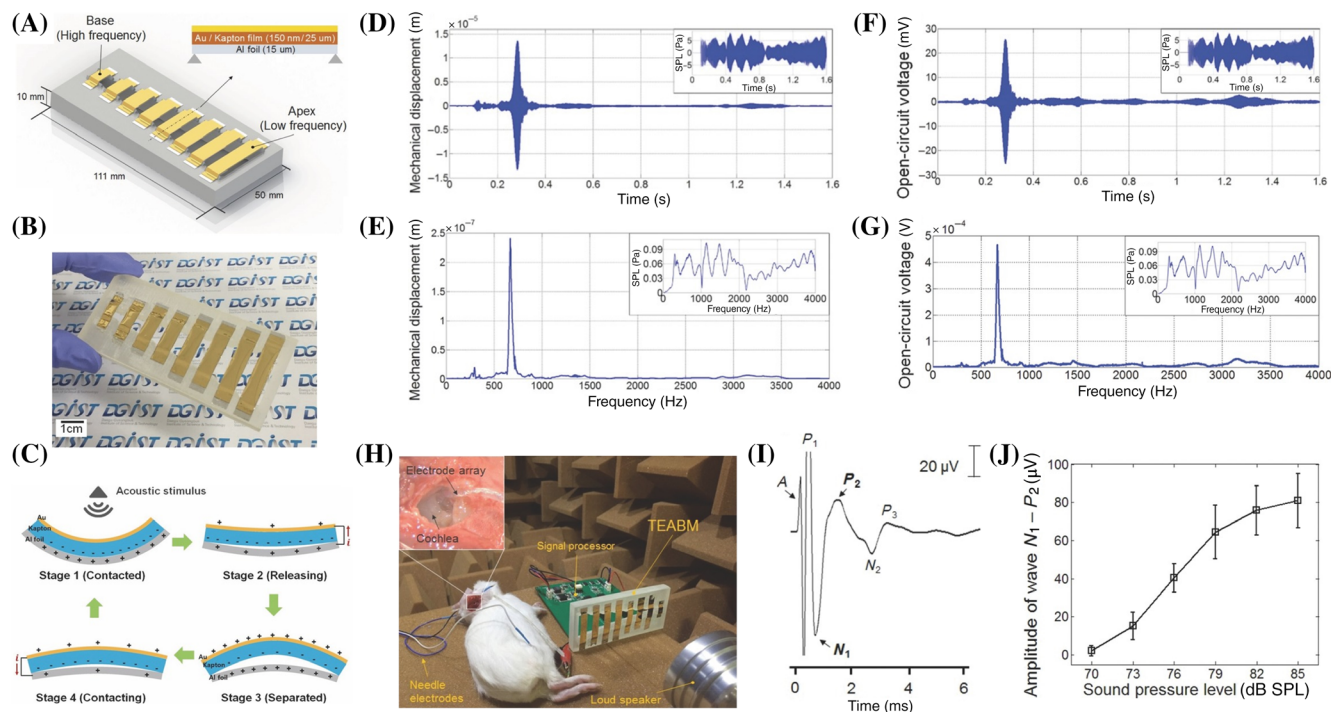


FIGURE 15 A triboelectric-based artificial basilar membrane for stimulating cochlea. (A) Structural diagram and (B) photograph of the artificial cochlea device based on basilar membrane. (C) The power generation mechanism by sound activation. (D) Test of displacement and (E) open-circuit voltage of the fourth channel of the device. (F) Open-circuit voltage output generated by sound stimulation. (G) Frequency response of the open-circuit voltage. (H) Photograph of experimental apparatus for testing the artificial basilar membrane implanted in an animal model. The artificial cochlea was implanted in a Hartley guinea pig for assisting the hearing. The TEABM denotes the triboelectric artificial basilar membrane. (I) The recording of evoked auditory brainstem response under acoustic stimulation of 85 dB. (J) Recording of the evoked auditory brainstem response with sound pressure level ranging from 70 to 85 dB. Reproduced with permission.¹⁹⁶ Copyright 2016, Wiley-VCH Verlag GmbH

blood perfusion in the arterial system. This results in cardiac circulation disorder, a disorder syndrome primarily manifested as pulmonary and vena cava congestions. Heart failure is a major public health problem^{219–221} that affects thousands of people around the world and forces many people into a vicious circle of hospitalization, discharge, and readmission. Some cardiologists classify this disease as an epidemic due to its lack of control. Approximately 26 million people are estimated to suffer from heart failure worldwide, and this number is expected to continuously increase in the coming decades as the population ages.

Change in endocardial pressure is an important parameter for evaluating cardiac function and thus has critical clinical significance for patients with heart failure and impaired cardiac function. A small, flexible, self-powered endocardial pressure sensor based on TENG¹⁹⁷ has minimally invasive implantation (Figure 16A).

The structural schematic diagram of such a sensor is presented (Figure 16B). A PTFE film is the friction layer, an Au layer deposited on a back surface serves as an electrode layer, and Kapton film on the back surface of the Au layer serves as a flexible substrate. An Al foil functions as a second friction material and as the electrode

material. PTFE and PDMS constitute the outer packaging, and a three-dimensional (3D) ethylene-vinyl acetate (EVA) copolymer film is the spacer layer between the two friction layers.

Hundreds of millions of cycles of experiments have been performed in a physiological saline environment to study the durability of the designed SEPS, and the results show that the output state of the SEPS remained stable. The encapsulation layer of the SEPS was tested to verify the compatibility between the SEPS and blood. The test shows that the designed encapsulation layer of the SEPS has an average hemolysis rate (1.08%) far lower than the required in the standard set by the International Standard Organization (5%), and also has no influence on the cell morphology of red blood cells. The SEPS was tested at different pressure levels in a closed chamber to evaluate its pressure response. The voltage of the SEPS is proportional to the pressure (Figure 16C), showing good sensitivity (Figure 16C slope inset).

Eventually, to evaluate the actual monitoring performance in the human body, an adult male Yorkshire pig (40 kg) was used in verification experiments. Because most heart failure cases start with left heart failure, the

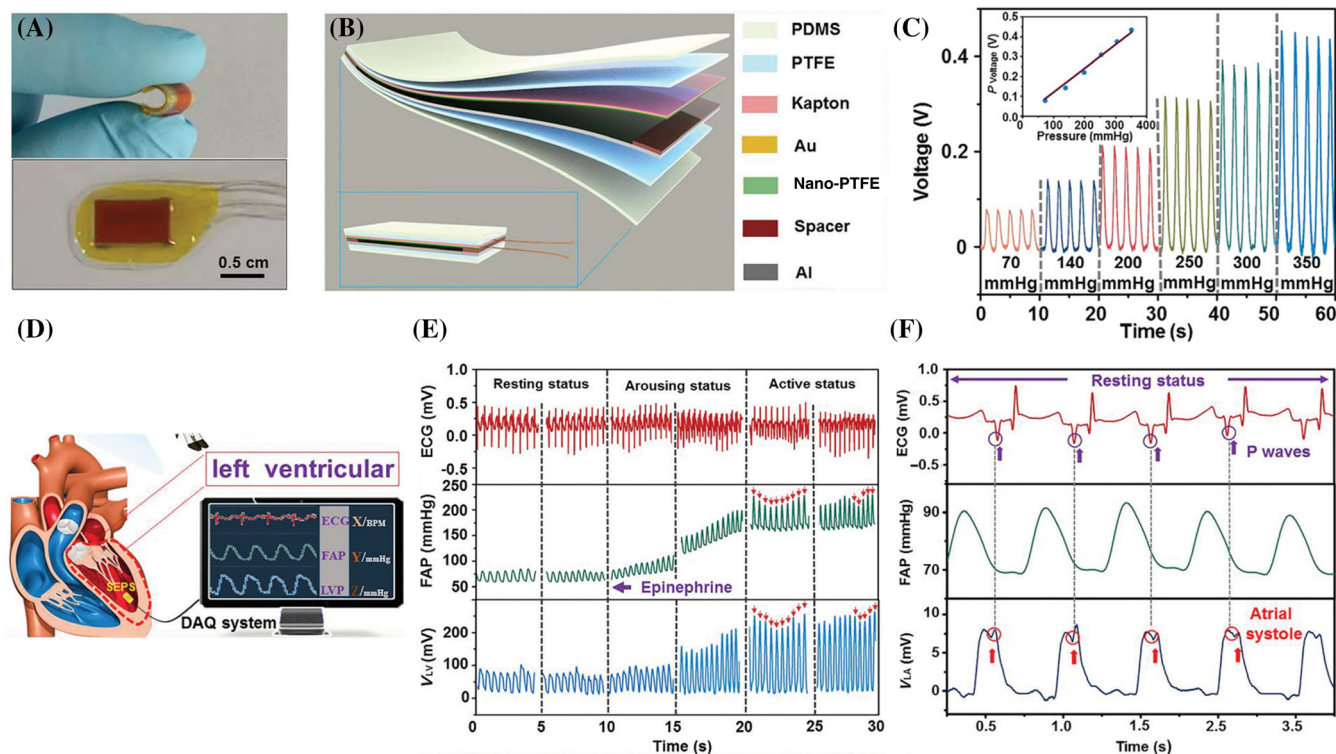


FIGURE 16 SEPS based on the TENG (DAQ: data acquisition). (A) Photograph of the designed SEPS. (B) Structural diagram of the SEPS. (C) Pressure response test of the SEPS (inset is a slope). (D) Schematic diagram showing the SEPS implanted in the heart of an adult Yorkshire pig to obtain signals. (E) Data from the SEPS implanted in the left ventricle compared with ECG and FAP signals for different cardiac active states. (F) Comparison of data from the SEPS implanted in the left atrium with ECG and FAP signals. Reproduced with permission.¹⁹⁷ Copyright 2018, Wiley-VCH Verlag GmbH

designed SEPS was implanted in the left ventricle and left atrium of the pig for testing. First, the SEPS was implanted in the left ventricle of the pig (Figure 16D). A comparison of data on the SEPS with ECG and femoral arterial pressure (FAP) signals are presented in different active states (Figure 16E). This indicates that the operating signals of the SEPS have good output stability and exhibit the same tendency as those of the FAP. The SEPS was then implanted in the left atrium of the pig, and the SEPS data was also compared with ECG and FAP data. The SEPS was able to capture even relatively small changes in the left atrial pressure (LAP), and the measured signal change was almost completely synchronized with the ECG and FAP signals (Figure 16F). These experimental results indicate that the designed SEPS has good reliability, biocompatibility, and sensitivity, and can be used for monitoring intracardiac pressure.

4 | APPLICATION OF THE NANOGENERATOR IN BIOMEDICAL THERAPY

The increasing research in nanogenerators and biomedical equipment provided an increase in the application of

nanogenerators in the biomedical field. The rapid development of nanogenerators was observed for applications in biomedical sensors and also in biomedical treatment.²²² At present, nanogenerators exhibit considerable potential for power supply in biomedical devices,^{6,223} promotion of cell proliferation and differentiation,^{224,225} drug delivery,^{226,227} and direct electrical stimulation.^{228,229} Table 4 summarizes some of the direct applications of nanogenerators for biomedical treatment.

4.1 | Power supply

Microspheres, due to their simple structure, are widely used in biomedicine, for example, injection therapy, 3D cell culture, and drug carriers. The construction of miniature organs using microspheres has become a focus of research.²³⁴ Two major problems need to be solved in the construction of mini-tissue from microspheres: obtain a bio-hydrogel with excellent biological properties and develop a quantifiable and stable production process based on the hydrogel. At present, there are two main technologies for producing microspheres, that is, air-jet stream²³⁵ and electro-assisted printing method.²³⁶ The air-jet method is cheap and easy to master. However, the

TABLE 4 The performance and application of nanogenerator for biomedical treatment

Medical applications	Nanogenerator types	Materials	Nanogenerator size	Output performance	Monitored parameters	Working principle	References
Electro-assisted cell printing	TENG	PVC films and nylon	30 × 30 cm	V_{OC} : 4 kV I_{SC} : 80 μ A The input frequency is 40 Hz (experimental test)	Power the cell solution in vitro	Use the high voltage generated by TENG to drive cell printing	230
Transdermal drug delivery (TDD)	TENG	PTFE and Al	15 × 15 cm	V_{OC} : 4 V I_{SC} : 12 μ A The input frequency is 2 Hz	Drug patches	The output of TENG accelerate the TDD rate	227
Cell reprogramming	TENG	Al and PDMS	1 × 2.5 cm	V_{OC} : 30 V I_{SC} : 280 nA The input frequency is 1 Hz	Cell culture substrate	TENG produces electrical stimulation to facilitate direct cell conversion	231
Cardiac pacemaker	PENG	A single crystalline PMN-PT thin film	1.7 × 1.7 cm	V_{OC} : 8.2 V I_{SC} : 145 μ A (a strain of 0.36%, a strain rate of 2.3% s^{-1} , and a frequency of 0.3 Hz)	A rat heart	PENG generates electrical energy via periodic bending/unbending cycles to stimulate the heart	232
Deep brain stimulation	PENG	A single crystalline PIMNT thin film	1.7 × 1.7 cm	V_{OC} : 11 V I_{SC} : 283 μ A (a strain of 0.3%, a strain rate of 2.3% s^{-1} , and a frequency of 0.32 Hz)	The M1 cortex in the mouse brain	The electricity harvested by PENG directly stimulated a certain area of the animal brain to induce corresponding body movements	228
Bone remodeling or orthodontic treatment	TENG	Polydimethylsiloxane (PDMS) and indium tin oxide (ITO)	Not mentioned	V_{OC} : 115 V I_{SC} : 30 μ A (experimental test)	Cell culture substrate	The SPLC system consisting of TENG and infrared laser excitation units accelerates cell proliferation and differentiation	233

microspheres produced are usually large and uneven (400–1200 μ m), which is unsuitable for quantitative production. Electro-assisted cell printing can produce monodisperse, bioactive microspheres with precise control of distribution and size, thus being a suitable method for quantitative production. However, the demand for high-voltage power supply equipment makes the method relatively expensive.

A simple, safe, and efficient triboelectric cell printing unit (TCPU) was employed for 3D cell culture.²³⁰ Structural of the unit are presented (Figure 17A). The system comprises a liquid supply device, a power supply, a voltage multiplier rectifier circuit (VMRC), and a basic printing device. Because the power supply principle of the designed TCPU is quite different from that of traditional commercial high-voltage power supply, it is necessary to study the influencing factors of microsphere printing.

The control variable method was used to study the influence of $CaCl_2$ concentration, sodium alginate (NaAlg) mass fraction, pump propulsion speed, motor speed, electrode distance, and needle diameter on the diameter and perfection of microspheres (Figure 17B). Subsequently, appropriate parameters were selected based on the results of previous experiments on factors influencing microspheres, and HepaRG and HeLa cells were selected for 3D cell culture experiments. Fluorescence staining images of two-dimensional living (green) and dead (red) cells are representing HepaRG cells (Figure 17C) and 3D HeLa cells (Figure 17D). The 3D HeLa cells show good cell viability. Finally, the cells in the printed microspheres were

compared with unprinted cells suspended in bio-ink (Figure 17E). Both the HepaRG and HeLa cells had cell survival rates higher than 92% in the printing experiment for cell-loaded microspheres, and showed no significant difference when compared with unprinted bio-ink suspension cells. The experimental results indicate that the TENG can be well applied to electrically assisted cell printing and subsequent biomedical applications.

Transdermal drug delivery (TDD) is a drug-delivery method in which drugs are coated or applied on the skin surface.^{237,238} This method employs chemical, physical, and pharmaceutical methods to enhance penetration of the target drug through the skin to the relevant circulatory system of the body to achieve the purpose of preventing or treating a disease. With changes in the modern concept of diagnosis and treatment, the emergence of this drug-delivery method has created a new tendency, and it has become the third largest drug administration method after injection and oral administration. The transdermal administration route has the advantages of convenience, simplicity, safety, lasting drug effect, absence of liver first-pass effects, gastrointestinal tract inactivation, and reduction of toxic and side effects.

However, transdermal drug delivery has limitations. The most significant limitation is that the barrier effect of the stratum corneum limits the transdermal absorption of drugs, hindering the transdermal rate and penetration amount to meet treatment requirements. Presently, various technologies have been developed to facilitate and enhance drug absorption through the skin,^{239–242} and

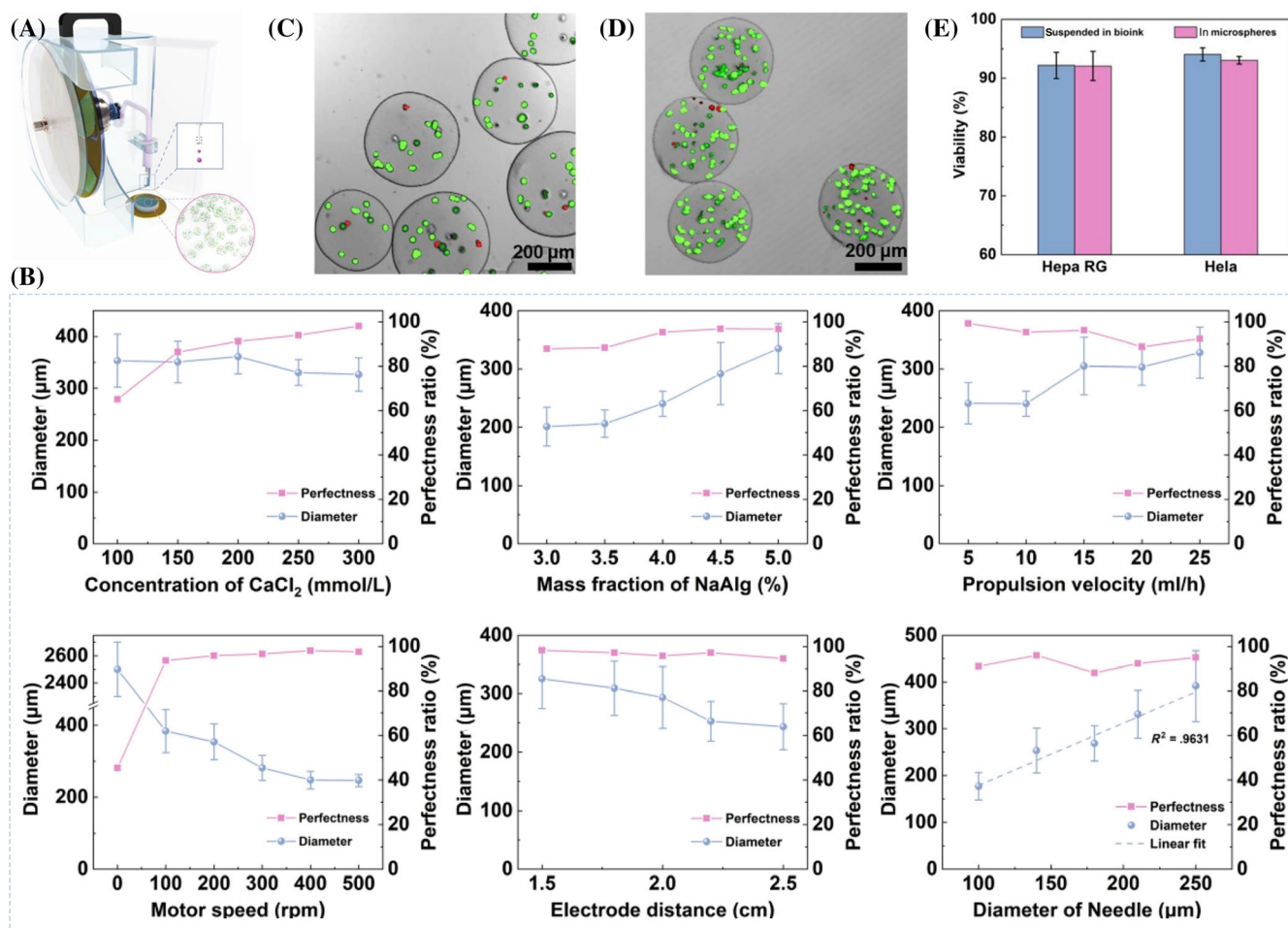


FIGURE 17 TENG for electro-assisted cell printing. (A) Structural diagram of the designed TCPU. (B) Degree of influence of different factors on microsphere printing. (C) Fluorescence staining image of two-dimensional living (green) and dead (red) HepaRG and (D) HeLa cells. (E) Comparison of survival rates of cells in printed microspheres and unprinted cells suspended in bio-ink. Reproduced with permission.²³⁰ Copyright 2019, Elsevier Ltd

penetration enhancement methods for transdermal drug delivery have become the focus of research in the industry.^{243,244} The commonly used penetration enhancement methods include chemical, physical, and pharmaceutical methods. Particularly, a growing number of industry experts have focused on physical methods of enhancing transdermal drug absorption.

According to experts, physical penetration enhancement methods can precisely control percutaneous absorption by controlling external forces, and can effectively expand the types of drugs that can be used in transdermal drug delivery, specifically proteins and peptides. Consequently, several new penetration enhancement technologies have emerged, including iontophoresis, electroporation, ultrasonic introduction, and microneedles. Iontophoresis can transfer hydrophilic and charged molecules to various parts of the skin and has been proved to be an effective method. This method has been commercialized and often used in scientific experiments, drug release and clinical diagnosis.

However, the large and expensive energy storage, power supply demand, and complicated feedback control limit the use of such electronic control patches.

A self-powered wearable iontophoresis based transdermal drug-delivery system has been reported via biomechanical motion sensing and energy harvesting for closed-circuit motion detection and treatment.²²⁷ This transdermal drug-delivery system comprises a wearable TENG, which can be used as a power supply, and a soft patch that can be used as a drug carrier. The TENG can be installed in different parts of the human body to harvest mechanical energy via various bodily movements, and the soft patch is attached to the skin as the medicine supply source. The two components are connected via wires, and the electrical energy converted by the TENG is used as a power supply to accelerate the drug-delivery speed of the transdermal drug-delivery system.

To verify the feasibility of this scheme, an experiment was conducted using a diffusion cell with four units

separated by a cellulose membrane. The experimental schematic diagram is presented in Figure 18A. First, the effect of the direction of the electric field on the dye transport rate was tested. The transport amount of rhodamine 6G (R6G) and methylene blue (MB) in the receptor cells significantly increased under direct voltage, but decreased under inverse voltage (Figure 18B). Here, the positive electric field accelerates the dye transport rate. To further verify the actual performance of this scheme, soft patch devices and a wearable TENG were designed. The hydrogel-based drug soft patch device (Figure 18C) contains two side-by-side hydrogel units and two carbon cellulose electrodes embedded in a PDMS frame. In the experiment, a poloxamer 407 hydrogel with reversible sol–gel characteristics was applied. The gel can change between liquid and semisolid state when the temperature is close to its gel transition temperature (Figure 18D), which makes poloxamer 407 hydrogel suitable for loading drugs, provides good contact with the skin, and makes it easily detachable.

The designed wearable TENG (Figure 18E) comprises three TENG units with the same structure. Each TENG unit has PTFE as a friction material, Al as friction material and electrode, Kapton as a spacer, and PET as the

substrate. The designed wearable TENG has good output performance. At 2 Hz, the maximum open-circuit voltage, charge transfer per cycle, and maximum short-circuit current were 1200 V, 370 nC, and 20 μ A, respectively. Finally, the designed drug soft patch device and wearable TENG were integrated for a transdermal drug-delivery test on pigskin (Figure 18E). For an accurate evaluation of the performance of the designed iontophoresis TDD system driven by a TENG, a controlled test was conducted under the same experimental conditions except for the exclusion of the TENG drive. The results (Figure 18F) clearly indicate that the drug delivery reaches deeper parts of the skin when the device is driven by a TENG.

4.2 | Direct application in biological therapy

Somatic reprogramming refers to a process in which differentiated somatic cells are reversed to a pluripotent or totipotent state, which is the basis of tissue repair, organ reconstruction, and the development of individualized regenerative medicine.^{245–249} Somatic cell reprogramming is primarily realized via nuclear transfer. However, other

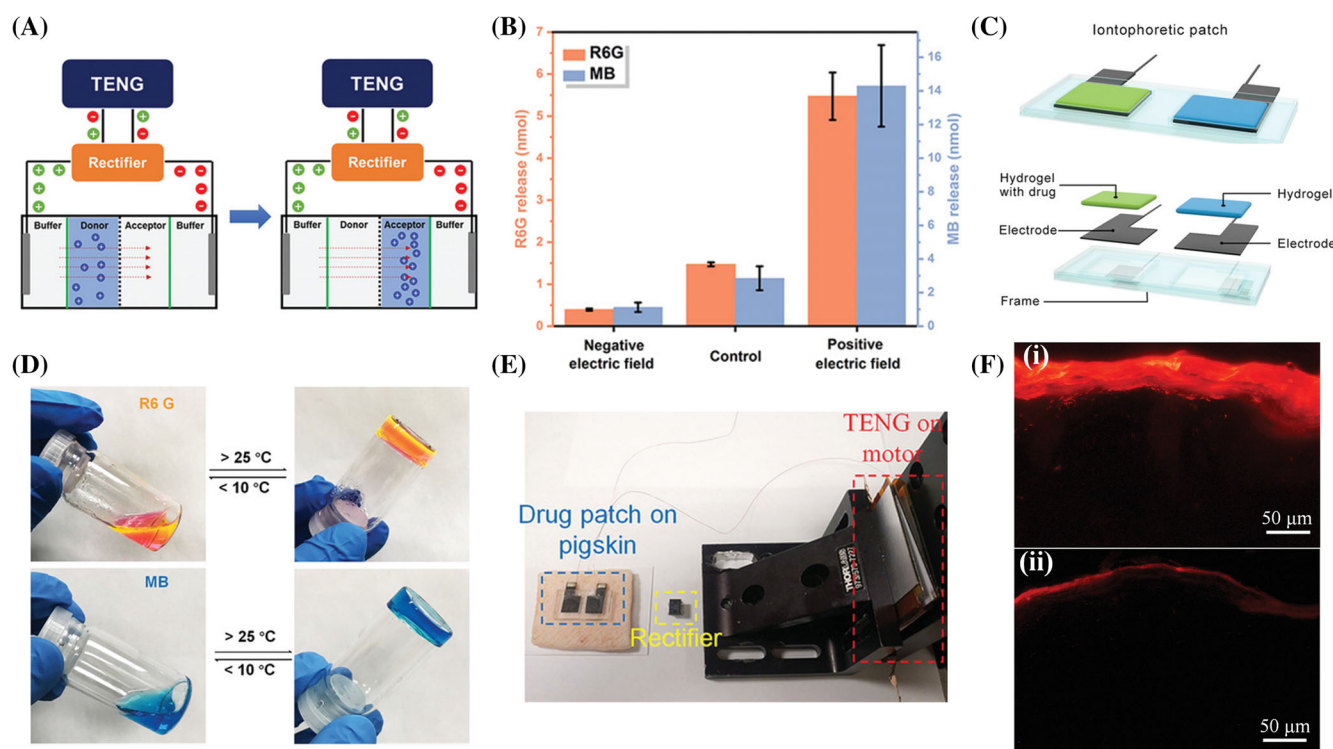


FIGURE 18 Self-powered wearable iontophoresis TDD system. (A) Schematic diagram of the experimental device using the diffusion unit. (B) Influence of electric field direction on R6G and MB transport. (C) Schematic diagram of the structure of the drug soft patch equipment. (D) Photographs of hydrogels of different dyes switching between fluid and semisolid states. (E) Diagram of experimental device for TDD test on pigskin. (F) Fluorescence cross-sectional histological images of skin after R6G delivery from the patch with a TENG (i), and with no TENG connected (ii). Reproduced with permission.²²⁷ Copyright 2019, WILEY-VCH Verlag GmbH

methods can be used, such as the artificial introduction of specific transcription factors into somatic cells.^{250,251} Dr. Yamanaka from Japan won the 2012 Nobel Prize in Medicine or Physiology for this pioneering work. This technology not only avoids the ethical debate provoked by nuclear transplantation but also inspires positive expectations for cell therapy and regenerative medicine.

With lineage reprogramming, which is based on the similar induced pluripotent stem cells (iPSCs) technology, a specific type of somatic cell can be directly transformed into another type of somatic cell without the iPSCs stage. Fibroblasts are the most commonly used starting cells for studying cell reprogramming as they are readily obtainable, have abundant sources, and provide incomparable advantages in iPSCs database construction and future clinical applications. It has been proved that skin fibroblasts can be directly reprogrammed into various types of somatic cells, for example, myocardium, nerve, blood, liver, and endothelium cells. Compared with the scheme of inducing iPSCs to form and then directionally differentiate the stem cells into target cells, the operation flow of lineage reprogramming is relatively simple, and the risk of tumor formation from undifferentiated cells is removed.

However, pedigree reprogramming also faces multiple challenges. For example, the virus vector is currently the most popular delivery method, but it is costly, misses the target effect, and poses a carcinogenic risk to the human body. Due to safety concerns, reprogramming methods that do not rely on virus vectors have received growing attention. The advantages of nonviral vectors are apparent and primarily manifested as high safety, low toxicity, low immune response, high vector capacity, good targeting, and easy assembly. However, low transfer efficiency and short duration of gene expression restrict its adoption in genetic engineering.

A biphasic triboelectric stimulation (TES) platform has been established for realizing efficient nonviral direct transformation of primary mouse embryonic fibroblasts (PMEFs) into neuron cells.²³¹ The cell culture medium was directly connected to a TENG (Figure 19A), and the electrical signals generated by the TENG stimulated the fibroblasts to accelerate their conversion into functional neuron cells.

The microstructures of the nanogenerator are briefly introduced (Figure 19B). A micro-column structured PDMS layer is adhered to a Kapton film. A Cu layer adhered under the Kapton film is used as the friction material and the bottom electrode. And an Al film simultaneously functions as the friction material and the top electrode. A triboelectric stimulator can be used as a self-powered biphasic electric stimulator to promote direct cell transformation because the contact and separation processes of the two friction materials generate currents

in opposite directions. To test the reliability of the TES, its cyclic stability and variable contact frequency was tested. There was no apparent change in the output of triboelectric stimulator for 1800 s of cyclic contact, and the triboelectric stimulator maintained a stable voltage output at different contact frequencies (0.5–3 Hz).

Experiments show that the triboelectric stimulator has good output stability. Four groups of experiments on PMEF producing induced neuronal (iN) cells were conducted using the controlling variable method.

The conversion efficiency on the 9th and 12th–14th days are presented in Figure 19C, with NT < TES < BAM < BAM/TES groups. After the 14th day of the experiment with the four experimental groups, the cells in the BAM/TES group showed apparent neuronal morphology (Figure 19D), indicating that exposing the cells to a triboelectric stimulator environment can accelerate cell transformation. To verify the feasibility of direct cell transformation *in vivo*, a cell transformation experiment was performed on mice. Mouse dermal fibroblasts were directly transformed into induced neuronal cells *in vivo*.

The experimental process is illustrated in Figure 19E. On the 14th day, an anti-Tuj1 antibody was employed for the immunostaining of skin tissue sections of mice in the NT, EGFP, BAM, and BAM/TES groups. A triboelectric stimulator does promote the nonviral production of induced neuronal cells, proving their good adaptability to an *in vivo* environment (Figure 19F). This study demonstrates the feasibility of combining nonviral direct transformation and TES, and has significant medical value.

A pacemaker is an electronic therapeutic instrument implanted in the body. Because drug therapy for the treatment of arrhythmia diseases such as bradycardia is often accompanied by significant side effects, it cannot be used for a protracted period. Furthermore, these diseases are incurable. Thus, pacemaker implantation has become a radical yet effective treatment for bradycardia, that is, an arrhythmia typified by slow heart rate. With developments in microelectronics since the invention of the pulse generator, cardiac pacemakers have been continuously improved, resulting in increased complexity in their electronic components and considerable reduction in size.

However, the battery capacity is usually relative to the size of the pacemaker. Although small-sized pacemakers bring convenience to surgery, their battery capacity is small and the lifespan of the pacemaker is commensurately short.^{252,253} Clinically, most cardiac pacemakers are replaced because the pacemaker's battery is depleted and cannot provide sufficient drive current to maintain normal operation of the pulse generator. Thus, using small pacemakers increases the number of replacements and the probability of infection. An independent study shows that the probability of infection during pacemaker

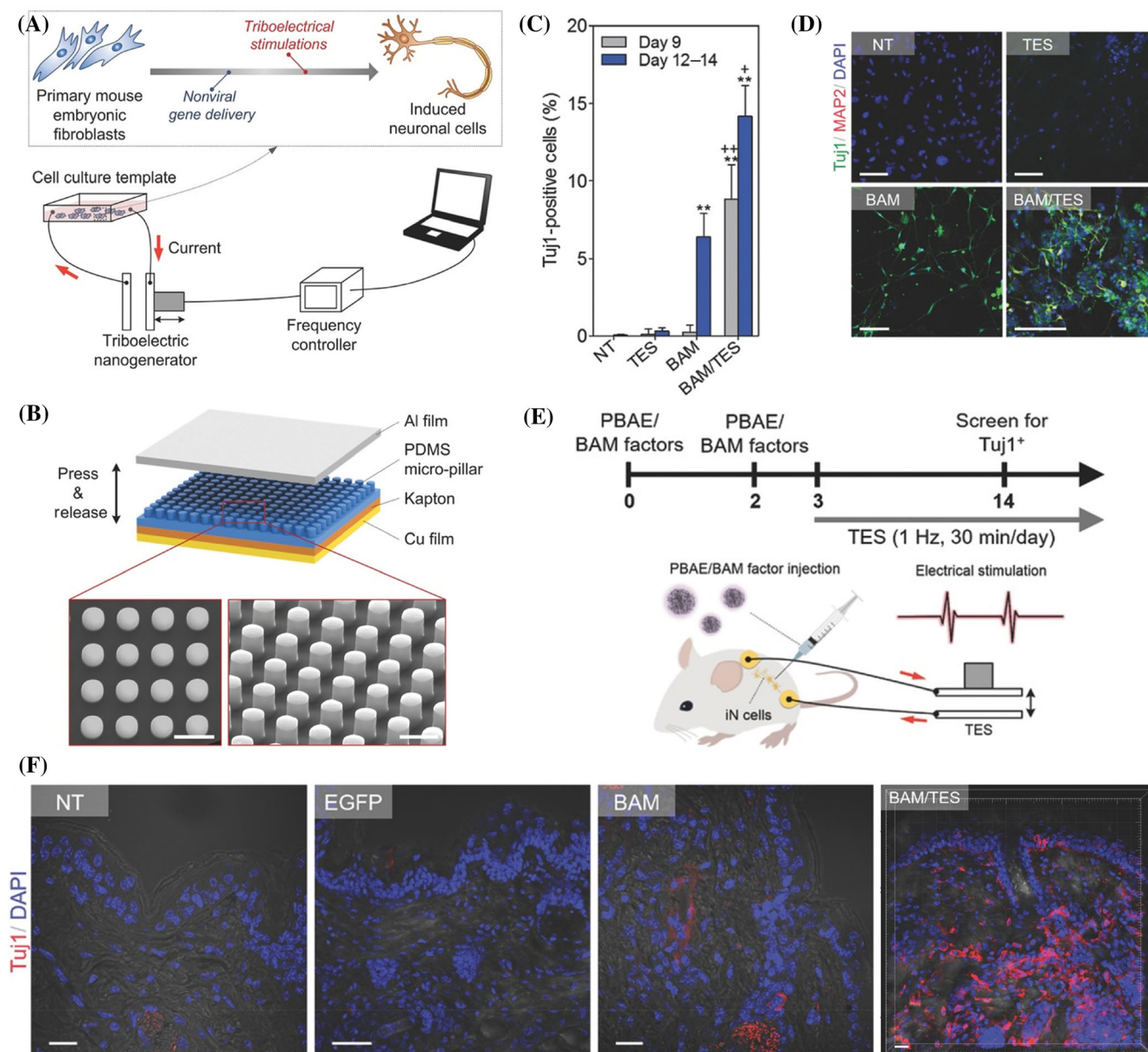


FIGURE 19 A biphasic triboelectric stimulator platform can be used to directly and efficiently transform primary mouse embryonic fibroblasts into induced neuronal cells. PBAE denotes poly(β -amino ester). (A) Schematic diagram of triboelectric stimulator device for realizing direct nonviral transformation. (B) Structural diagram of the designed TENG. (C) Conversion efficiency of primary mouse embryonic fibroblasts on Day 9 and Days 12–14. (D) Fluorescence staining of cells in the four experimental groups after the 14th day of the experiment. (E) Schematic diagram of the experimental process of the mouse cell transformation experiment. (F) Immunostaining of skin tissue sections of mice in the NT, EGFP, BAM, and BAM/TES groups on Day 14 using anti-Tuji1 antibody. NT denotes not transfected. EGFP denotes enhanced green fluorescent protein. BAM is the abbreviation for three neuronal transcription factors Brn2, Ascl1, and Myt11. TES denotes triboelectric stimulation. BAM/TES group stands for the transfection of primary mouse embryonic fibroblasts with BAM transcription factors-expressing plasmids and their subsequent maintenance in neuronal induction medium and exposure to TES. Reproduced with permission.²³¹ Copyright 2016, Wiley-VCH Verlag GmbH

replacement is three times higher than during initial implantation. A long battery life can significantly reduce the number of pacemaker replacements, which means fewer surgeries and reduced incidence of infection.^{254,255} Therefore, pacemaker battery life has become a key problem requiring urgent solution.

A self-powered cardiac pacemaker was realized via a flexible single-crystal $\text{Pb}(\text{Mg}_{1/3}\text{Nb}_{2/3})\text{O}_3\text{-xPbTiO}_3$ (PMN-PT) piezoelectric nanogenerator.²³² The flexible PMN-PT PENG (Figure 20A) is designed to continuously generate electric energy via periodic bending/reduction. It can be used directly as a cardiac pacemaker by attaching copper

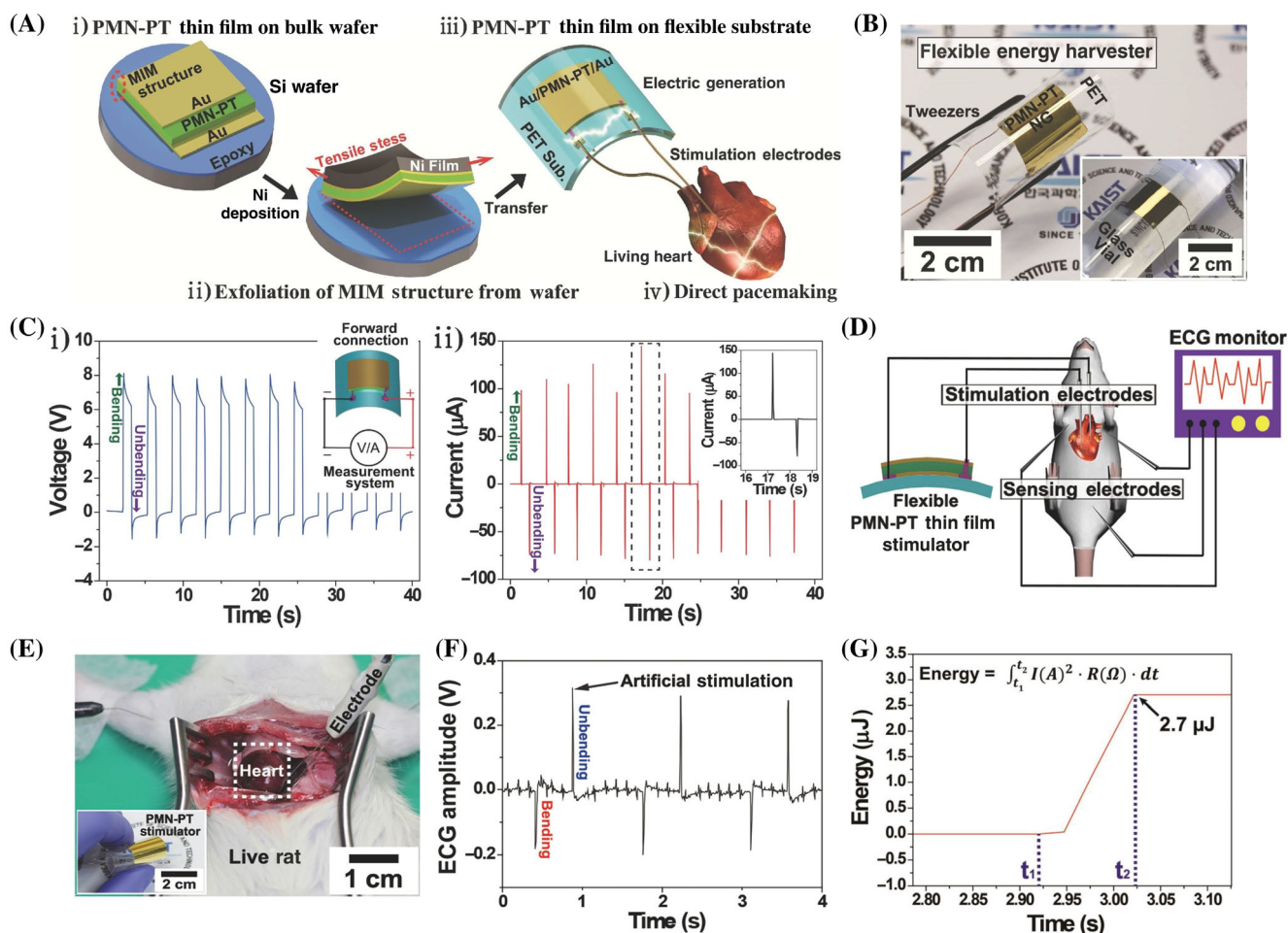


FIGURE 20 Self-powered cardiac pacemaker. (A) Schematic diagram of the manufacturing process and biomedical application of the flexible PMN-PT piezoelectric energy harvester. (B) Photographs of the designed flexible PMN-PT PENG, showing its excellent bendability. (C) Output voltage and current of the PMN-PT PENG. (D) Experimental schematic diagram of cardiac stimulation in rats. (E) Photographs from experiment on cardiac stimulation and heartbeat perception via rat thoracic cavity. (F) ECG of rats in the experiment. (G) Energy generated by the designed flexible PMN-PT PENG (MIM: metal–insulator–metal). Reproduced with permission.²³² Copyright 2014, WILEY-VCH Verlag GmbH

wires to a metal pad with silver conductive paste and then connecting them to a stimulation electrode.

A photograph of the designed flexible PMN-PT PENG is demonstrated (Figure 20B). The bending deformation of the device generates a voltage potential, and electrons are transferred through an external circuit to balance the electric field generated by the dipoles and accumulating at the top electrode; when the deformation recovers, the electrons flow back; and electrons are transferred through an external circuit to balance the electric field generated by dipoles.

A PMN-PT PENG with dimensions of $1.7 \text{ cm} \times 1.7 \text{ cm}$ was tested to evaluate the output performance. The results, presented in Figure 20C, indicate that the designed PMN-PT PENG has excellent output performance, with maximum output current and voltage reaching $145 \mu\text{A}$ and 8.2 V , respectively, which fully

meets the $100 \mu\text{A}$ and 3 V input requirements for cardiac pacemakers. Furthermore, finger tapping generates a current signal of $223 \mu\text{A}$, which is more than 36 times the maximum current of a ZnO nanowire nanogenerator ($6 \mu\text{A}$) and 8500 times the maximum current of a BaTiO₃ thin film nanogenerator (26 nA). An anti-fatigue test was also performed on the device.

The output of the PMN-PT PENG did not show any apparent decline after 30 000 cycles of a durability experiment, which indicates its durability. To verify the feasibility of the designed flexible PMN-PT PENG as a cardiac pacemaker, rats were selected as test subjects for a cardiac stimulation experiment. The flexible PMN-PT PENG was directly connected to a stimulation electrode to provide electrical stimulation to the heart of anesthetized rats (Figure 20D), and the ECG was transmitted via a sensing terminal. Figure 20E presents a photograph of

the animal experiment in which the thoracic cavity of a rat was opened for cardiac stimulation and heartbeat perception. The corresponding peak value generated by the flexible PMN-PT PENG is clearly observable on the rat's natural heartbeat ECG (Figure 20F). In addition, the designed flexible PMN-PT PENG can generate approximately 2.7 μJ of energy in one bending motion (Figure 20G), which is considerably higher than the threshold energy for electrically stimulating a living heart (1.1 μJ). The above shows that the flexible PMN-PT PENG has significant development prospects in cardiac function normalization.

The treatment of neurological diseases such as dyskinesia, epilepsy, and Parkinson's disease has typically relied on drug therapy for a long time. However, therapeutic drugs often affect various organs and tissues of human body, causing various side effects. With the development of microelectronic technology, implanted medical devices have received extensive attention as a solution. Clinically, implanted medical devices have the advantages of less damage to the human body, less complications, and reversibility. For example, deep brain electrical stimulation shows considerable potential with stimulator technology,²⁵⁶ which implants electrodes in specific brain regions and then injects electrical signals into the nervous system.

Compared with drug therapy, it is safer to inject electrical signals into the nervous system. The principle behind this method is that the potential of the designated nerve region can be artificially controlled, which means that it will not affect other parts of the body and will not produce side effects. Furthermore, the electrical signal injection method can realize an almost transient response, quickly activate nerve tissue, and is more efficient than drug therapy. This technique has been extensively used to treat tremor, Parkinson's disease, dystonia, Tourette syndrome, pain, and depression. However, due to its high operating frequency and high-power consumption, the service life of the device is short. For many patients, once the equipment is turned off for a few minutes or seconds or the battery is depleted (the battery life is 3–5 years), the treated condition immediately returns. However, frequent replacement of the equipment increases the risk of complications such as infection and hemorrhage, along with a heavy economic burden on the patient. Therefore, it is particularly important to design an implantable electrical stimulator that can be used for a long period.

A metal–insulator–metal PENG²²⁸ based on flexible $\text{Pb}(\text{In}_{1/2}\text{Nb}_{1/2})\text{O}_3\text{-Pb}(\text{Mg}_{1/3}\text{Nb}_{2/3})\text{O}_3\text{-PbTiO}_3$ (PIMNT) could provide a deep brain stimulation (DBS) in a self-powered fashion. The designed PIMNT PENG is fabricated by adhering a 10 μm thick PIMNT film, with Au electrodes on both sides, to a 125 μm thick substrate by using polyurethane (PU) adhesive. A photograph (Figure 21A)

and structural diagram (Figure 21B) of the device are presented.

The output performance of the such a PENG was tested under mechanical bending and straightening at a frequency of 0.32 Hz. A maximum open-circuit voltage of 11 V and maximum short-circuit current of 283 μA were obtained. A rectified PIMNT PENG can charge capacitors of different capacities (0–2 V) in a short time (tens of seconds to 200 s) (Figure 21C), or directly light up 120 parallel LED lamps (Figure 21D). To verify the durability of the device, 15 000 cycles of a mechanical test were performed.

Eventually, the PIMNT PENG was directly connected to a DBS stimulation electrode for activating the primary motor cortex (M1) in an experiment on the brain of a living mouse. The experimental scheme and photographs are presented (Figure 21E,F). The paw movement distance of mice receiving six instances of electroencephalogram (EEG) stimulation is shown (Figure 21G). The experiment proves that the M1 cortex of mice can be stimulated by a self-powered PIMNT PENG inducing DBS to cause forelimb muscle contraction. This study is an important reference for further development of future in vivo medical technology that realizes self-powered DBS devices driven by conversion of mechanical energy generated by bodily movement.

Osteocytes function as mechanical receptors in bone tissue and also as biochemical signal response effectors that convert mechanical stimulation into signals, regulating osteoblast and osteoclast activity and consequently bone remodeling under mechanical stress. Bone cells may have a regulatory or even dominant role in bone remodeling and orthodontic treatment, with the maintenance of bone function in adults depending primarily on bone remodeling. Bone is a dynamic active tissue that maintains its mineralization balance and structural integrity through continuous remodeling.²⁵⁷ In the bone remodeling process, osteoblasts and osteoclasts play a key role in regulating bone growth or absorption by feeling mechanical stimulation. Increased osteoblast function or decreased osteoclast function leads to increase in bone mass.

The reverse leads to bone mass reduction and osteoporosis-like changes, which are the main causes of a high incidence of fracture and bone pain in the middle-aged and elderly. In the field of medicine, the photobiological regulation effect of low-level laser therapy occupies an important position in many disciplines.^{258,259} The laser therapy has a positive effect on bone reconstruction and formation, which has been supported and confirmed by many in vitro and in vivo studies. Several studies have reported that low-energy lasers can activate osteoblasts and promote bone tissue healing and reconstruction. In the field of orthodontics, low-intensity lasers have been clinically applied to reduce

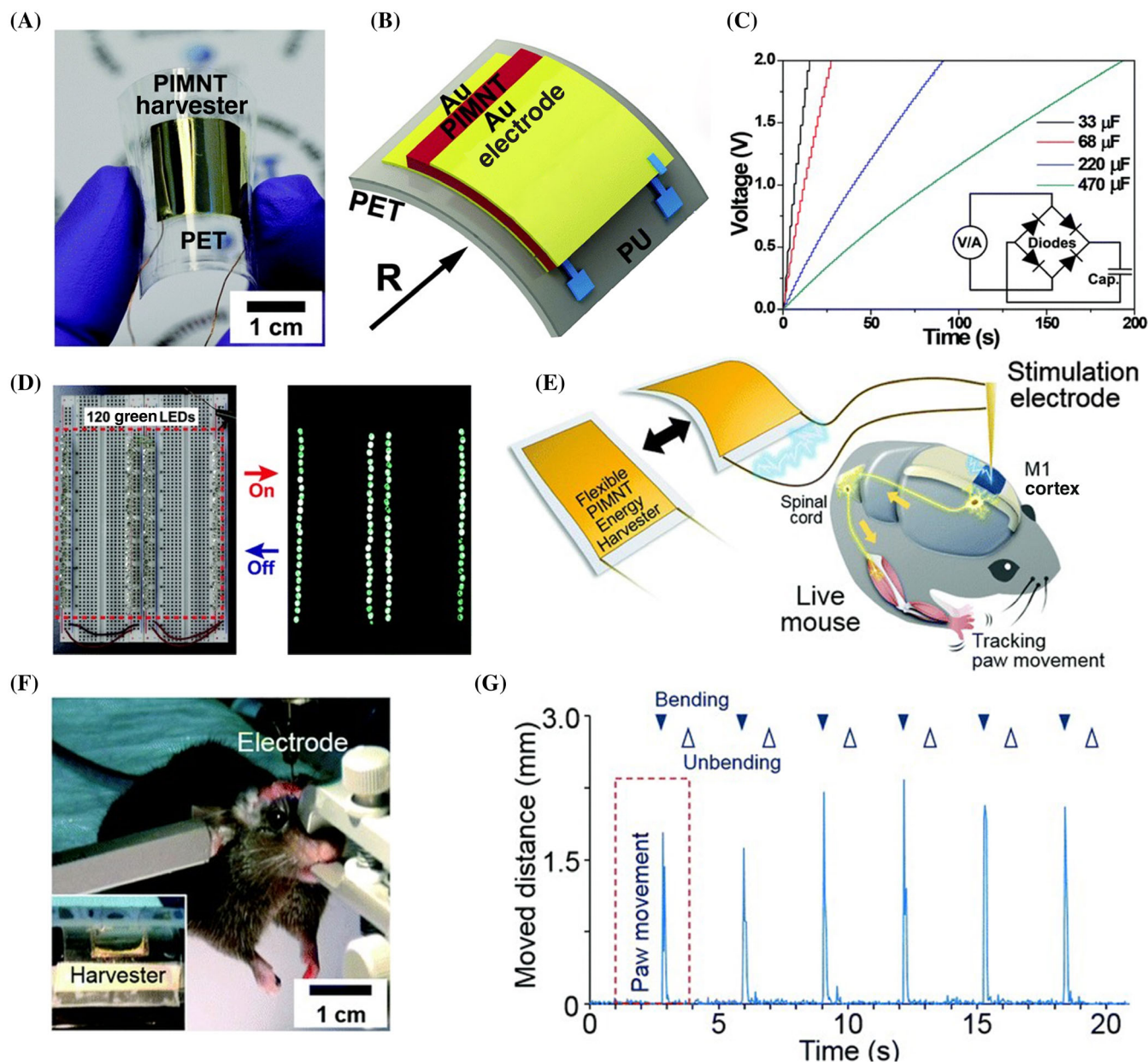


FIGURE 21 Flexible PENG device for providing self-powered deep brain stimulation. (A) Photograph and (B) structural diagram of the designed PIMNT PENG. The rectified PIMNT PENG (C) charging capacitors with different capacities, and (D) directly lighting up 120 parallel LED lamps. (E) Experimental schematic diagram and (F) photograph of the PIMNT PENG used for activating the brain of a living mouse in an M1 experiment. (G) Time graph of paw movement distance for mice receiving six EEG stimuli. Reproduced with permission.²²⁸ Copyright 2015, The Royal Society of Chemistry

pain in orthodontic treatment. Such a laser therapy can accelerate tooth movement.²⁶⁰ To promote the application of this technology, an attachable or implantable laser treatment system is required. However, conventional batteries are limited in use due to their size and lifespan.

An implantable self-powered low-level laser cure (SPLC) system for osteogenesis²³³ could significantly accelerate the proliferation and differentiation of mouse embryonic osteoblasts. The designed SPLC system consists of an arched flexible TENG and an infrared laser

excitation unit. The arched flexible TENG is made of PDMS and indium tin oxide (ITO) films, with a pyramid surface structure, as friction materials (Figure 22A). The output performances (Figure 22B,C) demonstrate maximum short-circuit current and maximum open-circuit voltage of about 3 μ A and 115 V, respectively. Murine calvarial preosteoblasts (MC3T3-E1) were selected for grouping experiments. The experimental grouping was as follows: a reference group without laser irradiation, a laser irradiation group with an irradiation frequency of

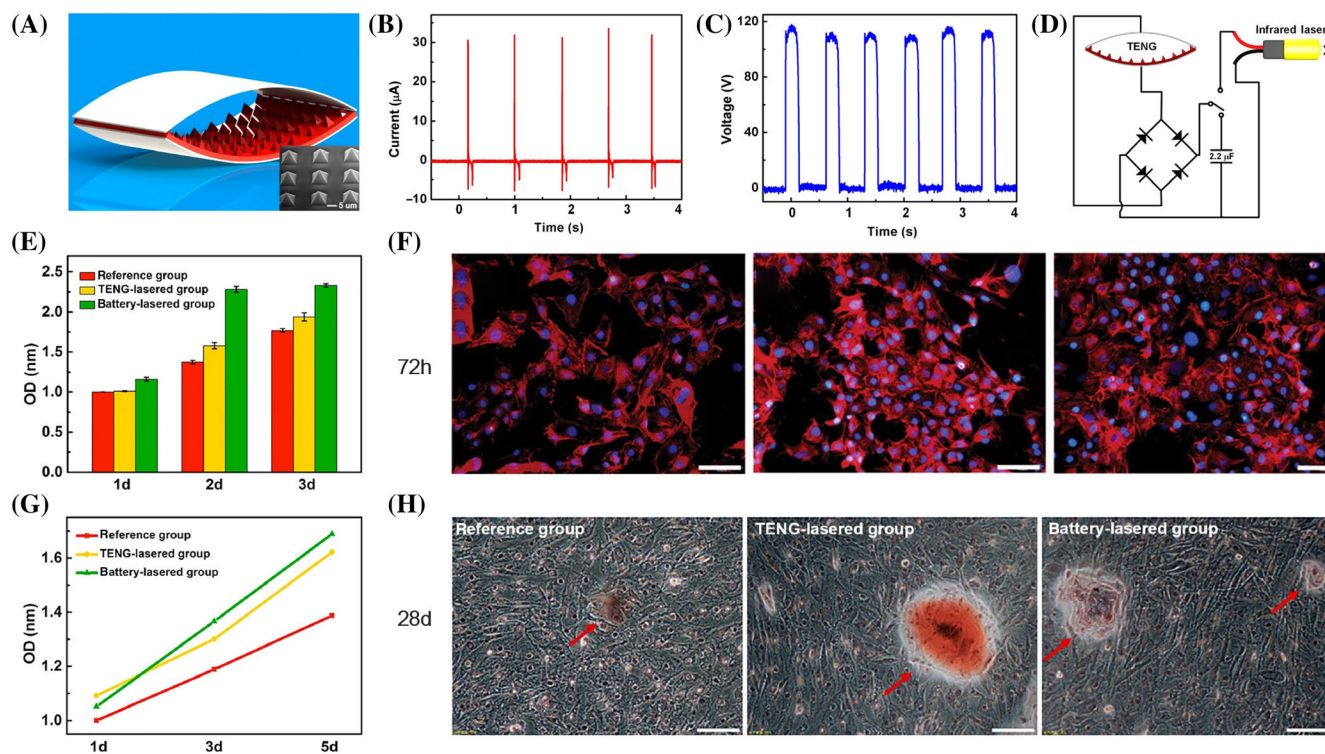


FIGURE 22 SPLC system for osteogenesis developed based on power generation via a TENG (OD: optical density). (A) Schematic diagram of the designed arch-shaped flexible TENG. (B) Time graph of the short-circuit current and (C) open-circuit voltage of the designed arched flexible TENG. (D) Schematic diagram of the SPLC system. (E) Cell proliferation for the first 3 days after the experiment. (F) Cell number and morphology after 3 days. (G) ALP level and (H) mineral deposition for the three experimental groups. Reproduced with permission.²³³ Copyright 2015, American Chemical Society

100 pulses/day using a TENG-driven laser. Here, the laser is powered by a capacitor charged by a TENG (Figure 22D). And a laser irradiation group has been set with an irradiation time of 1 min/day using a battery-powered laser. The cell proliferation for the first 3 days immediately after the experiment are presented in Figure 22E, and the cell number and morphology after the 3 days are presented in Figure 22F. From these two figures, the cell degrees of the TENG-driven laser irradiation and battery-powered laser irradiation groups are higher than that of the reference group, indicating that infrared laser irradiation can indeed accelerate cell proliferation. The alkaline phosphatase (ALP) level and mineral deposition have a certain degree of significance in measuring the growth degree of MC3T3-E1 cells. Figure 22G,H present the ALP level and mineral deposition, for the three groups of experiments. There is more cell growth in the laser irradiation group than in the reference group for both experiments. The above experiments show that the designed SPLC system has a positive effect on proliferation, differentiation, and bone formation of osteoblasts, which indicates that the system can be used in clinical applications for bone remodeling and orthodontic treatment.

5 | OTHER APPLICATIONS

5.1 | Disinfection and sterilization

From its origin and through different periods of societal development, human beings have subjectively and actively used productive labor to change their environments and to modify the natural environment to meet the needs of human survival and societal development. However, human activities have also caused a depletion of natural resources and pollution and destruction of the ecological environment due to a continuous transformation of the natural environment. With the rapid development of social economy and technology, this damage becomes increasingly severe. Thus, the increasing convenience in daily living brings increasing environmental problems, resulting in specific threats to our living and work environments. In some areas, more than environmental pollution accidents, there are large-scale ecological damage and environmental crises.

Water is the most precious natural resource, essential for human survival and socioeconomic development. Freshwater resources are closely connected to the survival

of human beings and other organisms.^{261–263} However, the availability of freshwater in the world is unevenly distributed. By 2025, 60% of the world's population may face a water shortage crisis. The rapid deterioration of the water environment, together with the multiplication of toxic algae and harmful bacteria in water bodies, results in a more acute shortage of water resources. Concurrently, the continuous deterioration of the water environment has also negatively impacted human society, causing agricultural production to decrease or even cease, and forcing factories to stop production, causing considerable economic losses. These factors hinder the sustainable development of the society and threatens the survival of mankind. Therefore, finding a solution to the water pollution problem has become one of the major environmental problems presently in need of an urgent solution, thus receiving widespread attention from the international community.

5.1.1 | Self-powered electrochemical water treatment system

A self-powered electrochemical water treatment system was fabricated for wastewater sterilization and algae removal.²⁶⁴ The system consists of a seawater electrolysis device and an arched TENG (Figure 23A) that harvests energy from water waves to power the device. A plurality of TENG units connected in parallel are placed in water together (Figure 23B,C).

With the alternating motion of water waves, an ITO-PET film top plate and PET-ITO-PTFE film bottom plate in the TENG are continuously contacted and separated to generate an alternating current between the TENG's electrodes. The designed electrochemical water treatment system (Figure 23D,F) consists of a TENG and its rectifying device as power supply, a 10 ml reaction vessel, and two electrode plates made from mixed metal oxide (MMO), Ti, and reduced graphene oxide (RGO). RGO nanosheet can inhibit the proliferation of microorganisms on its surface. A schematic diagram of an RGO-assisted electroporation MMO-coated Ti plate sterilization and algae removal mechanism is presented in Figure 23E.

Output tests were performed at a frequency of 2 Hz on 50 parallel TENG devices with dimensions of 15 cm × 30 cm. The parallel TENG devices delivered a short-circuit current with an average amplitude of 4.8 mA and an open-circuit voltage with a peak value of 210 V. First, the antibacterial and methyl methacrylate (MMA) removal effect of different electrodes was tested. To meet the requirements for disinfection and algae removal, the output of the TENG device was voltage-

reduced during the experiment (Figure 23G,H). The MMO-Ti-RGO electrode delivered the best performance in both the antibacterial and algal removal experiments. The system realizes high-efficiency sterilization (removal rates for *Escherichia coli*, *Streptococcus faecalis*, and *Vibrio alginolyticus* are over 99.9999%) and algae removal performance (survival rates for three mixed algae: *Phaeodactylum tricornutum*, *Skeletonema costatum*, and *Prorocentrum donghaiense* was reduced to zero) through electroporation and the synergistic effect of free chlorine and RGO during electrolysis.

The accumulation of bacteria or algae on wet surfaces will bring various problems to shipping, buildings along water and underwater facilities. An integrated triboelectric wave harvester (I-TEWH) can realize the antifouling of wet insulation surface through solid-liquid contact friction electrification (Figure 24A).²⁶⁵ Most microorganisms are charged bodies, and I-TEWH converts water wave energy into periodically changing electric energy, which will generate alternating electric fields near the protected surface. According to the principle of electrostatic induction, alternating electric field can disturb the surface charge distribution of microorganisms near the protected surface, which can disturb the inherent charge distribution of microorganisms, thus achieving the effect of inhibiting the adhesion of microorganisms. The anti-adhesion efficiency of this method to diatoms (bacillariophyceze), positive-gram bacteria (*Staphylococcus aureus*), and negative-gram bacteria (*E. coli*) is as high as 96.0%, 99.1%, and 99.3%, respectively.

For some cases where only a small part of water needs to be treated (rural areas or sudden disasters), the requirements of power and cost control are very strict. In this case, disinfection of POU with water is an economical and efficient treatment method. A TriboPump based on TENG can effectively realize water disinfection (Figure 24E).²⁶⁶

This system includes three parts: disinfection device (coaxial-electrode copper ionization cell [CECIC]) (Figure 24G), power source (disk triboelectric nanogenerator [D-TENG]) (Figure 24F), and water pump (Figure 24H). TriboPump combines TENG and CECIC together, which can make TENG generate electric field by manual operation. The existence of electric field can release Cu ions on the center click to inactivate bacteria, and at the same time enhance the permeability of bacterial cell membrane, thus increasing the consumption of copper entering bacterial cells. Experiments show that the inactivation rate of TriboPump on bacteria is as high as 6 log, while the Cu concentration in the discharged water is only 180–340 $\mu\text{g L}^{-1}$, which is far lower than the maximum pollutant level target of copper in drinking water set by US Environmental Protection Agency (1.3 mg L^{-1}).

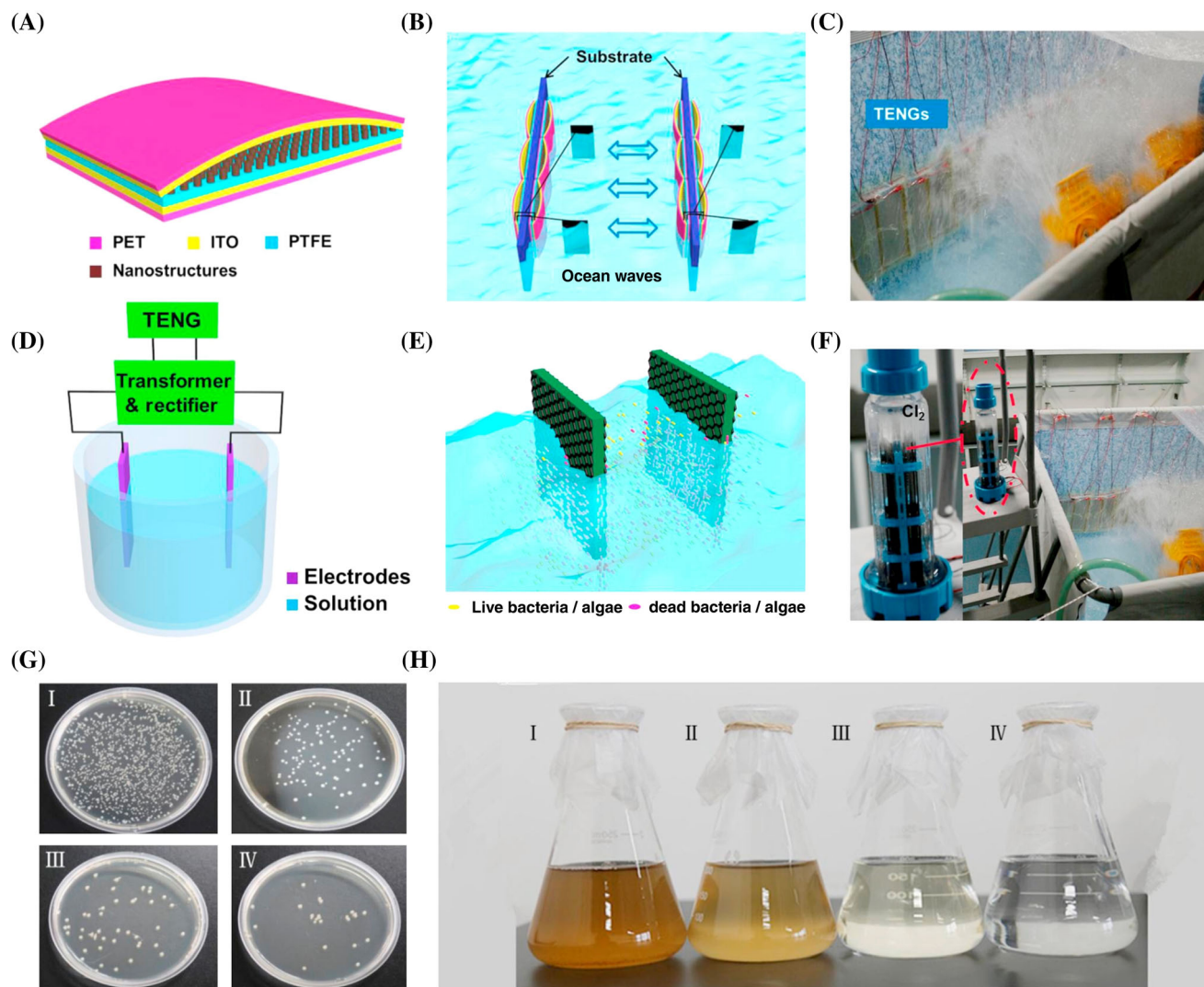


FIGURE 23 Self-powered electrochemical water treatment system. (A) Schematic diagram of the designed arch TENG. (B) Plurality of TENG units placed in parallel together in water. (C) Photograph of TENGs collecting water wave energy. (D) Schematic diagram and (F) photos of the designed electrochemical water treatment system. (E) Schematic diagram of RGO-assisted electroporation MMO-coated Ti plate sterilization and algae removal mechanism. (G) Antibacterial and (H) MMA removal effect of different electrodes. Reproduced with permission.²⁶⁴ Copyright 2015, Elsevier Ltd

5.1.2 | Sustainable sterilization

A self-powered sterilization system with both instant and sustainable antibacterial capability²⁶⁷ performs electroporation when an electric field is applied and continuously sterilizes after the electric field is removed. The system (Figure 25A) is composed primarily of a TENG driven by water waves and two nano-brush electrodes integrated via silver NPs and ZnO nanowires. Ag/ZnO electrodes are fixed in two filter supports to sterilize the bacterial solution extracted from the pump. The TENG, driven by wave motion, supplies an electric field to the electrodes. The designed spherical TENG consists of a rubber ball serving as a friction layer and two arc-shaped Al electrodes serving as both friction and electrode layers.

The operating principle of the spherical TENG is illustrated in Figure 25B. When the TENG moves under the action of water waves, the small balls within it roll and continuously make contact with and separate from the electrodes on both sides, generating an alternating output current. Using *E. coli* and *S. aureus* as samples in different control group experiments, the sterilization efficiency of the designed self-powered disinfection system was tested. The experimental results are presented in Figure 25C,D. Here, the sterilization effect of Ag/ZnO nano-brushes driven by the TENG is superior to that of the other three groups of control experiments, with a 100% sterilization rate (SR) for *E. coli* and a 99% SR for *S. aureus*.

A sustained sterilization capability after removal of the electric field is also demonstrated, with a 100% SR for

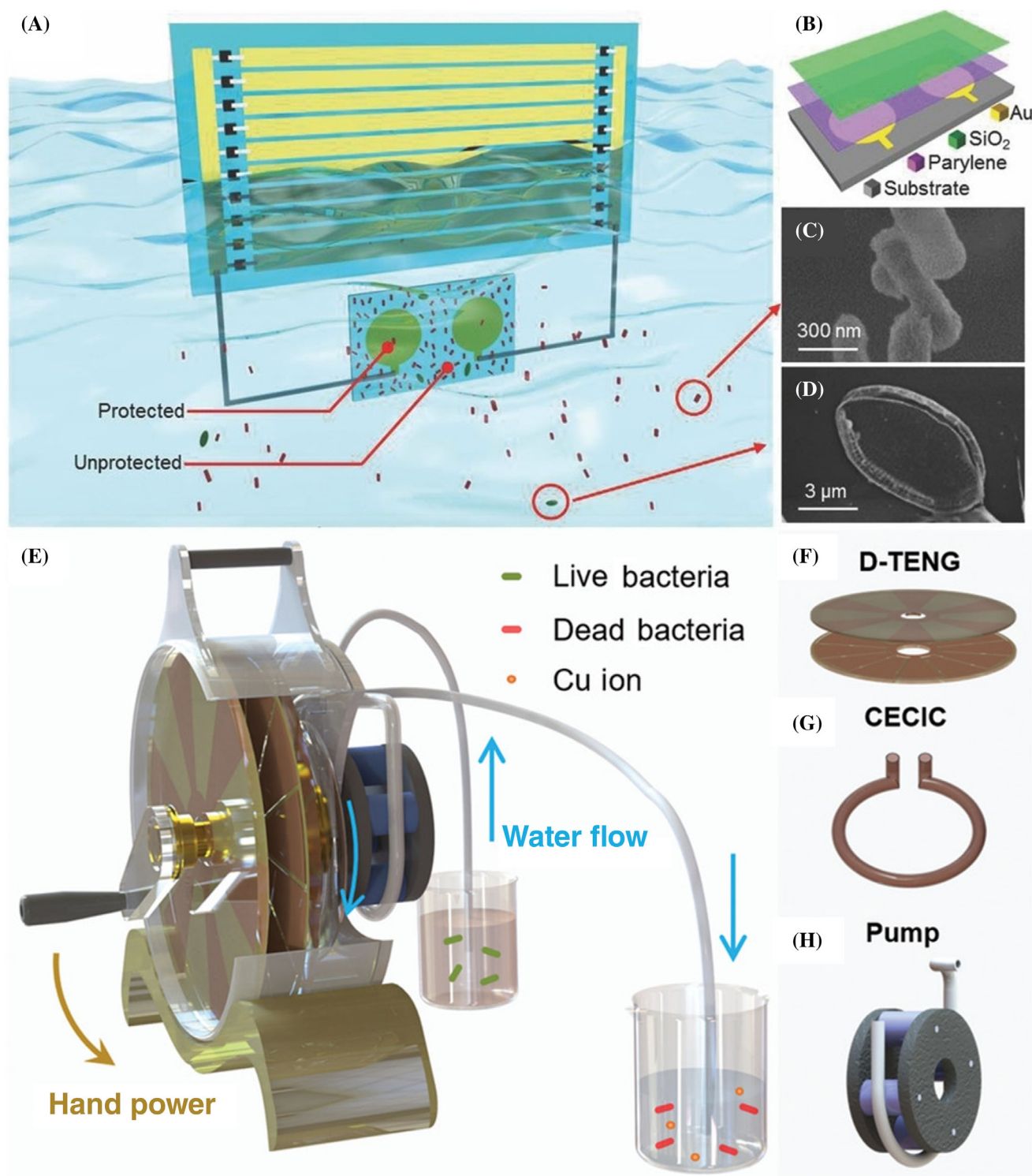


FIGURE 24 (A) Schematic diagram of antipollution device. (B) Structure of underwater components. SEM images of (C) *Escherichia coli* and (D) *Nitzschia* sp.²⁶⁵ Reproduced with permission. Copyright 2019, Wiley-VCH Verlag GmbH. (E) Schematic diagram of TriboPump system. (F) Schematic diagram of D-TENG section. (G) Schematic diagram of CECIC part. (H) Schematic diagram of water pump.²⁶⁶ Reproduced with permission. Copyright 2016, Wiley-VCH Verlag GmbH

E. coli and an $\approx 95\%$ SR for *S. aureus* 20 min after removal of the electric field. Furthermore, for natural river water, also used as an experimental object for the sterilization

capability test, the designed system still exhibits a strong sterilization effect (Figure 25E) as there are almost no microorganisms in the river water sterilized, and a

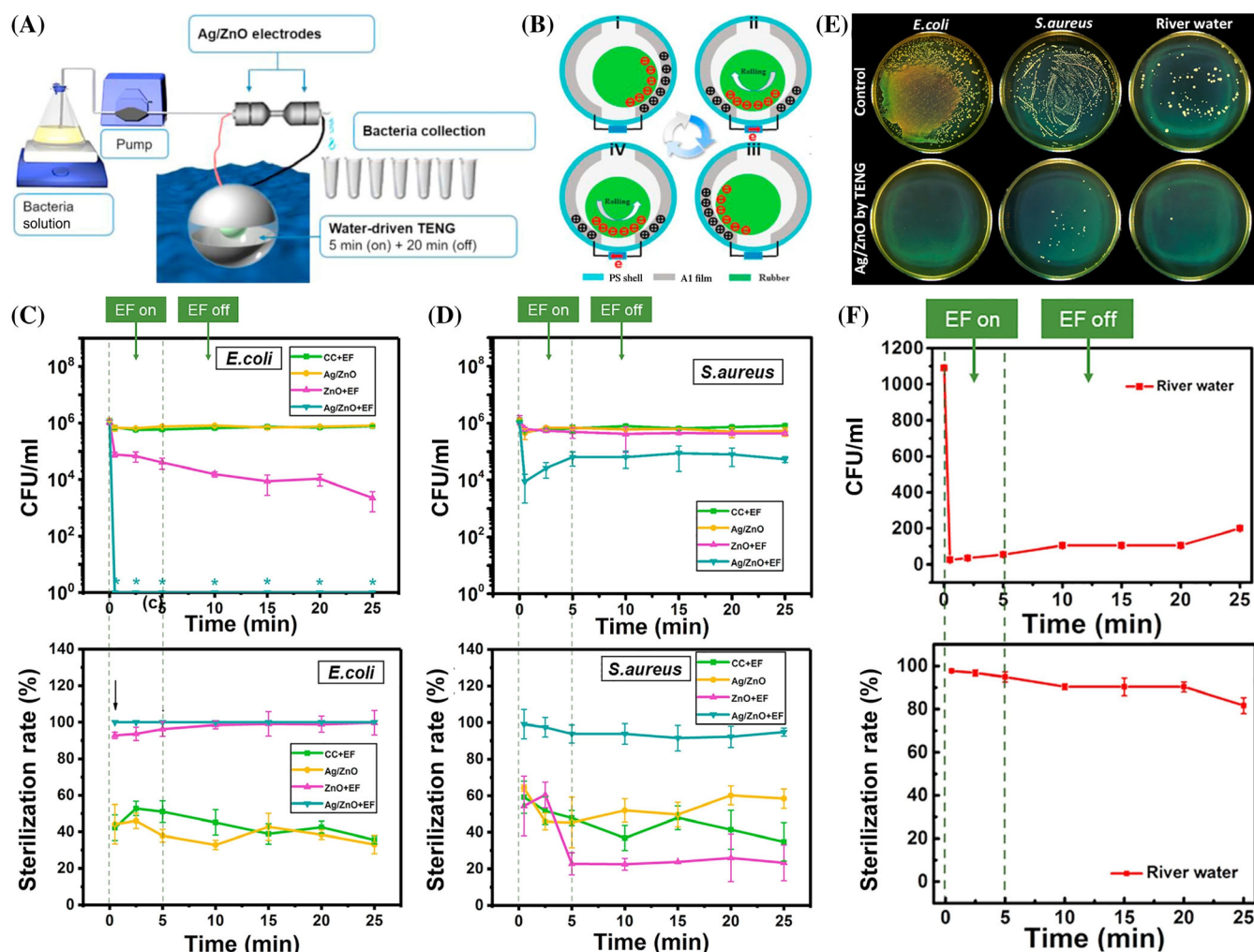


FIGURE 25 Self-powered sterilization system with both instant and sustainable antibacterial ability. (A) Schematic diagram of the designed experimental device for the self-powered disinfection system. (B) Schematic diagram of the operating principle of the spherical TENG. (C) *Escherichia coli* and (D) *Staphylococcus aureus* as samples to test sterilization efficiency. (E) Natural river water as the experimental object for the sterilization capability test. (F) Colony forming units (CFU) and SR of microorganisms in river water. Reproduced with permission.²⁶⁷ Copyright 2017, Elsevier Ltd

sustained sterilization capability is evident, with an SR exceeding 80% 20 min after the removal of the electric field (Figure 25F).

5.2 | Degradable medical devices

Because the substrate materials and electronic components of traditional implanted medical devices are not degradable, they often need to be removed via surgery when the designated diagnosis and treatment tasks are completed. This supplementary surgery causes secondary trauma to the patient and may cause complications such as wound infection and suppuration, and increased medical costs. Thus, the development of biodegradable electronic devices has attracted considerable attention.^{268,269} The biodegradable electronic devices can be completely

or partially degraded in physiological environments or in water. Degradable electronic devices can be absorbed by the human body, and when applied in the field of implantable medical diagnosis and treatment, avoid the side effects of secondary surgery and long-term implantation. Biodegradable electronic devices require degradable energy supply components to maintain normal operation. Although these devices have shown considerable potential, research on their energy supply remains very limited, which also limits its application in vivo. Therefore, the development of a safe, efficient, and long-term stable power supply for implanted degradable electronic medical devices is currently a challenging issue in scientific research.

A biodegradable TENG²⁷⁰ (BD-TENG) can be employed as a long-term implantable power supply. The designed biodegradable TENG (Figure 26A) is composed

of degradable polymers: poly(L-lactide-co-glycolide) (PLGA) and poly(caprolactone) (PCL) as friction layers, an absorbable metal (Mg) as the electrode layer, and a degradable polymer as the encapsulation layer and degradable polymer gasket.

The open-circuit voltage (Figure 26B) and short-circuit current (Figure 26C) of the BD-TENG are 40 V and 1 μ A, respectively. Figure 26D presents an in vitro

degradability experiment on the designed BD-TENG device, showing that after 90 days, the device almost completely disappeared, which indicates its good in vitro degradability characteristics. In addition, different beclomethasone dipropionate (BDP) encapsulation layers have different degradation times. Based on this characteristic, the BD-TENG can be designed for implantable medical devices with different lifetimes. The designed

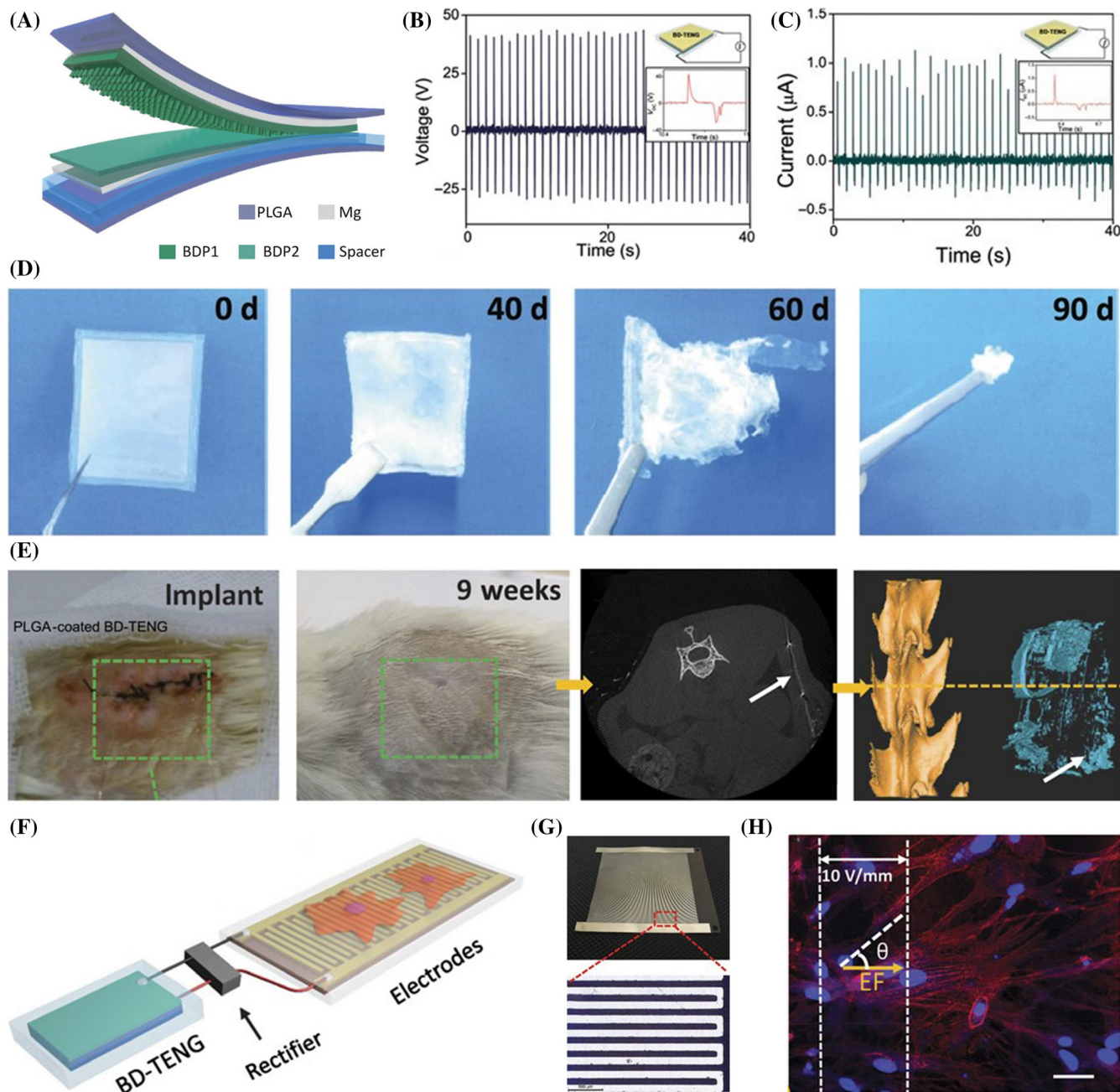


FIGURE 26 BD-TENG as a lifetime designed implantable power source. (A) Structural diagram of the designed BD-TENG. (B) Time graph of the BD-TENG's open-circuit voltage and (C) short-circuit current. (D) In vitro degradability test on the BD-TENG device. (E) Experiment implanting the BD-TENG in a rat. (F) Schematic diagram of the self-powered nerve cell stimulation system. (G) Patterned interdigital electrodes covered with PDMS. (H) Orientation and distribution of nerve cells under guidance of an electric field.²⁷⁰ Reproduced with permission. Copyright 2016, American Association for the Advancement of Science

BD-TENG was implanted in a rat and its wounds were healed after 9 weeks (Figure 26E).

Furthermore, a micro-computed tomography (micro-CT) image of the BD-TENG showed that its structure was almost completely destroyed (Figure 26E), demonstrating good biocompatibility and degradability *in vivo*. In addition, the designed BD-TENG also shows characteristics that can be applied to regulation of the direction of nerve cell growth. By combining the BD-TENG with a polylysine modified stimulation device, that is, a patterned interdigital electrode covered with PDMS (Figure 26G), it was seeded with primary neuron cells (Figure 26F). After being cultured for 5 days under electrical stimulation (1 Hz, 10 V mm^{-1}) for 30 min/day, most of the neurons exhibited a good orientation parallel to the electric field (Figure 26H).

Poly-L-lactide (PLLA) polymer, as a biodegradable polymer, also exhibits certain piezoelectric properties. A biodegradable and biocompatible piezoelectric force sensor is composed of PLLA, molybdenum electrode and polylactic acid (PLA) encapsulation layer (Figure 27A,B), which can effectively detect different breathing patterns of mice (Figure 27C). In addition, after accelerated degradation at 74°C for 56 days (Figure 27D), the designed sensor was completely degraded, and only showed a slight immune response after being implanted into the subcutaneous region of mouse back, and no obvious inflammation, multinucleated giant cells and fibrous cysts were observed.

Silk protein is a kind of natural high molecular fibrin extracted from silk, which has good flexibility, tensile strength, air permeability and moisture permeability, as

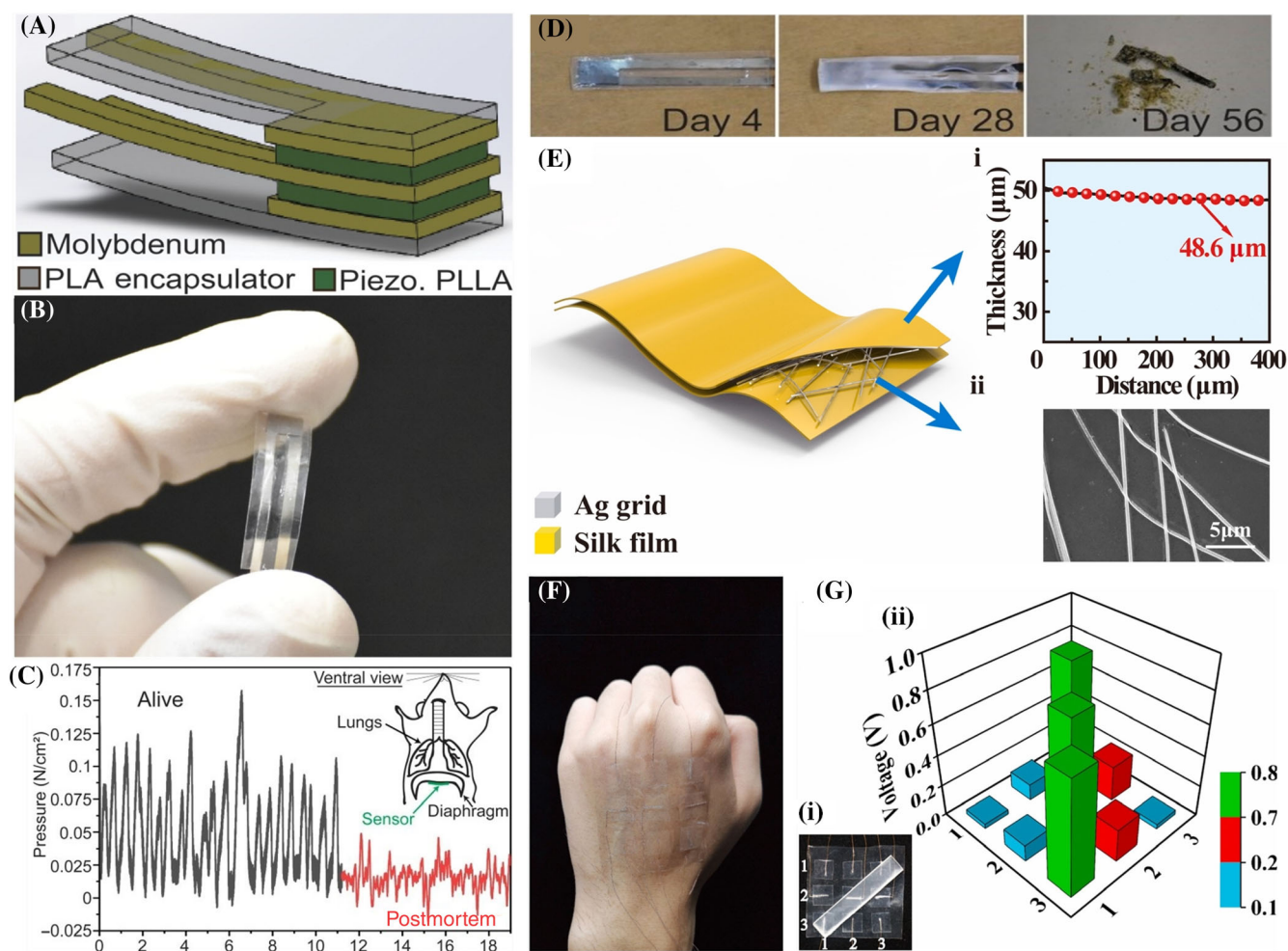


FIGURE 27 Biodegradable pressure sensor. (A) Schematic diagram of PLLA sensor. (B) Photograph of the manufactured PLLA sensor. (C) Different force signals generated by implanted sensors when mice are alive and under anesthesia (black) and mice are euthanized due to excessive anesthesia (red). (D) Degradation of the sensor at 74°C accelerated degradation temperature.²⁷¹ Copyright 2018, Proceedings of the National Academy of Sciences of the United States of America. (E) Structural schematic diagram of TENG based on conductive SFF: (i) Thickness of conductive SFF, (ii) SEM image of Ag NFs. (F) Images of tactile sensors (ii) on the skin. (G) Photograph of the tactile sensor and the corresponding voltage signals.²⁷² Reproduced with permission. Copyright 2020, Elsevier B.V

well as good biocompatibility and degradability, and has strong electron loss ability in triboelectric sequence. A single-electrode mode triboelectric nanogenerator (STENG) with high transparency and biodegradability is composed of a triboelectric electrode composed of silk fibroin film (SFF) and silver nanofiber, and PDMS dielectric material (Figure 27E). The artificial skin array based on TENG can be completely attached to the back of the hand and realize tactile sensing (voltage response to force) (Figure 27F,G). Moreover, the designed STENG has been basically dissolved after being soaked in vinegar for 96 h, and has good degradability. In addition, in the cell culture experiment, MC3T3-E1 cells showed good adhesion, spreading and growth on the surface of SFF, which indicated that SFF had good biocompatibility.

5.3 | Air purification

The exhaust emissions have gradually increased from the factories, power plants, traffic exhaust, and other polluting sources.^{273,274} Many countries have been jointly combating air pollution, as it is a serious environmental problem. The composition of air pollutants is very complex, and the toxic components primarily include carbon monoxide, ozone, nitrogen oxides, and suspended particulate matter (PM). Among pollutants, suspended PM poses the most significant threat to human health and the ecosystem.²⁷⁵ Respirable lung particles (PM_{2.5}) have a size of less than 2.5 μm and their large specific surface area enables the easy absorption of toxic substances. Thus, these particles can directly enter the respiratory tract of humans, causing diseases such as heart disease, asthma, and bronchitis.

At present, there are several methods of particle filtration for air purification: mechanical filtration, the Cottrell process, adsorption, and the use of negative ions. Mechanical filtration generally uses fibers or a porous membrane as the core component, and employs inertial collision, interception, and diffusion purification mechanisms to achieve a good filtration effect on fine particles. However, the wind resistance is large and the filter holes become easily obstructed. The Cottrell process is an important particle filtration method in the field of industrial dust removal,²⁷⁶ and utilizes a high-voltage electric field to ionize dust-containing gas, such that charged particles are adsorbed on a polar plate. Although the wind resistance of the Cottrell process is small, the purification cycle is long, the volume is considerable, and the removal effect on larger particles is poor.

Furthermore, a corona discharge is triggered under high voltages of several thousand volts, which easily releases ozone, generating secondary pollution. In

addition, a large volume of sustained external high-pressure energy consumption also increases the purification cost. Therefore, the development of air PM filtration methods, improving purification efficiency, shortening the purification cycle, and reducing cost have achieved high priority. The prominent feature of the TENG is its high output voltage, with an output range that can reach thousands of volts from several volts, which makes it an ideal choice for air purification. The utilization of the triboelectric effect may create a safe, energy-saving, and yet strong electrostatic field for an electrostatic filtration process for air particles. Table 5 lists the performance summary of various air purification devices.

A 3D-printed biomimetic-villus structure based TENG and a biomimetic-villus dust filter (BV-DF)²⁷⁷ effectively absorbs dust particles of various sizes. The designed BV-TENG (Figure 28A) is a cylindrical body with a villus-shaped structure extending inwards, which is polymerized layer-by-layer by a 3D printer. The acrylonitrile butadiene styrene cylindrical body and its inner surface is filled with PTFE powder that can produce the triboelectric effect, and the outside of each villus is coated with an Ag layer functioning as an electrode.

The designed BV-TENG can make the PTFE powder and the inner surface of the ABS cylinder contact and separate continuously under vibration (Figure 28B) and rolling (Figure 28C) modes, thus generating current. Furthermore, the designed BV-TENG has good stability and its output is almost unchanged after 1000 cycles of operation. The BV-TENG can be used as a dust filter by replacing the inner PTFE powder with PTFE balls and removing the external circuit structure. When the BV-DF moves (slides, rotates, or vibrates), the PTFE balls and ABS surface contact, generating large amounts of frictional charge (Figure 28D). As dust flows through the reticular BV-DF, the PTFE balls and the ABS surface absorb the dust particles with positive and negative charges, respectively, achieving a filtration effect. In addition, the designed BV-DF also has good stability, and its adsorption efficiency shows no evident change after washing, thus being reusable after washing (Figure 28E).

A triboelectric air filter (TAF)²⁷⁸ can efficiently remove fine particulate matter (PM_{2.5}) from air. The air filter is a multilayer structure composed of nylon and PTFE fabrics. Through simple friction (Figure 29A), frictional charges are generated between the two fabrics and therefore build a strong electric field between them. The operating mechanism of the air filter is illustrated (Figure 29B,C).

When the triboelectric air filter is not charged, mechanical filtering measures such as gravity settling, interception, inertial impact, and diffusion are adopted to filter larger particles in the air. In addition to mechanical

TABLE 5 Performance summary of different air purification devices

Materials	Mechanism	Filtration efficiency	Output stability	Application	References
Acrylonitrile butadiene styrene/PTFE/Ag	TENG	41% (75 min, PM2.5)	After running 10 000 cycles, the output performance is basically unchanged	Dust filter	277
Nylon and PTFE fabrics	TENG	96% (4 h, PM2.5)	After five washings, the filtration efficiency is 92%	Mask	278
PVDF-ESNF/Cu	TENG	99.2% (4 h, PM2.5)	After an interval of 30 days, the filtration efficiency is 99.2%	Mask	279
Hydrophobic nonwoven polypropylene (PP)/meltblown nonwoven PP/PTFE	TENG	99.2% (4 h, PM0.3)	After 4 cycles of testing, the filtration efficiency is 85.6%	Mask	280
Kaptont/Al/Cu/Bi ₂ Te ₃	TENG + TEG	92.1% (6 h, PM2.5)	There was no significant change in the output of the test after 10 000 min of continuous work	Gas energy recovery and purification system	281
Electrospun polyetherimide (PEI) nonwoven/Fe net	TENG	99.6% (PM0.3)	After wearing the mask for 40 h, the output did not decrease significantly	Mask	282

Abbreviations: PVDF-ESNF, poly(vinylidene fluoride) electrospun nanofiber film; TEG, thermoelectric generator.

filtration, the charged air filter can effectively remove submicron particles in PM_{2.5} via electrostatic adsorption using a strong electric field formed by friction between the two fabrics. The removal efficiency of the air filter was tested for different PM sizes, that is, PM_{0.5}, PM_{1.0}, PM_{2.5}, PM_{5.0}, PM_{10.0} (Figure 29D). The removal efficiency of the air filter after charging is considerably improved, which is analogous to that of commercial masks. To enable the application of air filter in environments with high humidity, the surface of the two fabrics were etched using inductively coupled plasma (ICP). This results in larger contact angles of water drops for the two fabrics and, consequently, higher hydrophobicity. The contact angles of water drops are presented before and after etching the two fabrics (Figure 29E,F).

The removal efficiency of the TAF for PM was tested under different humidity environments. The removal efficiency of the triboelectric air filter for PM_{1.0}–PM_{10.0} remained above 87% even with 90% relative humidity (Figure 29G). TAFs with different number of pieces (1–5 pieces) were tested at different flow rates. The more TAF pieces, the higher the removal efficiency (average 45% in one piece of TAF, average 75% in five pieces of TAF). Furthermore, the designed TAF still maintains a removal efficiency of more than 92% after five washes (Figure 29H), which is considerably higher than that of commercial masks (67%). For a practical application of the designed TAF, a TAF mask was manufactured and the

corresponding PM concentration filtered was recorded in real time. The experimental results are presented in Figure 29I. The manufactured TAF mask exhibited good filtering performance and improved the air quality index from serious pollution to an excellent level after being worn for 4 h. Due to its high efficiency and washability, the TAF is expected to be widely used as a mask in the future.

A self-powered electrostatic adsorption face mask (SEA-FM) was composed by combining the poly(vinylidene fluoride) electrospun nanofiber film (PVDF-ESNF) and a TENG driven by respiration (R-TENG).²⁷⁹ The structure and operating principle of the SEA-FM are illustrated in Figure 30A. The PVDF-ESNF prepared via electrospinning has a filtration function, and the R-TENG can continuously provide frictional charges for the PVDF-ESNF through respiration. Due to pressure changes in the mask during breathing, the Cu film and PVDF-ESNF continuously contact and separate. Thus, the charge of the PVDF-ESNF is replenished to ensure its filtering function (Figure 30B).

And cleverly, the inspiratory and expiratory parts of the mask are independent of each other, significantly limiting the influence of steam on the generation of electrostatic charge and electrostatic adsorption. Under wind speeds of 10–55 cm s⁻¹ (simulating the human respiratory rate), the removal efficiency of commercial masks and PVDF-ESNF were comparatively tested, and the results are presented (Figure 30C,D). The removal

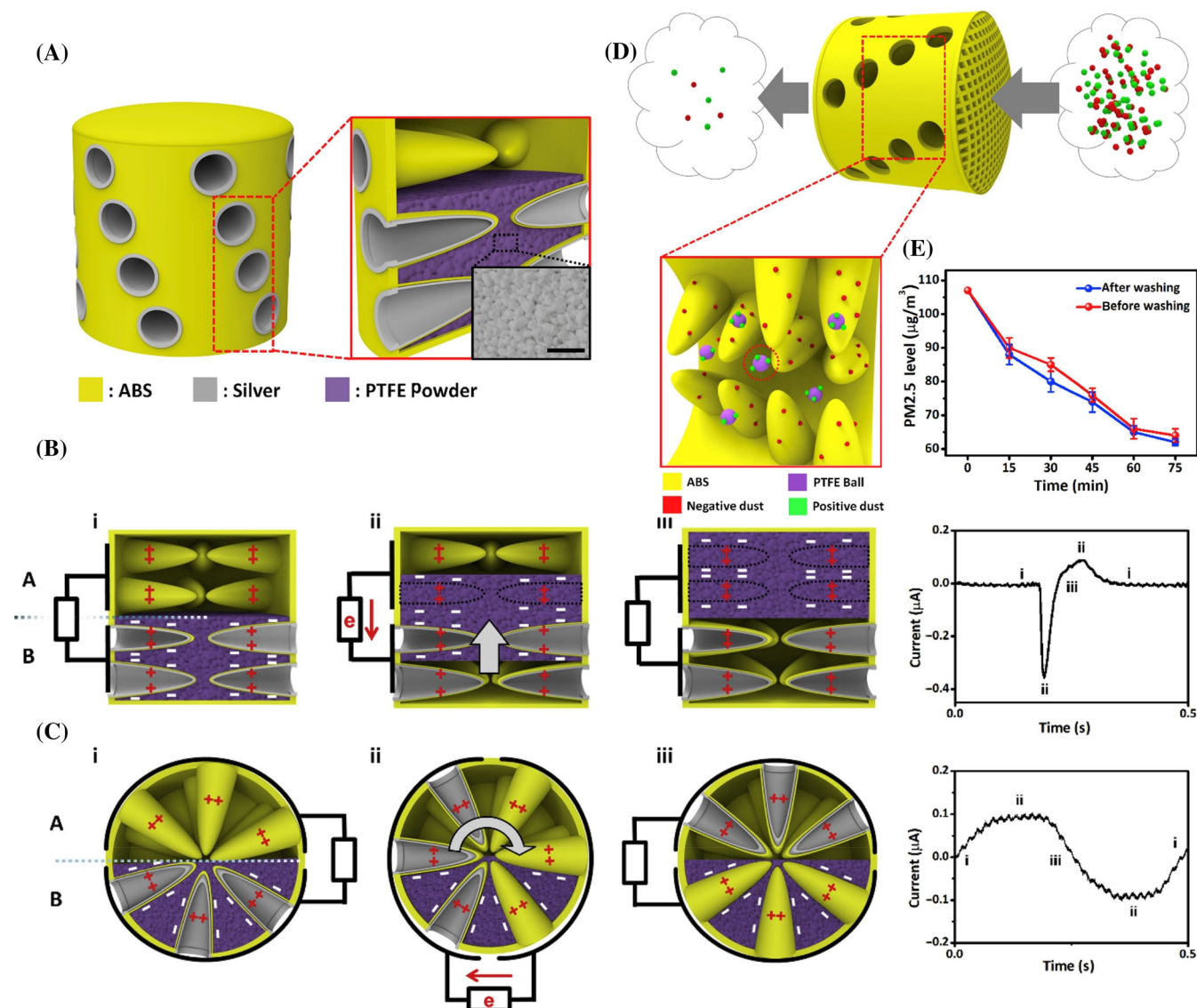


FIGURE 28 3D-printed BV-TENG and dust filter. (A) Structural diagram of the designed BV-TENG. (B) Operating principle diagram of the BV-TENG in vibration and (C) rolling modes. (D) Operating principle diagram of the BV-DF. (E) Washability experiment on the BV-DF. Reproduced with permission.²⁷⁷ Copyright 2019, Elsevier Ltd

efficiency of the PVDF-ESNF is above that of commercial masks for particles smaller than $2.5 \mu\text{m}$, and considerably higher for ultrafine particles smaller than $0.1 \mu\text{m}$. The filtering efficiency of the PVDF-ESNF with an R-TENG is considerably above that without an R-TENG (Figure 30E). To test the performance in practical application, the SEA-FM (Figure 30F) was manufactured. Figure 30G shows the particle removal efficiency during 240 min of wearing, which is basically the same as the removal efficiency measured under the same conditions after 30 days (Figure 30H), indicating that the SEA-FM has good durability. Due to its excellent durability and self-powered characteristics, the SEA-FM has significant development potential in the future wearable air purification field.

5.4 | Hybridized nanogenerators with supercapacitors

In the practical application of wearable sensor, due to the randomness of mechanical motion, the power generated by TENG cannot always keep consistent with the power required by the sensor, which will inevitably lead to the waste of power or insufficient supply. Therefore, it is necessary to store the power generated by TENG.^{283,284}

Supercapacitor (SC) seems to be one of the most suitable energy storage devices at present. It has the characteristics of rapid charge and discharge of capacitors and energy storage of batteries. In addition, compared with traditional batteries and capacitors, supercapacitors have the characteristics of high power density, long cycle life,

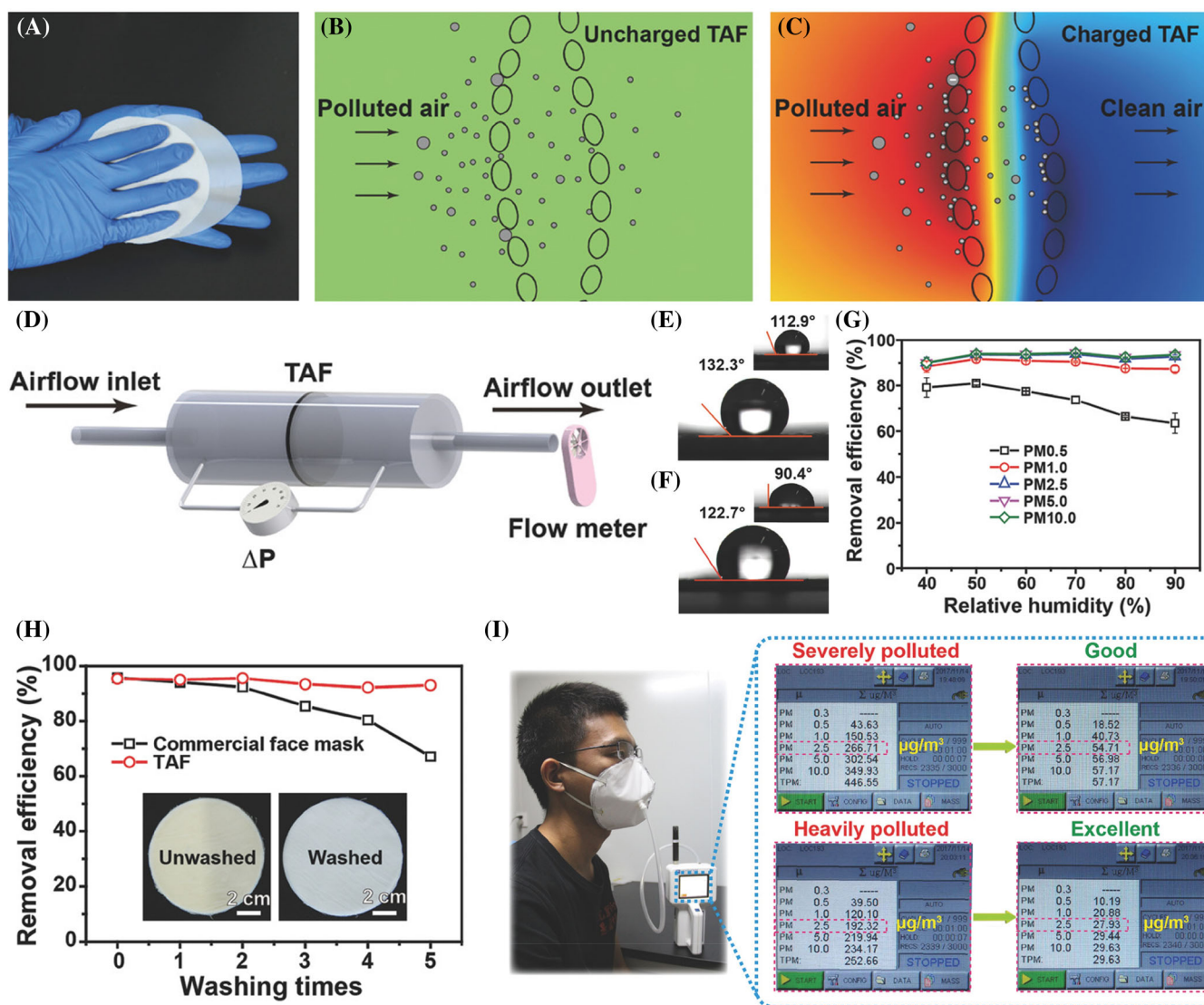


FIGURE 29 Washable multilayer TAF for efficient PM (PM_{2.5}) removal. (A) Friction process charging the TAF. (B) Uncharged TAF and (C) schematic diagram of filtration mechanism of charged TAF. (D) Schematic diagram of measuring device. Contact angle of water drops before and after etching of (E) PTFE and (F) nylon fabrics. (G) Removal efficiency test for the TAF under different humidity conditions. (H) Washability test for the TAF. (I) Removal efficiency test for mask manufactured based on the TAF. Reproduced with permission.²⁷⁸ Copyright 2018, Wiley-VCH Verlag GmbH

wide working temperature limit and environmental protection.

A novel transparent, low-power, stretchable and repairable strain sensor based on silver nanowires (AgNW)/poly(3,4-ethylenedioxythiophene):polystyrenesulfonate (PEDOT:PSS)/polyurethane (PU) nanocomposites (Figure 31D),²⁸⁵ combined with TENG (Figure 31B) and supercapacitor (Figure 31C), has a good response to various strain-causing activities on human skin (such as breathing, swallowing, clenching fist, wrist rotation, finger joint movement, etc.) (Figure 31A), and its conductivity, transmittance and sensitivity can be adjusted according to needs, which has certain advantages in personal health monitoring and artificial skin.

An integrated power supply system based on wearable fabric stores the power generated by TENG in supercapacitors (Figure 31G),²⁸⁶ which can collect both horizontal and vertical mechanical energy, and can monitor human activities such as stretching, walking, and running (Figure 31H). In addition, SC charged by TENG can also be used to light LED or as the power supply of other sensors, and has good cycle stability (after 4000 charge and discharge experiments, there is no obvious capacity change).

In order to make readers have a clearer understanding, we have made a summary table of the research progress of nanogenerators in biomedical devices such as sensors (Table 6) and therapy (Table 7) in chronological order.

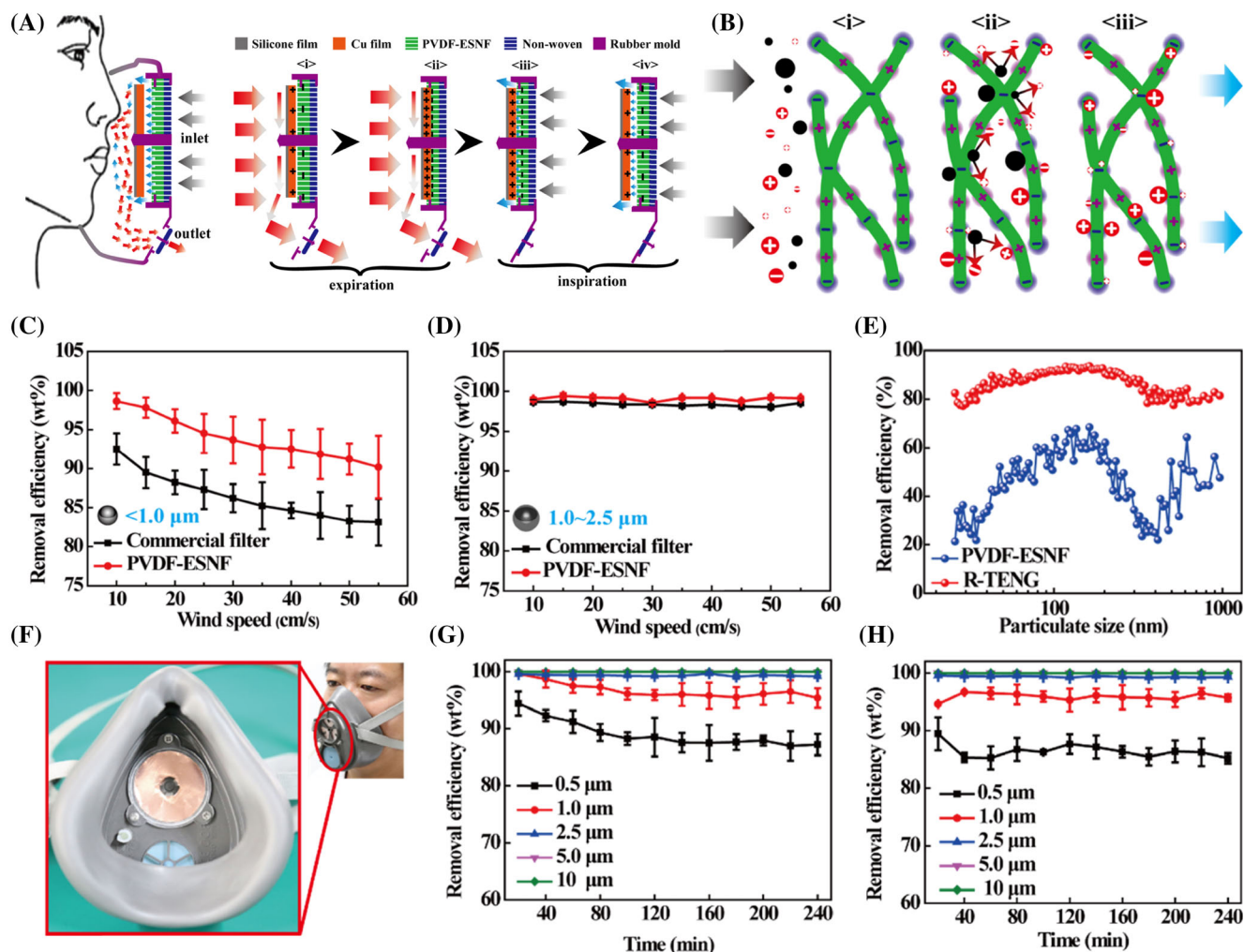


FIGURE 30 A self-powered electrostatic adsorption face mask based on a TENG. (A) Structure and operating scheme of the face mask. (B) Schematic diagram of the filtration function of the PVDF-ESNF. Under different wind speeds, the removal efficiencies of commercial masks and the PVDF-ESNF for (C) a particle size of less than $1.0 \mu\text{m}$ and (D) particle sizes from 1.0 to $2.5 \mu\text{m}$. (E) Comparison of filtration effects of the PVDF-ESNF with and without an R-TENG. (F) Photograph of the SEA-FM. SEA-FM denotes self-powered electrostatic adsorption face mask. (G) Particle removal efficiency of the SEA-FM during 240 min of wearing. (H) Removal efficiency of the SEA-FM after 30 days.²⁷⁹ Reproduced with permission. Copyright 2018, American Chemical Society

6 | FUTURE OPPORTUNITIES AND CONCLUDING REMARKS

The nanogenerator has been thoroughly investigated from all aspects such as material choice, device architecture and energy generation mechanism for over a decade. However, it is still in its infancy stage in the biomedical field. Future opportunities of biomedical and healthcare nanogenerators remain for pursuing the goal of flexibility, stability, sustainability, and comfortability. There remain several issues and challenges to be tackled.

First, the materials for electrification and sensing should offer flexibility, durability, and good biocompatibility.³⁰⁹ Indeed, the performances of nanogenerators^{310–312} could be tailored by regulating and coupling the triboelectric,³¹³ piezoelectric,³¹⁴ and pyroelectric³¹⁵

materials. The materials of sensors are required to secure the adaptation of these devices to various shapes and internal environments, that is, excellent biocompatibility.³¹⁶ The electrical interconnect is important for both biocompatible and wearable considerations.³¹⁷ For example, the traditional copper wire may generate toxic ions inside human body, while the metal wire may be tough and rigid when implicated in wearable situations. Emerging conductive materials such as graphene,^{318–321} MXene,^{322–324} and hydrogels³²⁵ may provide good electrical conductivity as alternative of metal electrodes. Therefore, the comprehensive optimization of flexible materials requires great attention from materials community.

Second, the design of the nanogenerator structure should be further miniaturized to facilitate more effective

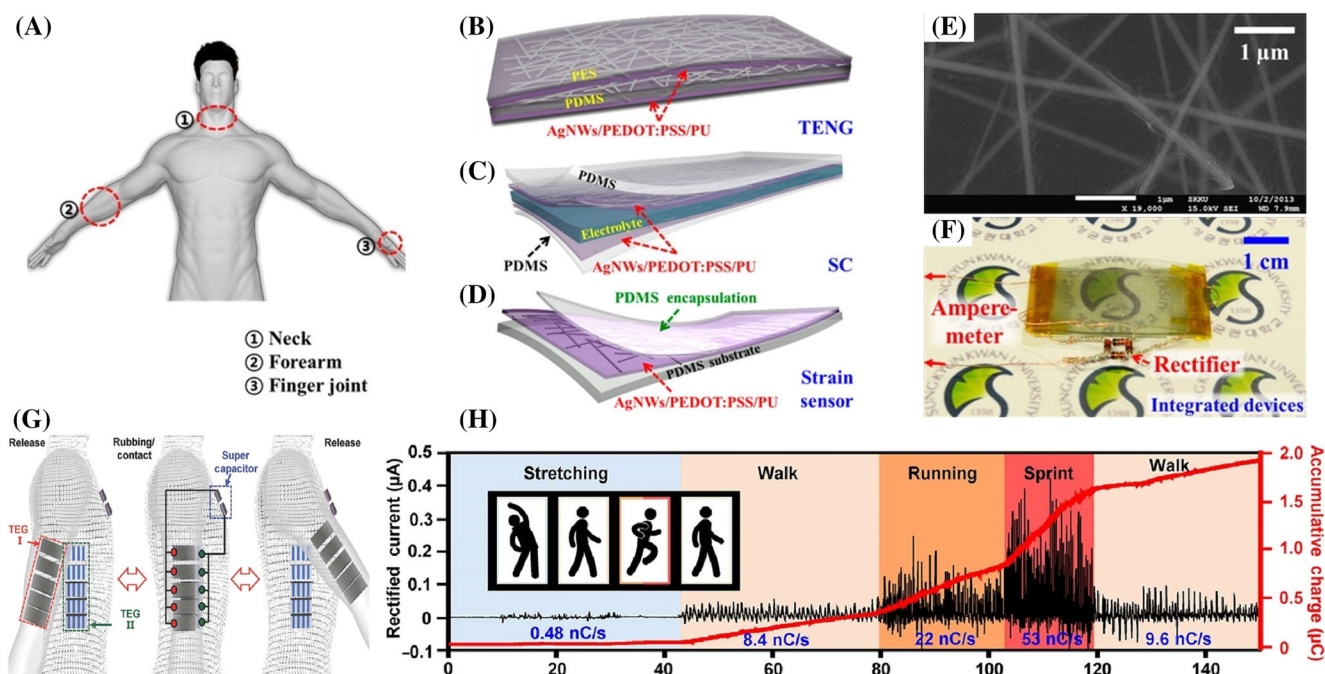


FIGURE 31 Hybridized nanogenerators with supercapacitors. (A) Schematic diagram of repairable integrated equipment on neck, forearm and knuckles. Schematic diagram of each component: (B) TENG, (C) SC, and (D) strain sensor. (E) FE-SEM images of AgNW/PEDOT:PSS/PU nanocomposite films on PDMS substrates. (F) Photographs of vertically integrated devices of strain sensor (bottom), SC (middle) and TENG (top).²⁸⁵ Reproduced with permission. Copyright 2015, American Chemical Society. (G) Schematic diagram of arm swing equipped with TENG and SC. (H) Demonstration of human activity sensor. Reproduced with permission.²⁸⁶ Copyright 2015, American Chemical Society

implantation or attachment inside and outside the human body. Besides, the comfortability should be concerned for minimizing its impact on the daily life of the patient. Besides, the large-scale production technique should be addressed for reducing the device cost. Real-world applications put forward strict requirements on the strength and durability of these device structures.³²⁶

Third, the packaging strategy for nanogenerator devices can be further modified. Traditional packaging technique has guaranteed a long lifetime of implanted systems, that is, without being affected by internal extrusion, corrosion, and oxidation by the humidity³²⁷ of body fluids. On the one hand, a reliable packaging method^{306,328,329} with negligible rejection reaction requires further investigation. On the other hand, completely degradable self-powered system may further decrease the risk of implanted systems.

Besides, signal transition remains an important issue for implanted nanogenerator systems. A low-power-consumption wireless communication means such as Zigbee technology^{330,331} and radio-frequency³³² may extend the working lifetime and reduce the surgery time. Indeed, the locating and tracking of implantable devices³³³ are highly demanded in the era of Internet of Things.^{334–336} Meanwhile, proper selection of the implantation position

for the implanted device affects the transmission of biological signals and the service life of the devices.

In addition, an appropriate power management module can reduce energy loss for long-term operation of the nanogenerator equipment. Indeed, the energy storage modules could continuously provide electric power such as a secondary battery or supercapacitor.^{337–339} The realization of most implantable devices in the target location is limited to small animals such as mice. Prior to the application to the human body, large animals with physiological characteristics analogous to the human body should be selected for testing.

It is necessary to improve the working stability and sensing accuracy. In practical applications, there are many external environmental factors that threaten the output stability of nanogenerators, such as humidity and temperature. The movement of human body leads to the release of sweat, which may cause some pollution to the nanogenerator, and the slight change of body temperature caused by movement may also affect the sensing accuracy of the nanogenerator. It is a good way to protect the nanogenerator by developing suitable package, but at the same time, it is necessary to consider the influence of package on the output of nanogenerator and human comfort. In addition, it is also an effective method to

TABLE 6 Research progress of nanogenerators in biomedical sensors

Materials	Performance	Areal size (cm ²)	Mechanism	Application	Subject	References
Silica/Cu	Monitor the infusion operation in real time and recording the infusion speed	4 × 2	TENG	Droplet flow rate monitoring	Liquid drops	287
PVDF/Au	Sensitivity 10050.6 mV Pa ⁻¹ ; V _{OC} : 64 V	2.5 × 2.5	TENG + PENG	Heart rate monitoring	Human	19
ZnO NRs-silk/Ag NWs	V _{OC} : 25 V; I _{SC} : 0.08 μA	0.5 × 0.5	PENG	Chest respiratory monitoring	Human	288
Silicone/Cu	V _{OC} : 5.75 V; I _{SC} : 0.38 μA (single TENG fiber: diameter = 700 μm, length = 2.5 cm)	n.a.	TENG	Renal edema monitoring	Adult porcine kidneys	289
Al/PTFE/Au	Sensitivity: 1.195 mV/mmHg; V _{OC} : 0.45 V; I _{SC} : 0.2 μA	1 × 1.5 × 0.1	TENG	Endocardial pressure monitoring	Male adult Yorkshire pigs	197
ZnO/Ti	The glucose concentration is 0, 0.024, 0.045, 0.076 and 0.119 g L ⁻¹ , and the output voltages are 0.49, 0.42, 0.32, 0.17, and 0.11 V, respectively	0.4 × 1.3	PENG	Detection of blood glucose level in vivo	Mouse	290
ZnO/Ti	The output voltages are 0.543, 0.458, 0.374, 0.261 and 0.079 V in 0, 1, 10, 30, and 80 mM urea solutions, respectively	0.5 × 0.5	PENG	In situ analysis of urea/uric-acid in body fluids	Mouse	291
Chitosan-glycerol film/PTFE/Al	V _{OC} : 130 V; I _{SC} : 15 μA	5 × 3	TENG	Determination of sodium chloride concentration in sweat	Sweat	292
PDMS/PVDF/Ag NWs	TENG-PENG: V _{OC} : 55 V; PyENG: V _{OC} : 86 V	3 × 3.5	TENG-PENG; PyENG	Monitoring of respiration, pulse, swallowing, and neck tilt	Human	195
Kapton/Cu	V _{OC} : 1.52 V; I _{SC} : 5.4 nA	2 × 1	TENG	Pulse monitoring	Human	192
Al/PVDF	V _{OC} : 42 V; I _{SC} : 2.5 μA	3.5 × 3.5	PyENG	Respiratory rate detection	Human	194
Agarose/BaTiO ₃ NPs/Ag	V _{OC} : 80 V; I _{SC} : 285 nA	3 × 3	PENG	Cysteine concentration detection	Cysteine	190
n-PTFE/Au/Al	V _{OC} : 10 V; I _{SC} : 4 μA	3 × 2 × 0.1	TENG	Rate monitoring of heartbeat and respiration; estimation of blood pressure and blood flow velocity	Pig	293
Stainless-steel thread/silicone rubber/skin	V _{OC} : 200 V; I _{SC} : 200 μA	16.5 × 11.4	TENG	Wrist pulse monitoring	Human	294
Cu-coated PET yarns/PI-coated yarns	V _{OC} : 4.98 V; J _{SC} : 15.50 mA/m ⁻²	6 × 4	TENG	Respiratory rate and depth monitoring	Human	193
BaTiO ₃ NPs/PVDF/Ag	V _{OC} : 5 V; I _{SC} : 900 nA	2.5 × 2.5	PENG	Glucose concentration detection	Glucose	191
Kapton/Al/Au/Ti	n.a.	11.1 × 5	TENG	Acoustic stimuli detection	Mouse	196

Abbreviations: NRs, nanorods; NPs, nanoparticles; NWs, nanowires; PET, polyethylene terephthalate; PI, polyimide.

TABLE 7 Applications of nanogenerators in biomedical therapy

Materials	Performance	Areal size (cm ²)	Mechanism	Application	Subject	References
PVDF/ZnO/rGO	V_{OC} : 4.55 V; I_{SC} : 2.95 μ A	6.5×3.5	PENG	Self-powered cardiac pacemaker	Dog	295
PVDF/Ag	V_{OC} : 200 V; Q_{SC} : 0.46 μ C	$2 \times 6 \times 0.05$	PENG	Cancer therapy	Mouse	296
PTFE/Ti/Cu	V_{OC} : 70 V; I_{SC} : 0.55 μ A	Diameter: 4	TENG	Cancer therapy	Mouse	297
Nylon/PVC/Cu	V_{OC} : 4 kV; I_{SC} : 85 μ A	30×30	TENG	Electro-assisted cell printing	HepaRG and HeLa cells	230
PTFE/Al	V_{OC} : 1200 V; I_{SC} : 20 μ A	10×10	TENG	Self-powered iontophoretic transdermal drug-delivery system	Pig skin	227
Al/PTFE/Au	V_{OC} : 60 mV; I_{SC} : 1 nA	2.0×2.0	TENG	Promote the attachment, proliferation and differentiation of osteoblasts	Murine calvarial preosteoblasts	298
PTFE/Al/Au	V_{OC} : 65.2 V; I_{SC} : 0.5 μ A	$3.9 \times 6.1 \times 0.099$	TENG	Symbiotic cardiac pacemaker	Pig	299
PTFE/Cu	V_{OC} : 160 V; I_{SC} : 100 μ A	Diameter: 18.4	TENG	Enhancing proliferation and migration of fibroblast cells	Mouse fibroblast cells	229
Se NWs/Ag NWs	V_{OC} : 0.45 V; I_{SC} : 1.67 nA	1×2	PENG	Gesture recognition and cardiovascular monitoring	Human	300
Cellular PP/PZT/Cu	Sensitivity: 0.19 V kPa ⁻¹ ; I_{SC} : 11.9 nA cm ⁻²	0.8×0.8	PENG	Measure the human heartbeat, monitor eyeball motions, and perform active tactile imaging	Human	301
PLGA/PCL/PLA	V_{OC} : 2 V; I_{SC} : 220 nA	$1.2 \times 1.2 \times 0.065$	TENG	Tissue repair	Rat	225
ITO/PET/PDMS/sponge	P_{1max} : 1.56 μ W; P_{2max} : 2.93 μ W; the effective pressure range: 13 N	2×2	TENG	Neurostimulator	Rat	302
PTFE/Cu/PDMS/Au	V_{OC} : 15 V; I_{SC} : 1.5 mA	$1 \times 1 \times 0.2$	TENG	Self-powered implantable drug-delivery system	Porcine eye	303
PDMS/Cu/PI/Au	V_{OC} : 160 V; I_{SC} : 6.7 μ A	3.1×2.5	TENG	Neural recording and effective stimulation	Rat	304
PVDF/Cu	V_{OC} : 630 mV; I_{SC} : 5.3 nA	$2 \times 0.7 \times 0.01$	PyENG	Nerve stimulation	Frog	305
n-PTFE/Al/Au	V_{OC} : 14 V; I_{SC} : 5 μ A	n.a.	TENG	Self-powered wireless cardiac monitoring in vivo	Yorkshire porcine	306
PDMS/Al/Cu	V_{OC} : 30 V; I_{SC} : 280 nA	n.a.	TENG	Accelerate highly efficient nonviral direct conversion and in vivo reprogramming	embryonic fibroblasts	231

(Continues)

TABLE 7 (Continued)

Materials	Performance	Areal size (cm ²)	Mechanism	Application	Subject	References
PTFE/Al	Sensitivity: 14.32 mV/mmHg; P_{\max} : 40 nW	n.a.	PENG	Implantable and self-powered blood pressure monitoring	Yorkshire porcine	307
Kapton/Al/Cu	V_{OC} : 300 V; I_{SC} : 30 μ A	5 \times 5	TENG	Accelerating mesenchymal stems cell differentiation	Rat	224
PLGA/PCL/Mg	V_{OC} : 40 V; I_{SC} : 1 μ A	2 \times 3	TENG	Orientation of nerve cell growth	Rat	270
Graphene/PVDF	V_{OC} : 2 V; I_{SC} : 200 nA	2 \times 2 \times 0.02	PyENG	Biological nerve stimulation	Frog and rat	308
PDMS/ITO	V_{OC} : 0.2 V; I_{SC} : 0.06 nA	1.5 \times 1.0	TENG	Implantable clinical cure for bone remodeling or orthodontic treatment	Rat	233
PIMNT/Au	V_{OC} : 11 V; I_{SC} : 283 μ A	1.7 \times 1.7	PENG	Deep brain stimulation	Mouse	228
PMN-PT	V_{OC} : 8.2 V; I_{SC} : 0.223 mA	1.7 \times 1.7	TENG	Self-powered cardiac pacemaker	Rat	232
PDMS/Al/Au	V_{OC} : 12 V; I_{SC} : 0.25 μ A	1.2 \times 1.2	TENG	Pacemaker	Rat	115
ITO/Al/PDMS	V_{OC} : 465 V; I_{SC} : 107.5 μ A	2 \times 4	TENG	Driving an implantable 3D microelectrode array for neural prosthesis	Neural prosthesis	170

Abbreviations: NWs, nanowires; PET, polyethylene terephthalate; PI, polyimide; PIMNT, $\text{Pb}(\text{In}_{1/2}\text{Nb}_{1/2})\text{O}_3\text{-Pb}(\text{Mg}_{1/3}\text{Nb}_{2/3})\text{O}_3\text{-PbTiO}_3$; PMN-PT, $(1-x)\text{Pb}(\text{Mg}_{1/3}\text{Nb}_{2/3})\text{O}_3\text{-xPbTiO}_3$; rGO, reduced graphene oxide.

change the surface morphology of nanogenerators to obtain excellent hydrophobicity.

The device performances could be elevated with the integration between sensors and nanogenerators. The interface engineering and electrical connection could be optimized for complicated device architectures.^{340,341} Besides, the energy conversion efficiency of the nanogenerators could be enhanced for self-powering. Indeed, the implantable nanogenerators have guaranteed self-powering feature for the sensing devices through the conversion of human kinetic energy into electricity.

This review summarizes the progress of nanogenerators in biomedical and healthcare applications, including self-powering, smart sensing, efficient therapy, microbial disinfection, and biodegradable implanting. The excellent innovation in healthcare could benefit from the combination of triboelectric materials, nanotechnology and biomedical systems. Indeed, the nanogenerator based biomedical and healthcare vortex may recall the great input of materials scientists, biologists, chemists, physicists, and biomedical engineers. A bright future awaits the investigation of nanogenerators for biomedical and healthcare applications.

ACKNOWLEDGMENTS

This work was financially supported by the National Natural Science Foundation of China (21975287), the start-up grant for young talent of China University of Petroleum (East China), Taishan Scholar Project (No. ts201712020), Technological Leading Scholar of 10000 Talent Project (No. W03020508), Shandong Provincial Natural Science Foundation (ZR2018ZC1458), the Scientific Research Development Plan of Shandong Higher Education Institutions (No. J18KA316), the Development Plan of Shandong Province (No. 2019GGX104019), and Guangdong Basic and Applied Basic Research Foundation (2019A1515110706). Hong Liu thanks the National Key Research and Development Program of China (2017YFB0405400) from the Ministry of Science and Technology (MOST) of China and the Project of “20 items of University” of Jinan (2018GXRC031). Weijia Zhou thanks Taishan Scholars Project Special Funds (tsqn201812083) and NSFC (No. 52022037). The authors show their gratitude to the National Natural Science Foundation of China (NSFC grant No. 51802113, 51802116) and the Natural Science Foundation of Shandong Province, China (grant No. ZR2019BEM040, ZR2018BEM015). Mark H Rummeli thanks the National Science Foundation China (NSFC,

Project 52071225), the National Science Center and the Czech Republic under the ERDF program “Institute of Environmental Technology—Excellent Research” (No. CZ.02.1.01/0.0/0.0/16_019/0000853) and the Sino-German Research Institute for support (Project No. GZ 1400).

CONFLICT OF INTEREST

The authors declare no conflict of interest.

ORCID

Jinbo Pang  <https://orcid.org/0000-0001-6965-4166>

Qiang Li  <https://orcid.org/0000-0001-8891-260X>

Weijia Zhou  <https://orcid.org/0000-0003-4339-0435>

Kai Wang  <https://orcid.org/0000-0002-3513-3511>

Hong Liu  <https://orcid.org/0000-0003-1640-9620>

Han Hu  <https://orcid.org/0000-0002-3755-7342>

REFERENCES

- Chung HU, Kim BH, Lee JY, et al. Binodal, wireless epidermal electronic systems with in-sensor analytics for neonatal intensive care. *Science*. 2019;363(6430):eaau0780.
- Rajewsky N, Almouzni G, Gorski SA, et al. LifeTime and improving European healthcare through cell-based interceptive medicine. *Nature*. 2020;587(7834):377-386.
- Haque A, Milstein A, Fei-Fei L. Illuminating the dark spaces of healthcare with ambient intelligence. *Nature*. 2020;585(7824):193-202.
- Smethurst DP, Williams HC. Power laws. Are hospital waiting lists self-regulating? *Nature*. 2001;410(6829):652-653.
- Zeggini E, Gloyn AL, Barton AC, Wain LV. Translational genomics and precision medicine: moving from the lab to the clinic. *Science*. 2019;365(6460):1409-1413.
- Hinchev R, Yoon HJ, Ryu H, et al. Transcutaneous ultrasound energy harvesting using capacitive triboelectric technology. *Science*. 2019;365(6452):491-494.
- Cook-Deegan R. Public health. Boosting health services research. *Science*. 2011;333(6048):1384-1385.
- Kang SK, Murphy RK, Hwang SW, et al. Bioresorbable silicon electronic sensors for the brain. *Nature*. 2016;530(7588):71-76.
- El-Ali J, Sorger PK, Jensen KF. Cells on chips. *Nature*. 2006;442(7101):403-411.
- Rong G, Corrie SR, Clark HA. In vivo biosensing: progress and perspectives. *ACS Sens*. 2017;2(3):327-338.
- Song Y, Min J, Gao W. Wearable and implantable electronics: moving toward precision therapy. *ACS Nano*. 2019;13(11):12280-12286.
- Curtis AB, Karki R, Hattoum A, Sharma UC. Arrhythmias in patients ≥ 80 years of age: pathophysiology, management, and outcomes. *J Am Coll Cardiol*. 2018;71(18):2041-2057.
- Liu S, Zhang XD, Gu X, Ming D. Photodetectors based on two dimensional materials for biomedical application. *Biosens Bioelectron*. 2019;143:111617.
- Rebello R, Barbosa AI, Caballero D, et al. 3D biosensors in advanced medical diagnostics of high mortality diseases. *Biosens Bioelectron*. 2019;130:20-39.
- Luo J, Gao W, Wang ZL. The triboelectric nanogenerator as an innovative technology toward intelligent sports. *Adv Mater*. 2021;33(17):2004178.
- Zhao K, Ouyang B, Bowen CR, Wang ZL, Yang Y. One-structure-based multi-effects coupled nanogenerators for flexible and self-powered multi-functional coupled sensor systems. *Nano Energy*. 2020;71:104632.
- Zhang R, Hummelgård M, Örtengren J, et al. Human body constituted triboelectric nanogenerators as energy harvesters, code transmitters, and motion sensors. *ACS Appl Energy Mater*. 2018;1(6):2955-2960.
- Gao L, Hu D, Qi M, et al. A double-helix-structured triboelectric nanogenerator enhanced with positive charge traps for self-powered temperature sensing and smart-home control systems. *Nanoscale*. 2018;10(42):19781-19790.
- Nayeem MOG, Lee S, Jin H, et al. All-nanofiber-based, ultrasensitive, gas-permeable mechanoacoustic sensors for continuous long-term heart monitoring. *Proc Natl Acad Sci U S A*. 2020;117(13):7063-7070.
- Yao MT, Cheng YX, Zhou ZY, Liu M. Recent progress on the fabrication and applications of flexible ferroelectric devices. *J Mater Chem C*. 2020;8(1):14-27.
- Li G, Lee DW. An advanced selective liquid-metal plating technique for stretchable biosensor applications. *Lab Chip*. 2017;17(20):3415-3421.
- Tai YL, Yang ZG. Flexible pressure sensing film based on ultra-sensitive SWCNT/PDMS spheres for monitoring human pulse signals. *J Mater Chem B*. 2015;3(27):5436-5441.
- Wei P, Yang X, Cao Z, et al. Flexible and stretchable electronic skin with high durability and shock resistance via embedded 3D printing technology for human activity monitoring and personal healthcare. *Adv Mater Technol*. 2019;4(9):1900315.
- Mahmud MS, Fang H, Wang HG. An integrated wearable sensor for unobtrusive continuous measurement of autonomic nervous system. *IEEE Internet Things*. 2019;6(1):1104-1113.
- Zhang Y, Webb RC, Luo H, et al. Theoretical and experimental studies of epidermal heat flux sensors for measurements of core body temperature. *Adv Healthc Mater*. 2016;5(1):119-127.
- Guo J, Zhou B, Yang C, Dai Q, Kong L. Stretchable and temperature-sensitive polymer optical fibers for wearable health monitoring. *Adv Funct Mater*. 2019;29(33):1902898.
- Cheong JH, Ng SS, Liu X, et al. An inductively powered implantable blood flow sensor microsystem for vascular grafts. *IEEE Trans Biomed Eng*. 2012;59(9):2466-2475.
- Huang C, Gu Y, Chen J, et al. A wearable fiberless optical sensor for continuous monitoring of cerebral blood flow in mice. *IEEE J Sel Top Quantum Electron*. 2019;25(1):1-8.
- Yang JC, Mun J, Kwon SY, Park S, Bao Z, Park S. Electronic skin: recent progress and future prospects for skin-attachable devices for health monitoring, robotics, and prosthetics. *Adv Mater*. 2019;31(48):1904765.
- Bu CY, Li FJ, Yin K, Pang JB, Wang LC, Wang K. Research progress and prospect of triboelectric nanogenerators as self-powered human body sensors. *ACS Appl Electron Mater*. 2020;2(4):863-878.
- Zhang X, Xi Z, Machuki JO, et al. Gold cube-in-cube based oxygen nanogenerator: a theranostic nanoplatform for modulating tumor microenvironment for precise chemo-phototherapy and multimodal imaging. *ACS Nano*. 2019;13(5):5306-5325.
- Liu Y, Feig VR, Bao Z. Conjugated polymer for implantable electronics toward clinical application. *Adv Healthc Mater*. 2021;10(17):2001916.

33. Lee GH, Moon H, Kim H, et al. Multifunctional materials for implantable and wearable photonic healthcare devices. *Nat Rev Mater*. 2020;5(2):149-165.
34. Abraham WT, Stough WG, Pina IL, et al. Trials of implantable monitoring devices in heart failure: which design is optimal? *Nat Rev Cardiol*. 2014;11(10):576-585.
35. Paruchuri V, Adhaduk M, Garikipati NV, Steinberg JS, Mittal S. Clinical utility of a novel wireless implantable loop recorder in the evaluation of patients with unexplained syncope. *Heart Rhythm*. 2011;8(6):858-863.
36. Manian U, Gula LJ. Arrhythmia management in the elderly-implanted cardioverter defibrillators and prevention of sudden death. *Can J Cardiol*. 2016;32(9):1117-1123.
37. Graziosi M, Nanni C, Lorenzini M, et al. Role of (1)(8)F-FDG PET/CT in the diagnosis of infective endocarditis in patients with an implanted cardiac device: a prospective study. *Eur J Nucl Med Mol Imaging*. 2014;41(8):1617-1623.
38. Brailova M, Clerfond G, Tresorier R, et al. Inherited metabolic diseases and cardiac pathology in adults: diagnosis and prevalence in a CardioMetabo study. *J Clin Med*. 2020;9(3):694.
39. Humar M, Dobravec A, Zhao X, Yun SH. Biomaterial micro-lasers implantable in the cornea, skin, and blood. *Optica*. 2017;4(9):1080-1085.
40. Walk J, Weber J, Soell C, Weigel R, Fischer G, Ussmueller T. Remote powered medical implants for telemonitoring. *Proc IEEE*. 2014;102(11):1811-1832.
41. Perrin T, Boveda S, Defaye P, et al. Role of medical reaction in management of inappropriate ventricular arrhythmia diagnosis: the inappropriate Therapy and HOme monitoRiNg (THORN) registry. *EP Europace*. 2019;21(4):607-615.
42. Jung YH, Kim JU, Lee JS, et al. Injectable biomedical devices for sensing and stimulating internal body organs. *Adv Mater*. 2020;32(16):1907478.
43. Bai W, Yang H, Ma Y, et al. Flexible transient optical waveguides and surface-wave biosensors constructed from monocrystalline silicon. *Adv Mater*. 2018;30(32):1801584.
44. Cohn WE, Timms DL, Frazier OH. Total artificial hearts: past, present, and future. *Nat Rev Cardiol*. 2015;12(10):609-617.
45. Jang J, Kim JY, Kim YC, et al. A 3D micro scaffold cochlear electrode array for steroid elution. *Adv Healthc Mater*. 2019;8(20):1900379.
46. Farra R, Sheppard NF Jr, McCabe L, et al. First-in-human testing of a wirelessly controlled drug delivery microchip. *Sci Transl Med*. 2012;4(122):122ra121.
47. Dolan EB, Varela CE, Mendez K, et al. An actuatable soft reservoir modulates host foreign body response. *Sci Robot*. 2019;4(33):eaax7043.
48. Mirani B, Pagan E, Shojaei S, et al. Facile method for fabrication of meter-long multifunctional hydrogel fibers with controllable biophysical and biochemical features. *ACS Appl Mater Interfaces*. 2020;12(8):9080-9089.
49. Löffler S, Seyock S, Nybom R, Jacobson GB, Richter-Dahlfors A. Electrochemically triggered release of acetylcholine from sCO₂ impregnated conductive polymer films evokes intracellular Ca²⁺ signaling in neurotypic SH-SY5Y cells. *J Control Release*. 2016;243:283-290.
50. Mejia Oneto JM, Gupta M, Leach JK, Lee M, Sutcliffe JL. Implantable biomaterial based on click chemistry for targeting small molecules. *Acta Biomater*. 2014;10(12):5099-5105.
51. Hou T-C, Yang Y, Lin Z-H, et al. Nanogenerator based on zinc blende CdTe micro/nanowires. *Nano Energy*. 2013;2(3):387-393.
52. Koydemir HC, Ozcan A. Wearable and implantable sensors for biomedical applications. *Annu Rev Anal Chem*. 2018;11(1):127-146.
53. Wu YH, Zhen RM, Liu HZ, et al. Liquid metal fiber composed of a tubular channel as a high-performance strain sensor. *J Mater Chem C*. 2017;5(47):12483-12491.
54. Xu M, Obodo D, Yadavalli VK. The design, fabrication, and applications of flexible biosensing devices. *Biosens Bioelectron*. 2019;124-125:96-114.
55. Faerber J, Cummins G, Pavuluri SK, et al. In vivo characterization of a wireless telemetry module for a capsule endoscopy system utilizing a conformal antenna. *IEEE Trans Biomed Circuits Syst*. 2018;12(1):95-105.
56. Sai CT. A low-operating-voltage wireless intermediate-range scheme for energy and signal transmission by magnetic coupling for implantable devices. *IEEE J Emerging Sel Top Power Electron*. 2015;3(1):242-251.
57. Tjong FV, Reddy VY. Permanent leadless cardiac pacemaker therapy: a comprehensive review. *Circulation*. 2017;135(15):1458-1470.
58. Grijalva SI, Gu JM, Li J, et al. Engineered cardiac pacemaker nodes created by TBX18 gene transfer overcome source-sink mismatch. *Adv Sci (Weinh)*. 2019;6(22):1901099.
59. Dong L, Closson AB, Jin C, et al. Multifunctional pacemaker lead for cardiac energy harvesting and pressure sensing. *Adv Healthc Mater*. 2020;9(11):2000053.
60. Tang SC, Lun TLT, Guo ZY, Kwok KW, McDannold NJ. Intermediate range wireless power transfer with segmented coil transmitters for implantable heart pumps. *IEEE Trans Power Electron*. 2017;32(5):3844-3857.
61. Chew DJ, Zhu L, Delivopoulos E, et al. A microchannel neuroprosthesis for bladder control after spinal cord injury in rat. *Sci Transl Med*. 2013;5(210):210ra155.
62. Lobel DA, Lee KH. Brain machine interface and limb reanimation technologies: restoring function after spinal cord injury through development of a bypass system. *Mayo Clin Proc*. 2014;89(5):708-714.
63. Torre-Amione G, Alo K, Estep JD, et al. Spinal cord stimulation is safe and feasible in patients with advanced heart failure: early clinical experience. *Eur J Heart Fail*. 2014;16(7):788-795.
64. Dieter A, Keppeler D, Moser T. Towards the optical cochlear implant: optogenetic approaches for hearing restoration. *EMBO Mol Med*. 2020;12(4):e11618.
65. Xu M, Ma D, Chen D, et al. Preparation, characterization and application research of a sustained dexamethasone releasing electrode coating for cochlear implantation. *Mater Sci Eng C*. 2018;90:16-26.
66. Gong S, Yap LW, Zhu Y, et al. A soft resistive acoustic sensor based on suspended standing nanowire membranes with point crack design. *Adv Funct Mater*. 2020;30(25):1910717.
67. Li Q, Li H, Xia Q, et al. Extra storage capacity in transition metal oxide lithium-ion batteries revealed by in situ magnetometry. *Nat Mater*. 2021;20(1):76-83.
68. Jia X, Yang Y, Wang C, et al. Biocompatible ionic liquid-biopolymer electrolyte-enabled thin and compact magnesium-air batteries. *ACS Appl Mater Interfaces*. 2014;6(23):21110-21117.

69. Hu H, Li Q, Li LQ, et al. Laser irradiation of electrode materials for energy storage and conversion. *Matter*. 2020;3(1):95-126.
70. Bock DC, Marschilok AC, Takeuchi KJ, Takeuchi ES. Batteries used to power implantable biomedical devices. *Electrochim Acta*. 2012;84:155-164.
71. Mardanpour MM, Yaghmaei S. Characterization of a microfluidic microbial fuel cell as a power generator based on a nickel electrode. *Biosens Bioelectron*. 2016;79:327-333.
72. Sode K, Yamazaki T, Lee I, Hanashi T, Tsugawa W. Bio-Capacitor: a novel principle for biosensors. *Biosens Bioelectron*. 2016;76:20-28.
73. Corbett GD, Lim YC, Lee JC, Chernoleskiy A, Pugh PJ, Cameron EA. Safety of the colonoscope magnetic imaging device (ScopeGuide) in patients with implantable cardiac devices. *Endoscopy*. 2014;46(2):135-138.
74. Sandhu AT, Goldhaber-Fiebert JD, Owens DK, Turakhia MP, Kaiser DW, Heidenreich PA. Cost-effectiveness of implantable pulmonary artery pressure monitoring in chronic heart failure. *JACC Heart Fail*. 2016;4(5):368-375.
75. Aslam S, Xie R, Cowger J, et al. Bloodstream infections in mechanical circulatory support device recipients in the International Society of Heart and Lung Transplantation Mechanically Assisted Circulation Support Registry: epidemiology, risk factors, and mortality. *J Heart Lung Transplant*. 2018;37(8):1013-1020.
76. Chabin X, Taghli-Lamalle O, Mulliez A, et al. Bioimpedance analysis is safe in patients with implanted cardiac electronic devices. *Clin Nutr*. 2019;38(2):806-811.
77. Zhang K, Wang Y, Yang Y. Structure design and performance of hybridized nanogenerators. *Adv Funct Mater*. 2018;29(41):1806435.
78. Zhang K, Yang Y. Linear-grating hybridized electromagnetic-triboelectric nanogenerator for sustainably powering portable electronics. *Nano Res*. 2016;9(4):974-984.
79. Zhang K, Wang ZL, Yang Y. Conductive fabric-based stretchable hybridized nanogenerator for scavenging biomechanical energy. *ACS Nano*. 2016;10(4):4728-4734.
80. Xu Q, Qin Y. Theoretical study of enhancing the piezoelectric nanogenerator's output power by optimizing the external force's shape. *APL Mater*. 2017;5(7):074101.
81. Cui X, Xu Q, Ni X, Zhang Y, Qin Y. Atomic-thick 2D MoS₂/insulator interjection structures for enhancing nanogenerator output. *J Mater Chem C*. 2018;6(4):899-906.
82. Tian G, Deng WL, Gao YY, et al. Rich lamellar crystal baklava-structured PZT/PVDF piezoelectric sensor toward individual table tennis training. *Nano Energy*. 2019;59:574-581.
83. Hu C, Cheng L, Wang Z, Zheng Y, Bai S, Qin Y. A transparent antipeep piezoelectric nanogenerator to harvest tapping energy on screen. *Small*. 2016;12(10):1315-1321.
84. Liu S, Wang L, Feng X, et al. Ultrasensitive 2D ZnO piezotronic transistor array for high resolution tactile imaging. *Adv Mater*. 2017;29(16):1606346.
85. Wang C, Lai SK, Wang ZC, Wang JM, Yang WQ, Ni YQ. A low-frequency, broadband and tri-hybrid energy harvester with septuple-stable nonlinearity-enhanced mechanical frequency up-conversion mechanism for powering portable electronics. *Nano Energy*. 2019;64:103943.
86. Xi Y, Guo H, Zi Y, et al. Multifunctional TENG for blue energy scavenging and self-powered wind-speed sensor. *Adv Energy Mater*. 2017;7(12):1602397.
87. Lingam D, Parikh AR, Huang J, Jain A, Minary-Jolandan M. Nano/microscale pyroelectric energy harvesting: challenges and opportunities. *Int J Smart Nano Mater*. 2013;4(4):229-245.
88. Bowen CR, Taylor J, LeBoulbar E, Zabek D, Chauhan A, Vaish R. Pyroelectric materials and devices for energy harvesting applications. *Energy Environ Sci*. 2014;7(12):3836-3856.
89. Wang Z, Yu R, Pan C, et al. Light-induced pyroelectric effect as an effective approach for ultrafast ultraviolet nanosensing. *Nat Commun*. 2015;6:8401.
90. Cheng G, Lin ZH, Du ZL, Wang ZL. Increase output energy and operation frequency of a triboelectric nanogenerator by two grounded electrodes approach. *Adv Funct Mater*. 2014;24(19):2892-2898.
91. Xie L, Chen X, Wen Z, et al. Spiral steel wire based fiber-shaped stretchable and tailorable triboelectric nanogenerator for wearable power source and active gesture sensor. *Nanomicro Lett*. 2019;11(1):39.
92. Wang X, Yang Y. Effective energy storage from a hybridized electromagnetic-triboelectric nanogenerator. *Nano Energy*. 2017;32:36-41.
93. Chen B, Yang N, Jiang Q, Chen W, Yang Y. Transparent triboelectric nanogenerator-induced high voltage pulsed electric field for a self-powered handheld printer. *Nano Energy*. 2018;44:468-475.
94. Li C, Yin Y, Wang B, et al. Self-powered electrospinning system driven by a triboelectric nanogenerator. *ACS Nano*. 2017;11(10):10439-10445.
95. Wang ZL, Song J. Piezoelectric nanogenerators based on zinc oxide nanowire arrays. *Science*. 2006;312(5771):242-246.
96. Xiao L, Wu SY, Yang SL. Parametric study on the thermoelectric conversion performance of a concentrated solar-driven thermionic-thermoelectric hybrid generator. *Int J Energy Res*. 2018;42(2):656-672.
97. Wang ZL. Triboelectric nanogenerators as new energy technology for self-powered systems and as active mechanical and chemical sensors. *ACS Nano*. 2013;7(11):9533-9557.
98. Fan FR, Tian ZQ, Wang ZL. Flexible triboelectric generator! *Nano Energy*. 2012;1(2):328-334.
99. Yang Y, Guo W, Pradel KC, et al. Pyroelectric nanogenerators for harvesting thermoelectric energy. *Nano Lett*. 2012;12(6):2833-2838.
100. Hasan MAM, Wang Y, Bowen CR, Yang Y. 2D nanomaterials for effective energy scavenging. *Nanomicro Lett*. 2021;13(1):82.
101. Wang ZL. Self-powered nanotech. *Sci Am*. 2008;298(1):82-87.
102. Zhao X, Chen B, Wei GD, Wu JM, Han W, Yang Y. Polyimide/graphene nanocomposite foam-based wind-driven triboelectric nanogenerator for self-powered pressure sensor. *Adv Mater Technol*. 2019;4(5):1800723.
103. Ji Y, Zhang K, Yang Y. A one-structure-based multieffects coupled nanogenerator for simultaneously scavenging thermal, solar, and mechanical energies. *Adv Sci*. 2018;5(2):1700622.
104. Jiang Q, Chen B, Yang Y. Wind-driven triboelectric nanogenerators for scavenging biomechanical energy. *ACS Appl Energy Mater*. 2018;1(8):4269-4276.

105. Jiang Q, Chen B, Zhang K, Yang Y. Ag nanoparticle-based triboelectric nanogenerator to scavenge wind energy for a self-charging power unit. *ACS Appl Mater Interfaces*. 2017;9(50):43716-43723.
106. Yang Y, Zhu G, Zhang H, et al. Triboelectric nanogenerator for harvesting wind energy and as self-powered wind vector sensor system. *ACS Nano*. 2013;7(10):9461-9468.
107. Xie Y, Wang S, Lin L, et al. Rotary triboelectric nanogenerator based on a hybridized mechanism for harvesting wind energy. *ACS Nano*. 2013;7(8):7119-7125.
108. Meng XS, Zhu G, Wang ZL. Robust thin-film generator based on segmented contact-electrification for harvesting wind energy. *ACS Appl Mater Interfaces*. 2014;6(11):8011-8016.
109. Zhang H, Wang J, Xie Y, et al. Self-powered, wireless, remote meteorologic monitoring based on triboelectric nanogenerator operated by scavenging wind energy. *ACS Appl Mater Interfaces*. 2016;8(48):32649-32654.
110. Hu J, Pu XJ, Yang HM, et al. A flutter-effect-based triboelectric nanogenerator for breeze energy collection from arbitrary directions and self-powered wind speed sensor. *Nano Res*. 2019;12(12):3018-3023.
111. Zi Y, Guo H, Wen Z, Yeh MH, Hu C, Wang ZL. Harvesting low-frequency (<5 Hz) irregular mechanical energy: a possible killer application of triboelectric nanogenerator. *ACS Nano*. 2016;10(4):4797-4805.
112. Xie Y, Wang S, Niu S, et al. Grating-structured freestanding triboelectric-layer nanogenerator for harvesting mechanical energy at 85% total conversion efficiency. *Adv Mater*. 2014;26(38):6599-6607.
113. Jiang T, Chen XY, Han CB, Tang W, Wang ZL. Theoretical study of rotary freestanding triboelectric nanogenerators. *Adv Funct Mater*. 2015;25(19):2928-2938.
114. Li Z, Zhu G, Yang R, Wang AC, Wang ZL. Muscle-driven in vivo nanogenerator. *Adv Mater*. 2010;22(23):2534-2537.
115. Zheng Q, Shi B, Fan F, et al. In vivo powering of pacemaker by breathing-driven implanted triboelectric nanogenerator. *Adv Mater*. 2014;26(33):5851-5856.
116. Zhao K, Wang X, Yang Y. Ultra-stable electret nanogenerator to scavenge high-speed rotational energy for self-powered electronics. *Adv Mater Technol*. 2017;2(1):1600233.
117. Xia GT, Huang YN, Li FJ, et al. A thermally flexible and multi-site tactile sensor for remote 3D dynamic sensing imaging. *Front Chem Sci Eng*. 2020;14(6):1039-1051.
118. Zhao K, Wang ZL, Yang Y. Self-powered wireless smart sensor node enabled by an ultrastable, highly efficient, and superhydrophobic-surface-based triboelectric nanogenerator. *ACS Nano*. 2016;10(9):9044-9052.
119. Gao PX, Ding Y, Mai W, Hughes WL, Lao C, Wang ZL. Conversion of zinc oxide nanobelts into superlattice-structured nanohelices. *Science*. 2005;309(5741):1700-1704.
120. Kong XY, Ding Y, Yang R, Wang ZL. Single-crystal nanorings formed by epitaxial self-coiling of polar nanobelts. *Science*. 2004;303(5662):1348-1351.
121. Pan ZW, Dai ZR, Wang ZL. Nanobelts of semiconducting oxides. *Science*. 2001;291(5510):1947-1949.
122. Guo W, Tan C, Shi K, et al. Wireless piezoelectric devices based on electrospun PVDF/BaTiO₃ NW nanocomposite fibers for human motion monitoring. *Nanoscale*. 2018;10(37):17751-17760.
123. Shi KM, Huang XY, Sun B, Wu ZY, He JL, Jiang PK. Cellulose/BaTiO₃ aerogel paper based flexible piezoelectric nanogenerators and the electric coupling with triboelectricity. *Nano Energy*. 2019;57:450-458.
124. Zhao J, Li F, Wang Z, Dong P, Xia G, Wang K. Flexible PVDF nanogenerator-driven motion sensors for human body motion energy tracking and monitoring. *J Mater Sci Mater Electron*. 2021;32(11):14715-14727.
125. Xu S, Hansen BJ, Wang ZL. Piezoelectric-nanowire-enabled power source for driving wireless microelectronics. *Nat Commun*. 2010;1:93.
126. Qin Y, Wang X, Wang ZL. Microfibre-nanowire hybrid structure for energy scavenging. *Nature*. 2008;451(7180):809-813.
127. Wu WZ, Wang ZL. Piezotronics and piezo-phototronics for adaptive electronics and optoelectronics. *Nat Rev Mater*. 2016;1(7):16031.
128. Pan CF, Dong L, Zhu G, et al. High-resolution electroluminescent imaging of pressure distribution using a piezoelectric nanowire LED array. *Nat Photonics*. 2013;7(9):752-758.
129. Yang R, Qin Y, Dai L, Wang ZL. Power generation with laterally packaged piezoelectric fine wires. *Nat Nanotechnol*. 2009;4(1):34-39.
130. Li W, Torres D, Diaz R, et al. Nanogenerator-based dual-functional and self-powered thin patch loudspeaker or microphone for flexible electronics. *Nat Commun*. 2017;8:15310.
131. Wu W, Wang L, Li Y, et al. Piezoelectricity of single-atomic-layer MoS₂ for energy conversion and piezotronics. *Nature*. 2014;514(7523):470-474.
132. Luo J, Wang ZL. Recent progress of triboelectric nanogenerators: from fundamental theory to practical applications. *EcoMat*. 2020;2(4):e12059.
133. Feng X, Li Q, Wang K. Waste plastic triboelectric nanogenerators using recycled plastic bags for power generation. *ACS Appl Mater Interfaces*. 2021;13(1):400-410.
134. Cui N, Dai C, Liu J, et al. Increasing the output charge quantity of triboelectric nanogenerators via frequency multiplication with a multigap-structured friction layer. *Energy Environ Sci*. 2020;13(7):2069-2076.
135. Zou H, Zhang Y, Guo L, et al. Quantifying the triboelectric series. *Nat Commun*. 2019;10(1):1427.
136. Feng X, Zhang Y, Kang L, et al. Integrated energy storage system based on triboelectric nanogenerator in electronic devices. *Front Chem Sci Eng*. 2021;15(2):238-250.
137. Matsunaga M, Hirotsani J, Kishimoto S, Ohno Y. High-output, transparent, stretchable triboelectric nanogenerator based on carbon nanotube thin film toward wearable energy harvesters. *Nano Energy*. 2020;67:104297.
138. Wu C, Wang AC, Ding W, Guo H, Wang ZL. Triboelectric nanogenerator: a foundation of the energy for the new era. *Adv Energy Mater*. 2019;9(1):1802906.
139. Luo JJ, Xu L, Tang W, et al. Direct-current triboelectric nanogenerator realized by air breakdown induced ionized air channel. *Adv Energy Mater*. 2018;8(27):1800889.
140. Quan T, Wu Y, Yang Y. Hybrid electromagnetic-triboelectric nanogenerator for harvesting vibration energy. *Nano Res*. 2015;8(10):3272-3280.
141. Quan T, Yang Y. Fully enclosed hybrid electromagnetic-triboelectric nanogenerator to scavenge vibrational energy. *Nano Res*. 2016;9(8):2226-2233.

142. Chen X, Gao LX, Chen JF, et al. A chaotic pendulum triboelectric–electromagnetic hybridized nanogenerator for wave energy scavenging and self-powered wireless sensing system. *Nano Energy*. 2020;69:104440.
143. Quan T, Wang ZL, Yang Y. A shared-electrode-based hybridized electromagnetic–triboelectric nanogenerator. *ACS Appl Mater Interfaces*. 2016;8(30):19573-19578.
144. Wang ZL. Triboelectric nanogenerators as new energy technology and self-powered sensors—principles, problems and perspectives. *Faraday Discuss*. 2014;176:447-458.
145. Cao X, Jie Y, Wang N, Wang ZL. Triboelectric nanogenerators driven self-powered electrochemical processes for energy and environmental science. *Adv Energy Mater*. 2016;6(23):1600665.
146. Wang ZL. On Maxwell's displacement current for energy and sensors: the origin of nanogenerators. *Mater Today*. 2017;20(2):74-82.
147. Zhu G, Pan C, Guo W, et al. Triboelectric-generator-driven pulse electrodeposition for micropatterning. *Nano Lett*. 2012;12(9):4960-4965.
148. Guo H, Jia X, Liu L, Cao X, Wang N, Wang ZL. Freestanding triboelectric nanogenerator enables noncontact motion-tracking and positioning. *ACS Nano*. 2018;12(4):3461-3467.
149. Yu Y, Li Z, Wang Y, Gong S, Wang X. Sequential infiltration synthesis of doped polymer films with tunable electrical properties for efficient triboelectric nanogenerator development. *Adv Mater*. 2015;27(33):4938-4944.
150. Tang Q, Pu XJ, Zeng QX, et al. A strategy to promote efficiency and durability for sliding energy harvesting by designing alternating magnetic stripe arrays in triboelectric nanogenerator. *Nano Energy*. 2019;66:104087.
151. Zhang Z, Zhang J, Zhang H, et al. A portable triboelectric nanogenerator for real-time respiration monitoring. *Nanoscale Res Lett*. 2019;14(1):354.
152. Rahman MT, Salauddin M, Maharjan P, Rasel MS, Cho H, Park JY. Natural wind-driven ultra-compact and highly efficient hybridized nanogenerator for self-sustained wireless environmental monitoring system. *Nano Energy*. 2019;57:256-268.
153. Nahian SA, Cheedarala RK, Ahn KK. A study of sustainable green current generated by the fluid-based triboelectric nanogenerator (FluTENG) with a comparison of contact and sliding mode. *Nano Energy*. 2017;38:447-456.
154. Wang S, Lin L, Xie Y, Jing Q, Niu S, Wang ZL. Sliding-triboelectric nanogenerators based on in-plane charge-separation mechanism. *Nano Lett*. 2013;13(5):2226-2233.
155. Khandelwal G, Minocha T, Yadav SK, et al. All edible materials derived biocompatible and biodegradable triboelectric nanogenerator. *Nano Energy*. 2019;65:104016.
156. Chen J, Guo HY, Wu ZY, et al. Actuation and sensor integrated self-powered cantilever system based on TENG technology. *Nano Energy*. 2019;64:103920.
157. Su Y, Yang Y, Zhong X, et al. Fully enclosed cylindrical single-electrode-based triboelectric nanogenerator. *ACS Appl Mater Interfaces*. 2014;6(1):553-559.
158. Bai ZQ, Zhang Z, Li JY, Guo JS. Textile-based triboelectric nanogenerators with high-performance via optimized functional elastomer composited tribomaterials as wearable power source. *Nano Energy*. 2019;65:104012.
159. Wu YH, Luo Y, Qu JK, Daoud WA, Qi T. Liquid single-electrode triboelectric nanogenerator based on graphene oxide dispersion for wearable electronics. *Nano Energy*. 2019;64:103948.
160. Ankanahalli Shankaregowda S, Sagade Muktar Ahmed RF, Nanjegowda CB, et al. Single-electrode triboelectric nanogenerator based on economical graphite coated paper for harvesting waste environmental energy. *Nano Energy*. 2019;66:104141.
161. Yang Y, Zhang H, Lin ZH, et al. Human skin based triboelectric nanogenerators for harvesting biomechanical energy and as self-powered active tactile sensor system. *ACS Nano*. 2013;7(10):9213-9222.
162. Paosangthong W, Wagih M, Torah R, Beeby S. Textile-based triboelectric nanogenerator with alternating positive and negative freestanding grating structure. *Nano Energy*. 2019;66:104148.
163. Zhang DH, Shi JW, Si YL, Li T. Multi-grating triboelectric nanogenerator for harvesting low-frequency ocean wave energy. *Nano Energy*. 2019;61:132-140.
164. Shao HY, Wen Z, Cheng P, et al. Multifunctional power unit by hybridizing contact–separate triboelectric nanogenerator, electromagnetic generator and solar cell for harvesting blue energy. *Nano Energy*. 2017;39:608-615.
165. Niu SM, Liu Y, Chen XY, et al. Theory of freestanding triboelectric-layer-based nanogenerators. *Nano Energy*. 2015;12:760-774.
166. Chen Y, Wang Y-C, Zhang Y, et al. Elastic-beam triboelectric nanogenerator for high-performance multifunctional applications: sensitive scale, acceleration/force/vibration sensor, and intelligent keyboard. *Adv Energy Mater*. 2018;8(29):1802159.
167. Wang S, Xie Y, Niu S, Lin L, Wang ZL. Freestanding triboelectric-layer-based nanogenerators for harvesting energy from a moving object or human motion in contact and non-contact modes. *Adv Mater*. 2014;26(18):2818-2824.
168. Fan FR, Lin L, Zhu G, Wu W, Zhang R, Wang ZL. Transparent triboelectric nanogenerators and self-powered pressure sensors based on micropatterned plastic films. *Nano Lett*. 2012;12(6):3109-3114.
169. Wang S, Lin L, Wang ZL. Nanoscale triboelectric-effect-enabled energy conversion for sustainably powering portable electronics. *Nano Lett*. 2012;12(12):6339-6346.
170. Zhang XS, Han MD, Wang RX, et al. Frequency-multiplication high-output triboelectric nanogenerator for sustainably powering biomedical microsystems. *Nano Lett*. 2013;13(3):1168-1172.
171. Zhang XS, Zhu FY, Han MD, Sun XM, Peng XH, Zhang HX. Self-cleaning poly(dimethylsiloxane) film with functional micro/nano hierarchical structures. *Langmuir*. 2013;29(34):10769-10775.
172. Meng B, Tang W, Zhang X, Han M, Liu W, Zhang H. Self-powered flexible printed circuit board with integrated triboelectric generator. *Nano Energy*. 2013;2(6):1101-1106.
173. Liu W, Han M, Sun X, Meng B, Zhang X-S, Zhang H. An unmovable single-layer triboelectric generator driven by sliding friction. *Nano Energy*. 2014;9:401-407.
174. Shao J, Jiang T, Wang Z. Theoretical foundations of triboelectric nanogenerators (TENGs). *Sci China Technol Sci*. 2020;63(7):1087-1109.

175. Li X, Lau TH, Guan D, Zi Y. A universal method for quantitative analysis of triboelectric nanogenerators. *J Mater Chem A*. 2019;7(33):19485-19494.
176. Zi Y, Niu S, Wang J, Wen Z, Tang W, Wang ZL. Standards and figure-of-merits for quantifying the performance of triboelectric nanogenerators. *Nat Commun*. 2015;6:8376.
177. Shao J, Jiang T, Tang W, Chen X, Xu L, Wang ZL. Structural figure-of-merits of triboelectric nanogenerators at powering loads. *Nano Energy*. 2018;51:688-697.
178. Peng J, Kang SD, Snyder GJ. Optimization principles and the figure of merit for triboelectric generators. *Sci Adv*. 2017;3(12):eaap8576.
179. Meier D, Reinhardt D, van Straaten M, et al. Longitudinal spin Seebeck effect contribution in transverse spin Seebeck effect experiments in Pt/YIG and Pt/NFO. *Nat Commun*. 2015;6:8211.
180. Wang H, Ail U, Gabrielson R, Berggren M, Crispin X. Ionic Seebeck effect in conducting polymers. *Adv Energy Mater*. 2015;5(11):1500044.
181. Mistewicz K, Jesionek M, Nowak M, Koziol M. SbSeI pyroelectric nanogenerator for a low temperature waste heat recovery. *Nano Energy*. 2019;64:103906.
182. Lee J-H, Ryu H, Kim T-Y, et al. Thermally induced strain-coupled highly stretchable and sensitive pyroelectric nanogenerators. *Adv Energy Mater*. 2015;5(18):1500704.
183. Qi J, Ma N, Yang Y. Photovoltaic-pyroelectric coupled effect based nanogenerators for self-powered photodetector system. *Adv Mater Interfaces*. 2018;5(3):1701189.
184. Zhang K, Wang S, Yang Y. A one-structure-based piezo-tribo-pyro-photoelectric effects coupled nanogenerator for simultaneously scavenging mechanical, thermal, and solar energies. *Adv Energy Mater*. 2016;7(6):1601852.
185. Zhang D, Wang Y, Yang Y. Design, performance, and application of thermoelectric nanogenerators. *Small*. 2019;15(32):1805241.
186. Zhang K, Wang Y, Wang ZL, Yang Y. Standard and figure-of-merit for quantifying the performance of pyroelectric nanogenerators. *Nano Energy*. 2019;55:534-540.
187. Yang Y, Jung JH, Yun BK, et al. Flexible pyroelectric nanogenerators using a composite structure of lead-free KNbO₃ nanowires. *Adv Mater*. 2012;24(39):5357-5362.
188. Hinchet R, Kim SW. Wearable and implantable mechanical energy harvesters for self-powered biomedical systems. *ACS Nano*. 2015;9(8):7742-7745.
189. Sun JY, Yang AP, Zhao CC, Liu F, Li Z. Recent progress of nanogenerators acting as biomedical sensors in vivo. *Sci Bull*. 2019;64(18):1336-1347.
190. Selvarajan S, Alluri NR, Chandrasekhar A, Kim SJ. Direct detection of cysteine using functionalized BaTiO₃ nanoparticles film based self-powered biosensor. *Biosens Bioelectron*. 2017;91(19):203-210.
191. Selvarajan S, Alluri NR, Chandrasekhar A, Kim SJ. BaTiO₃ nanoparticles as biomaterial film for self-powered glucose sensor application. *Sens Actuators B*. 2016;234:395-403.
192. Ouyang H, Tian J, Sun G, et al. Self-powered pulse sensor for antidiastole of cardiovascular disease. *Adv Mater*. 2017;29(40):1703456.
193. Zhao Z, Yan C, Liu Z, et al. Machine-washable textile triboelectric nanogenerators for effective human respiratory monitoring through loom weaving of metallic yarns. *Adv Mater*. 2016;28(46):10267-10274.
194. Xue H, Yang Q, Wang DY, et al. A wearable pyroelectric nanogenerator and self-powered breathing sensor. *Nano Energy*. 2017;38:147-154.
195. Sun JG, Yang TN, Wang CY, Chen LJ. A flexible transparent one-structure tribo-piezo-pyroelectric hybrid energy generator based on bio-inspired silver nanowires network for biomechanical energy harvesting and physiological monitoring. *Nano Energy*. 2018;48:383-390.
196. Jang J, Lee J, Jang JH, Choi H. A triboelectric-based artificial basilar membrane to mimic cochlear tonotopy. *Adv Healthc Mater*. 2016;5(19):2481-2487.
197. Liu Z, Ma Y, Ouyang H, et al. Transcatheter self-powered ultrasensitive endocardial pressure sensor. *Adv Funct Mater*. 2019;29(3):1807560.
198. Li G, Zhang H, Meng L, et al. Adjustment of oxygen vacancy states in ZnO and its application in ppb-level NO₂ gas sensor. *Sci Bull*. 2020;65(19):1650-1658.
199. Xu Q, Lou J, Zhang R, Ma B, Bai S, Qin Y. Self-cleaning and self-powered UV sensors for highly reliable outdoor UV detection. *ACS Appl Electron Mater*. 2020;2(6):1628-1634.
200. Yang LJ, Chi S, Dong SP, et al. Preparation and characterization of a novel piezoelectric nanogenerator based on soluble and meltable copolyimide for harvesting mechanical energy. *Nano Energy*. 2020;67:104220.
201. Zi YL, Wang ZL. Nanogenerators: an emerging technology towards nanoenergy. *APL Mater*. 2017;5(7):074103.
202. He X, Wu X, Shi W, Ma H. Comparison of N-acetylcysteine and cysteine in their ability to replenish intracellular cysteine by a specific fluorescent probe. *Chem Commun*. 2016;52(60):9410-9413.
203. Zhao Z, Liu Q, Bliven S, Xie L, Bourne PE. Determining cysteines available for covalent inhibition across the human kinome. *J Med Chem*. 2017;60(7):2879-2889.
204. Yin J, Ren W, Yang G, et al. L-cysteine metabolism and its nutritional implications. *Mol Nutr Food Res*. 2016;60(1):134-146.
205. Leong DP, Joseph PG, McKee M, et al. Reducing the global burden of cardiovascular disease, part 2: prevention and treatment of cardiovascular disease. *Circ Res*. 2017;121(6):695-710.
206. Henson JB, Simon TG, Kaplan A, Osganian S, Masia R, Corey KE. Advanced fibrosis is associated with incident cardiovascular disease in patients with non-alcoholic fatty liver disease. *Aliment Pharmacol Ther*. 2020;51(7):728-736.
207. So-Armah K, Benjamin LA, Bloomfield GS, et al. HIV and cardiovascular disease. *Lancet HIV*. 2020;7(4):e279-e293.
208. Balakumar P, Maung UK, Jagadeesh G. Prevalence and prevention of cardiovascular disease and diabetes mellitus. *Pharmacol Res*. 2016;113(pt A):600-609.
209. Mathew RO, Bangalore S, Lavelle MP, et al. Diagnosis and management of atherosclerotic cardiovascular disease in chronic kidney disease: a review. *Kidney Int*. 2017;91(4):797-807.
210. Zhang TF, Chang HC, Wu YP, et al. Macroscopic and direct light propulsion of bulk graphene material. *Nat Photonics*. 2015;9(7):471-476.
211. Liu L, Yu Y, Yan C, Li K, Zheng Z. Wearable energy-dense and power-dense supercapacitor yarns enabled by scalable

- graphene-metallic textile composite electrodes. *Nat Commun.* 2015;6:7260.
212. Weng W, Chen P, He S, Sun X, Peng H. Smart electronic textiles. *Angew Chem Int Ed Engl.* 2016;55(21):6140-6169.
213. Wang X, Dai Y, Liu R, He X, Li S, Wang ZL. Light-triggered pyroelectric nanogenerator based on a pn-junction for self-powered near-infrared photosensing. *ACS Nano.* 2017;11(8):8339-8345.
214. Li MN, Porter AL, Wang ZL. Evolutionary trend analysis of nanogenerator research based on a novel perspective of phased bibliographic coupling. *Nano Energy.* 2017;34:93-102.
215. Liao XQ, Liao QL, Zhang Z, et al. A highly stretchable ZnO@fiber-based multifunctional nanosensor for strain/temperature/UV detection. *Adv Funct Mater.* 2016;26(18):3074-3081.
216. You MH, Wang XX, Yan X, et al. A self-powered flexible hybrid piezoelectric-pyroelectric nanogenerator based on non-woven nanofiber membranes. *J Mater Chem A.* 2018;6(8):3500-3509.
217. Ko YJ, Kim DY, Won SS, et al. Flexible $\text{Pb}(\text{Zr}_{0.52}\text{Ti}_{0.48})\text{O}_3$ films for a hybrid piezoelectric-pyroelectric nanogenerator under harsh environments. *ACS Appl Mater Interfaces.* 2016;8(10):6504-6511.
218. Olusanya BO, Neumann KJ, Saunders JE. The global burden of disabling hearing impairment: a call to action. *Bull WH O.* 2014;92(5):367-373.
219. Amat-Santos IJ, Varela-Falcon LH, Abraham WT. Current and future percutaneous strategies for the treatment of acute and chronic heart failure. *Rev Esp Cardiol (Engl Ed).* 2017;70(5):382-390.
220. Velazquez EJ, Bonow RO. Revascularization in severe left ventricular dysfunction. *J Am Coll Cardiol.* 2015;65(6):615-624.
221. Noly PE, Pagani FD, Noiseux N, et al. Continuous-flow left ventricular assist devices and Valvular heart disease: a comprehensive review. *Can J Cardiol.* 2020;36(2):244-260.
222. Feng H, Zhao C, Tan P, Liu R, Chen X, Li Z. Nanogenerator for biomedical applications. *Adv Healthc Mater.* 2018;7(10):1701298.
223. Yu Y, Sun H, Orbay H, et al. Biocompatibility and in vivo operation of implantable mesoporous PVDF-based nanogenerators. *Nano Energy.* 2016;27:275-281.
224. Guo W, Zhang X, Yu X, et al. Self-powered electrical stimulation for enhancing neural differentiation of mesenchymal stem cells on graphene-poly(3,4-ethylenedioxythiophene) hybrid microfibers. *ACS Nano.* 2016;10(5):5086-5095.
225. Li Z, Feng HQ, Zheng Q, et al. Photothermally tunable biodegradation of implantable triboelectric nanogenerators for tissue repairing. *Nano Energy.* 2018;54:390-399.
226. Zhang Y, Zhou Z, Sun L, Liu Z, Xia X, Tao TH. "Genetically engineered" biofunctional triboelectric nanogenerators using recombinant spider silk. *Adv Mater.* 2018;30(50):1805722.
227. Wu C, Jiang P, Li W, et al. Self-powered iontophoretic transdermal drug delivery system driven and regulated by biomechanical motions. *Adv Funct Mater.* 2019;30(3):1907378.
228. Hwang GT, Kim Y, Lee JH, et al. Self-powered deep brain stimulation via a flexible PIMNT energy harvester. *Energy Environ Sci.* 2015;8(9):2677-2684.
229. Hu WT, Wei XL, Zhu L, et al. Enhancing proliferation and migration of fibroblast cells by electric stimulation based on triboelectric nanogenerator. *Nano Energy.* 2019;57:600-607.
230. Huo HN, Liu F, Luo YX, et al. Triboelectric nanogenerators for electro-assisted cell printing. *Nano Energy.* 2020;67:104150.
231. Jin Y, Seo J, Lee JS, et al. Triboelectric nanogenerator accelerates highly efficient nonviral direct conversion and in vivo reprogramming of fibroblasts to functional neuronal cells. *Adv Mater.* 2016;28(34):7365-7374.
232. Hwang GT, Park H, Lee JH, et al. Self-powered cardiac pacemaker enabled by flexible single crystalline PMN-PT piezoelectric energy harvester. *Adv Mater.* 2014;26(28):4880-4887.
233. Tang W, Tian J, Zheng Q, et al. Implantable self-powered low-level laser cure system for mouse embryonic osteoblasts' proliferation and differentiation. *ACS Nano.* 2015;9(8):7867-7873.
234. Hou Y, Jiang N, Zhang L, et al. Oppositely charged polyurethane microspheres with tunable zeta potentials as an injectable dual-loaded system for bone repair. *ACS Appl Mater Interfaces.* 2017;9(31):25808-25817.
235. Chan JM, Zervantonakis IK, Rimchala T, Polacheck WJ, Whisler J, Kamm RD. Engineering of in vitro 3D capillary beds by self-directed angiogenic sprouting. *PLoS One.* 2012;7(12):e50582.
236. Xie J, Jiang J, Davoodi P, Srinivasan MP, Wang CH. Electrohydrodynamic atomization: a two-decade effort to produce and process micro-/nanoparticulate materials. *Chem Eng Sci.* 2015;125:32-57.
237. Skoog SA, Elam JW, Narayan RJ. Atomic layer deposition: medical and biological applications. *Int Mater Rev.* 2013;58(2):113-129.
238. Yin M, Xiao L, Liu Q, et al. 3D printed microheater sensor-integrated, drug-encapsulated microneedle patch system for pain management. *Adv Healthc Mater.* 2019;8(23):1901170.
239. Lee H, Song C, Hong YS, et al. Wearable/disposable sweat-based glucose monitoring device with multistage transdermal drug delivery module. *Sci Adv.* 2017;3(3):e1601314.
240. Beloqui A, Solinis MA, Rodriguez-Gascon A, Almeida AJ, Preat V. Nanostructured lipid carriers: promising drug delivery systems for future clinics. *Nanomedicine.* 2016;12(1):143-161.
241. Larrañeta E, Lutton REM, Woolfson AD, Donnelly RF. Micro-needle arrays as transdermal and intradermal drug delivery systems: materials science, manufacture and commercial development. *Mater Sci Eng R Rep.* 2016;104:1-32.
242. Yu M, Wu J, Shi J, Farokhzad OC. Nanotechnology for protein delivery: overview and perspectives. *J Control Release.* 2016;240:24-37.
243. Grimaldi N, Andrade F, Segovia N, et al. Lipid-based nanovesicles for nanomedicine. *Chem Soc Rev.* 2016;45(23):6520-6545.
244. Hu X, Yu J, Qian C, et al. H_2O_2 -responsive vesicles integrated with transcutaneous patches for glucose-mediated insulin delivery. *ACS Nano.* 2017;11(1):613-620.
245. Cao N, Huang Y, Zheng J, et al. Conversion of human fibroblasts into functional cardiomyocytes by small molecules. *Science.* 2016;352(6290):1216-1220.
246. Weinberger L, Ayyash M, Novershtern N, Hanna JH. Dynamic stem cell states: naive to primed pluripotency in

- rodents and humans. *Nat Rev Mol Cell Biol.* 2016;17(3):155-169.
247. Feinberg AP, Koldobskiy MA, Gondor A. Epigenetic modulators, modifiers and mediators in cancer aetiology and progression. *Nat Rev Genet.* 2016;17(5):284-299.
248. Caiazza M, Okawa Y, Ranga A, Piersigilli A, Tabata Y, Lutolf MP. Defined three-dimensional microenvironments boost induction of pluripotency. *Nat Mater.* 2016;15(3):344-352.
249. Ocampo A, Reddy P, Martinez-Redondo P, et al. In vivo amelioration of age-associated hallmarks by partial reprogramming. *Cell.* 2016;167(7):1719-1733.
250. Takahashi K, Yamanaka S. A decade of transcription factor-mediated reprogramming to pluripotency. *Nat Rev Mol Cell Biol.* 2016;17(3):183-193.
251. Chronis C, Fiziev P, Papp B, et al. Cooperative binding of transcription factors orchestrates reprogramming. *Cell.* 2017;168(3):442-459.
252. Hu C, Ye H, Jain G, Schmidt C. Remaining useful life assessment of lithium-ion batteries in implantable medical devices. *J Power Sources.* 2018;375:118-130.
253. Hu C, Jain G, Schmidt C, Strief C, Sullivan M. Online estimation of lithium-ion battery capacity using sparse Bayesian learning. *J Power Sources.* 2015;289:105-113.
254. Ashbaugh AG, Jiang X, Zheng J, et al. Polymeric nanofiber coating with tunable combinatorial antibiotic delivery prevents biofilm-associated infection in vivo. *Proc Natl Acad Sci U S A.* 2016;113(45):E6919-E6928.
255. Yazici H, O'Neill MB, Kacar T, et al. Engineered chimeric peptides as antimicrobial surface coating agents toward infection-free implants. *ACS Appl Mater Interfaces.* 2016;8(8):5070-5081.
256. Timmermann L, Jain R, Chen L, et al. Multiple-source current steering in subthalamic nucleus deep brain stimulation for Parkinson's disease (the VANTAGE study): a non-randomised, prospective, multicentre, open-label study. *Lancet Neurol.* 2015;14(7):693-701.
257. Bairo F, Fiorilli S, Vitale-Brovarone C. Bioactive glass-based materials with hierarchical porosity for medical applications: review of recent advances. *Acta Biomater.* 2016;42:18-32.
258. Zhang Q, Dong T, Li P, Wu MX. Noninvasive low-level laser therapy for thrombocytopenia. *Sci Transl Med.* 2016;8(349):349ra101.
259. Assis L, Milares LP, Almeida T, et al. Aerobic exercise training and low-level laser therapy modulate inflammatory response and degenerative process in an experimental model of knee osteoarthritis in rats. *Osteoarthr Cartil.* 2016;24(1):169-177.
260. Ge MK, He WL, Chen J, et al. Efficacy of low-level laser therapy for accelerating tooth movement during orthodontic treatment: a systematic review and meta-analysis. *Lasers Med Sci.* 2015;30(5):1609-1618.
261. Zhu YG, Zhao Y, Li B, et al. Continental-scale pollution of estuaries with antibiotic resistance genes. *Nat Microbiol.* 2017;2(4):16270.
262. Forouzanfar MH, Afshin A, Alexander LT, et al. Global, regional, and national comparative risk assessment of 79 behavioural, environmental and occupational, and metabolic risks or clusters of risks, 1990-2015: a systematic analysis for the Global Burden of Disease Study 2015. *Lancet.* 2016;388(10053):1659-1724.
263. Santhosh C, Velmurugan V, Jacob G, Jeong SK, Grace AN, Bhatnagar A. Role of nanomaterials in water treatment applications: a review. *Chem Eng J.* 2016;306:1116-1137.
264. Jiang QW, Jie Y, Han Y, et al. Self-powered electrochemical water treatment system for sterilization and algae removal using water wave energy. *Nano Energy.* 2015;18:81-88.
265. Zhao XJ, Tian JJ, Kuang SY, et al. Biocide-free antifouling on insulating surface by wave-driven triboelectrification-induced potential oscillation. *Adv Mater Interfaces.* 2016;3(17):1600187.
266. Ding WB, Zhou JF, Cheng J, et al. TriboPump: a low-cost, hand-powered water disinfection system. *Adv Energy Mater.* 2019;9(27):1901320.
267. Tian J, Feng H, Yan L, et al. A self-powered sterilization system with both instant and sustainable anti-bacterial ability. *Nano Energy.* 2017;36:241-249.
268. Chatterjee S, Saxena M, Padmanabhan D, Jayachandra M, Pandya HJ. Futuristic medical implants using bioresorbable materials and devices. *Biosens Bioelectron.* 2019;142:111489.
269. Rüegg M, Blum R, Boero G, Brugger J. Biodegradable frequency-selective magnesium radio-frequency microresonators for transient biomedical implants. *Adv Funct Mater.* 2019;29(39):1903051.
270. Zheng Q, Zou Y, Zhang Y, et al. Biodegradable triboelectric nanogenerator as a life-time designed implantable power source. *Sci Adv.* 2016;2(3):e1501478.
271. Curry EJ, Ke K, Chorsi MT, et al. Biodegradable piezoelectric force sensor. *Proc Natl Acad Sci U S A.* 2018;115(5):909-914.
272. Gong H, Xu Z, Yang Y, et al. Transparent, stretchable and degradable protein electronic skin for biomechanical energy scavenging and wireless sensing. *Biosens Bioelectron.* 2020;169:112567.
273. Di Q, Wang Y, Zanobetti A, et al. Air pollution and mortality in the medicare population. *N Engl J Med.* 2017;376(26):2513-2522.
274. Giles-Corti B, Vernez-Moudon A, Reis R, et al. City planning and population health: a global challenge. *Lancet.* 2016;388(10062):2912-2924.
275. Burnett R, Chen H, Szyszkowicz M, et al. Global estimates of mortality associated with long-term exposure to outdoor fine particulate matter. *Proc Natl Acad Sci U S A.* 2018;115(38):9592-9597.
276. Chen J, Huang Y, Li G, An T, Hu Y, Li Y. VOCs elimination and health risk reduction in e-waste dismantling workshop using integrated techniques of electrostatic precipitation with advanced oxidation technologies. *J Hazard Mater.* 2016;302:395-403.
277. Yoon HJ, Kim DH, Seung W, et al. 3D-printed biomimetic-villus structure with maximized surface area for triboelectric nanogenerator and dust filter. *Nano Energy.* 2019;63:103857.
278. Bai Y, Han CB, He C, et al. Washable multilayer triboelectric air filter for efficient particulate matter PM2.5 Removal. *Adv Funct Mater.* 2018;28(15):1706680.
279. Liu G, Nie J, Han C, et al. Self-powered electrostatic adsorption face mask based on a triboelectric nanogenerator. *ACS Appl Mater Interfaces.* 2018;10(8):7126-7133.
280. Zhang R, Xu Q, Bai S, et al. Enhancing the filtration efficiency and wearing time of disposable surgical masks using TENG technology. *Nano Energy.* 2021;79:105434.

281. Ma M, Zhang Z, Liao Q, et al. Integrated hybrid nanogenerator for gas energy recycle and purification. *Nano Energy*. 2017;39:524-531.
282. Cheng Y, Wang C, Zhong J, et al. Electrospun polyetherimide electret nonwoven for bi-functional smart face mask. *Nano Energy*. 2017;34:562-569.
283. Liu X, Zhao K, Wang ZL, Yang Y. Unity convoluted design of Solid li-ion battery and triboelectric nanogenerator for self-powered wearable electronics. *Adv Energy Mater*. 2017;7(22):1701629.
284. Gao T, Zhao K, Liu X, Yang Y. Implanting a solid Li-ion battery into a triboelectric nanogenerator for simultaneously scavenging and storing wind energy. *Nano Energy*. 2017;41:210-216.
285. Hwang BU, Lee JH, Trung TQ, et al. Transparent stretchable self-powered patchable sensor platform with ultrasensitive recognition of human activities. *ACS Nano*. 2015;9(9):8801-8810.
286. Jung S, Lee J, Hyeon T, Lee M, Kim DH. Fabric-based integrated energy devices for wearable activity monitors. *Adv Mater*. 2014;26(36):6329-6334.
287. Hu S, Shi Z, Zheng R, et al. Superhydrophobic liquid-solid contact triboelectric nanogenerator as a droplet sensor for biomedical applications. *ACS Appl Mater Interfaces*. 2020;12(36):40021-40030.
288. Gogurla N, Roy B, Kim S. Self-powered artificial skin made of engineered silk protein hydrogel. *Nano Energy*. 2020;77:105242.
289. Tong YX, Feng Z, Kim J, Robertson JL, Jia XT, Johnson BN. 3D printed stretchable triboelectric nanogenerator fibers and devices. *Nano Energy*. 2020;75:104973.
290. Zhang W, Zhang L, Gao H, et al. Self-powered implantable skin-like glucometer for real-time detection of blood glucose level in vivo. *Nanomicro Lett*. 2018;10(2):32.
291. Yang W, Han W, Gao H, et al. Self-powered implantable electronic-skin for in situ analysis of urea/uric-acid in body fluids and the potential applications in real-time kidney-disease diagnosis. *Nanoscale*. 2018;10(4):2099-2107.
292. Jao YT, Yang PK, Chiu CM, et al. A textile-based triboelectric nanogenerator with humidity-resistant output characteristic and its applications in self-powered healthcare sensors. *Nano Energy*. 2018;50:513-520.
293. Ma Y, Zheng Q, Liu Y, et al. Self-powered, one-stop, and multifunctional implantable triboelectric active sensor for real-time biomedical monitoring. *Nano Lett*. 2016;16(10):6042-6051.
294. Lai YC, Deng J, Zhang SL, Niu S, Guo H, Wang ZL. Single-thread-based wearable and highly stretchable triboelectric nanogenerators and their applications in cloth-based self-powered human-interactive and biomedical sensing. *Adv Funct Mater*. 2017;27(1):1604462.
295. Azimi S, Golabchi A, Nekookar A, et al. Self-powered cardiac pacemaker by piezoelectric polymer nanogenerator implant. *Nano Energy*. 2021;83:105781.
296. Liu Z, Xu L, Zheng Q, et al. Human motion driven self-powered photodynamic system for long-term autonomous cancer therapy. *ACS Nano*. 2020;14(7):8074-8083.
297. Zhao CC, Feng HQ, Zhang LJ, et al. Highly efficient in vivo cancer therapy by an implantable magnet triboelectric nanogenerator. *Adv Funct Mater*. 2019;29(41):1808640.
298. Tian J, Shi R, Liu Z, et al. Self-powered implantable electrical stimulator for osteoblasts' proliferation and differentiation. *Nano Energy*. 2019;59:705-714.
299. Ouyang H, Liu Z, Li N, et al. Symbiotic cardiac pacemaker. *Nat Commun*. 2019;10(1):1821.
300. Wu M, Wang YX, Gao SJ, et al. Solution-synthesized chiral piezoelectric selenium nanowires for wearable self-powered human-integrated monitoring. *Nano Energy*. 2019;56:693-699.
301. Yan C, Deng W, Jin L, et al. Epidermis-inspired ultrathin 3D cellular sensor array for self-powered biomedical monitoring. *ACS Appl Mater Interfaces*. 2018;10(48):41070-41075.
302. Lee S, Wang H, Wang J, et al. Battery-free neuromodulator for peripheral nerve direct stimulation. *Nano Energy*. 2018;50:148-158.
303. Song P, Kuang S, Panwar N, et al. A self-powered implantable drug-delivery system using biokinetic energy. *Adv Mater*. 2017;29(11):1605668.
304. Lee S, Wang H, Shi Q, et al. Development of battery-free neural interface and modulated control of tibialis anterior muscle via common peroneal nerve based on triboelectric nanogenerators (TENGs). *Nano Energy*. 2017;33:1-11.
305. Zhao T, Jiang W, Liu B, et al. Flexible multichannel-stimulator for motor neuroprosthesis in vivo by remotely driven in vitro. *Nano Energy*. 2016;30:146-154.
306. Zheng Q, Zhang H, Shi B, et al. In vivo self-powered wireless cardiac monitoring via implantable triboelectric nanogenerator. *ACS Nano*. 2016;10(7):6510-6518.
307. Cheng XL, Xue X, Ma Y, et al. Implantable and self-powered blood pressure monitoring based on a piezoelectric thinfilm: simulated, in vitro and in vivo studies. *Nano Energy*. 2016;22:453-460.
308. Liu H, Zhao T, Jiang W, et al. Flexible battery-less bio-electronic implants: wireless powering and manipulation by near-infrared light. *Adv Funct Mater*. 2015;25(45):7071-7079.
309. Gao LX, Chen X, Lu S, et al. Enhancing the output performance of triboelectric nanogenerator via grating-electrode-enabled surface plasmon excitation. *Adv Energy Mater*. 2019;9(44):1902725.
310. Surmenev RA, Chernozem RV, Pariy IO, Surmeneva MA. A review on piezo- and pyroelectric responses of flexible nano- and micropatterned polymer surfaces for biomedical sensing and energy harvesting applications. *Nano Energy*. 2021;79:105442.
311. Sun Y, Sun B, He J, Wang C. Compositional and structural engineering of inorganic nanowires toward advanced properties and applications. *InfoMat*. 2019;1(4):496-524.
312. Ryu H, Yoon HJ, Kim SW. Hybrid energy harvesters: toward sustainable energy harvesting. *Adv Mater*. 2019;31(34):1802898.
313. Yu A, Zhu Y, Wang W, Zhai J. Progress in triboelectric materials: toward high performance and widespread applications. *Adv Funct Mater*. 2019;29(41):1900098.
314. Chorsi MT, Curry EJ, Chorsi HT, et al. Piezoelectric biomaterials for sensors and actuators. *Adv Mater*. 2019;31(1):1802084.
315. He H, Lu X, Hanc E, Chen C, Zhang H, Lu L. Advances in lead-free pyroelectric materials: a comprehensive review. *J Mater Chem C*. 2020;8(5):1494-1516.
316. Wang H, Sun P, Yin L, Sheng X. 3D electronic and photonic structures as active biological interfaces. *InfoMat*. 2019;2(3):527-552.
317. Li S, Zhang Y, Wang Y, et al. Physical sensors for skin-inspired electronics. *InfoMat*. 2019;2(1):184-211.
318. Reina G, Gonzalez-Dominguez JM, Criado A, Vazquez E, Bianco A, Prato M. Promises, facts and challenges for graphene in biomedical applications. *Chem Soc Rev*. 2017;46(15):4400-4416.
319. Tucek J, Blonski P, Ugolotti J, Swain AK, Enoki T, Zboril R. Emerging chemical strategies for imprinting magnetism in

- graphene and related 2D materials for spintronic and biomedical applications. *Chem Soc Rev.* 2018;47(11):3899-3990.
320. Syama S, Mohanan PV. Comprehensive application of graphene: emphasis on biomedical concerns. *Nanomicro Lett.* 2019;11(1):6.
321. Dasari Shareena TP, McShan D, Dasmahapatra AK, Tchounwou PB. A review on graphene-based nanomaterials in biomedical applications and risks in environment and health. *Nanomicro Lett.* 2018;10(3):53.
322. Huang K, Li Z, Lin J, Han G, Huang P. Two-dimensional transition metal carbides and nitrides (MXenes) for biomedical applications. *Chem Soc Rev.* 2018;47(14):5109-5124.
323. Lin H, Chen Y, Shi J. Insights into 2D MXenes for versatile biomedical applications: current advances and challenges ahead. *Adv Sci (Weinh).* 2018;5(10):1800518.
324. Soleymaniha M, Shahbazi MA, Rafieerad AR, Maleki A, Amiri A. Promoting role of MXene nanosheets in biomedical sciences: therapeutic and biosensing innovations. *Adv Health Mater.* 2019;8(1):1801137.
325. Peng Q, Chen J, Wang T, et al. Recent advances in designing conductive hydrogels for flexible electronics. *InfoMat.* 2020;2(5):843-865.
326. Yang SX, Chen YJ, Jiang CB. Strain engineering of two-dimensional materials: methods, properties, and applications. *InfoMat.* 2021;3(4):397-420.
327. Nguyen V, Yang R. Effect of humidity and pressure on the triboelectric nanogenerator. *Nano Energy.* 2013;2(5):604-608.
328. Guo H, Yeh MH, Lai YC, et al. All-in-one shape-adaptive self-charging power package for wearable electronics. *ACS Nano.* 2016;10(11):10580-10588.
329. Seol M-L, Han J-W, Park S-J, Jeon S-B, Choi Y-K. Hybrid energy harvester with simultaneous triboelectric and electromagnetic generation from an embedded floating oscillator in a single package. *Nano Energy.* 2016;23:50-59.
330. Lazaro M, Lazaro A, Villarino R. Feasibility of backscatter communication using LoRAWAN signals for deep implanted devices and wearable applications. *Sensors.* 2020;20(21):6342.
331. Gil J, Kim J-H, Kim CS, et al. A fully integrated low-power high-coexistence 2.4-GHz ZigBee transceiver for biomedical and healthcare applications. *IEEE Trans Microw Theory Tech.* 2014;62(9):1879-1889.
332. Cai MY, Wang ZY, Luo Y, Mirabbasi S. An RF-powered crystalless double-mixing receiver for miniaturized biomedical implants. *IEEE Trans Microw Theory Tech.* 2018;66(11):5129-5140.
333. Umay I, Fidan B, Barshan B. Localization and tracking of implantable biomedical sensors. *Sensors.* 2017;17(3):583.
334. Fan X, He J, Mu J, et al. Triboelectric-electromagnetic hybrid nanogenerator driven by wind for self-powered wireless transmission in Internet of Things and self-powered wind speed sensor. *Nano Energy.* 2020;68:104319.
335. Zhao X, Kang Z, Liao Q, et al. Ultralight, self-powered and self-adaptive motion sensor based on triboelectric nanogenerator for perceptual layer application in Internet of Things. *Nano Energy.* 2018;48:312-319.
336. Ahmed A, Hassan I, El-Kady MF, et al. Integrated triboelectric nanogenerators in the era of the Internet of Things. *Adv Sci (Weinh).* 2019;6(24):1802230.
337. Cheng X, Tang W, Song Y, Chen H, Zhang H, Wang ZL. Power management and effective energy storage of pulsed output from triboelectric nanogenerator. *Nano Energy.* 2019;61:517-532.
338. Luo J, Wang ZL. Recent advances in triboelectric nanogenerator based self-charging power systems. *Energy Storage Mater.* 2019;23:617-628.
339. Pu X, Li L, Song H, et al. A self-charging power unit by integration of a textile triboelectric nanogenerator and a flexible lithium-ion battery for wearable electronics. *Adv Mater.* 2015;27(15):2472-2478.
340. Chen Y, Cheng Y, Jie Y, Cao X, Wang N, Wang ZL. Energy harvesting and wireless power transmission by a hybridized electromagnetic-triboelectric nanogenerator. *Energy Environ Sci.* 2019;12(9):2678-2684.
341. Wang ZL. Triboelectric Nanogenerator (TENG)—sparking an energy and sensor revolution. *Adv Energy Mater.* 2020;10(17):2000137.

AUTHOR BIOGRAPHIES



Kai Wang is distinguished professor in College of Electrical Engineering, Qingdao University. He received his PhD degree in 2014 from Dalian University of Technology (China). He is a Member of Qingdao Young Scientists Association and executive secretary of innovation and entrepreneurship committee. His current research mainly focuses on the triboelectric nanogenerators for biomedical sensing and blue energy harvesting, state evaluation and life prediction of energy storage devices, supercapacitors and lithium-ion batteries, and human-machine interaction.



Hong Liu is a professor in State Key Laboratory of Crystal Materials, Shandong University. He also acts as a director of Institute for Advanced Interdisciplinary Research (IAIR), University of Jinan. He received his PhD degree in 2001 from Shandong University (China). He received The National Science Fund for Distinguished Young Scholars. His current research mainly focuses on chemical processing of nanomaterials for tactile sensors and electronic skins, energy-related applications including photocatalysis, tissue engineering (especially the interaction between stem cell and nanostructure of biomaterials), as well as the nonlinear optical crystals.



Gianauelio Cuniberti holds the Chair of Materials Science and Nanotechnology since 2007 at the Dresden University of Technology and is the founding director of the Dresden Center for Computational Materials Science (DCMS). He is an elected fellow of the European Academy of Sciences, elected member of Academia Europaea,

Honorary Professor at the Division of IT Convergence Engineering of POSTECH, the Pohang University of Science and Technology, and Adjunct Professor for the Department of Chemistry at the University of Alabama.

How to cite this article: Wang W, Pang J, Su J, et al. Applications of nanogenerators for biomedical engineering and healthcare systems. *InfoMat*. 2022;4(2):e12262. doi:10.1002/inf2.12262